Search for dark matter in association with a leptonically decaying Z boson in the ATLAS detector at the Large Hadron Collider

by

Alison A. Elliot
B.Sc., University of Victoria, 2010

A Dissertation Submitted in Partial Fulfillment of the
Requirements for the Degree of

DOCTOR OF PHILOSOPHY

in the Department of Physics and Astronomy

Search for dark matter in association with a leptonically decaying Z boson in the ATLAS detector at the Large Hadron Collider

by

Alison A. Elliot
B.Sc., University of Victoria, 2010

Supervisory Committee

Dr. R. Keeler, Supervisor
(Department of Physics and Astronomy)

Dr. R. McPherson, Supervisor
(Department of Physics and Astronomy)

Dr. M. Lefebvre, Departmental Member
(Department of Physics and Astronomy)

Dr. C. Bohne, Outside Member
(Department of Chemistry)

Supervisory Committee

Dr. R. Keeler, Supervisor
(Department of Physics and Astronomy)

Dr. R. McPherson, Supervisor
(Department of Physics and Astronomy)

Dr. M. Lefebvre, Departmental Member
(Department of Physics and Astronomy)

Dr. C. Bohne, Outside Member
(Department of Chemistry)

ABSTRACT

This dissertation describes a search for the invisible decays of dark matter particles produced in association with a Z boson, where the latter decays to a charged lepton pair. The dataset for this search includes 13.3 fb^{-1} of collisions recorded in 2015 and 2016 at a centre-of-mass energy of 13 TeV in the ATLAS detector at the Large Hadron Collider in Geneva, Switzerland. The invisible particles manifest themselves as missing transverse momentum, or $E_{\mathrm{T}}^{\mathrm{miss}}$, in the detector, while the charged leptons of interest are electron (e^+e^-) or muon ($\mu^+\mu^-$) pairs. The models simulated for this study are vector mediated simplified models with Dirac fermionic dark matter particles with couplings $g_q = 0.25$, $g_\chi = 1$ and $g_\ell = 0$. The main background to this analysis, $ZZ \to \ell^+\ell^-\nu\bar{\nu}$, is irreducible, as it shares the same signature as the signal. It is estimated with Monte Carlo simulations including contributions from both $qq \to ZZ$ and $gg \to ZZ$ production modes. Where possible, other backgrounds are estimated using data-driven techniques and reduced through various selection criteria. The final search is performed by looking for a deviation from the Standard Model background expectation in the $E_{\mathrm{T}}^{\mathrm{miss}}$ distribution using two signal regions, ee and $\mu\mu$. This is done using statistical tools to make a likelihood fit and set a 95% confidence level limit as no deviations are found. Limits are placed on the presented model of dark matter for mediator masses up to 400 GeV and for a range of dark matter masses from 1 to $\sim$ 200 GeV.

DECLARATION

Analysis contributions

- Dark matter summary paper contact for the Mono-Z analysis (2016-present)
- Studied acceptances of axial-vector dark matter models compared to vector models and confirmed acceptances equal in the on-shell region
- Editor for internal supporting documentation (Common Analysis Strategies) for the 2017 analysis paper
- Explored γ+jets in data as a possible technique for estimating the Z+jets background
- Editor for internal supporting documentation (Low Mass Analysis) for the 2016 conference note
- Worked on Z+jets background estimation with the ABCD technique
- Worked on providing 3ℓCR WZ scale factors, cross checks, and cutflow challenge
- Provided group cross checks on analysis event selection consistency
- Did Mono-Z analysis optimization for signal models (both Mono-Z and $ZH \to \ell^+\ell^- +$ invisible)
- Tested new event selection cuts and proposed thresholds for optimal cuts
- Co-developed and currently maintain analysis software package used by University of Victoria group

Detector and operations contributions

- Online software expert shifts for the Liquid Argon Calorimeter during 2015 data-taking (both p-p and p-Pb collisions)
- Contribution to the maintenance, development and operation of the Liquid Argon Calorimeter online system
- Contribution to the development and operation of the calibration tools as well as the organization and development of the LAr operations framework

Contents

List of Tables

List of Figures

ACKNOWLEDGEMENTS

There are so many without whom I would not be where I am today. I want to name you all here, but you know how bad my memory is! If you know me and you are reading this, thank you - I could not have done this without you.

I would like to say a special thank you to those who have so carefully edited this document - my supervisors Rob McPherson and Richard Keeler, Sam Harper, and Vanessa McCumber.

First off, I want to thank my parents - Randy and Janette Faulkner. Thank you for teaching and inspiring me. Your support of my every career whim has allowed me to explore what I really want to do. I also appreciated the subtle push to attend the University of Victoria; it has worked out surprisingly well. My entire family has been very supportive in my thesis writing over the past year. Thanks to Daniel Faulkner for showing me a coffee shop to work at and to Shanna for the encouragement. Thank you Craig Elliot and Carolynn Elliot, for driving me around Vancouver to all the best coffee shop offices to put together these caffeine-fuelled pages. Thanks too, to Brian for the welcome ski breaks and to Andrew for the bottomless goodies.

The last six years have been transformative. The students at the University of Victoria have made it such an enjoyable journey. Tackling assignments, teaching, pub quizzes, and conferences (I still have a scar from TSI) - thank you especially to Matt LeBlanc, Alex Beaulieu, and Steph Laforest. It was memorable, to say the least. Thanks to those of you 'older' and wiser for including me in grad student life, and as friends - Tony Kwan, Sam de Jong, Anthony Fradette, and Brock Moir. And of course to Frank, Lorraine, J-R, Jordan, Matthias, Lei, Di, Jaime, Jason, Nick, Jon, and so many more - thank you for all the good times and advice! I also know that curling kept me a bit more sane - thanks to Trystyn, Chelsea, Paul, and Jason, and everyone else who I got to play with and against. Thank you to Kayla McLean for taking on so many Mono-Z challenges with me, and for teaching me to do duck plots! Special thanks to Kate Taylor, whose enjoyment of physics is truly contagious.

My fifteen months at CERN were some of the most intense times I've been through. Thank you Chris Marino and Alex Martyniuk for welcoming me and letting me steal all your friends. Heather Russell, round two of sharing a place was awesome, and thank you for teaching me how to ride a bike - and how to enjoy mountains. I have loved exploring the world with you. Where to next? Tony Kwan, whether sharing a flat or sharing an office, I've appreciated your listening ear and helpful advice

throughout the last seven years - I promise I won't unfriend you on LinkedIn, or wherever. Anna Kopp, thank you for the cycling, the running, and the bouldering, and for the encouragement. It is always so good to hang out with you. Dirk Hufnagel, thank you for the movie nights, the wine tastings, and the many trips, it was great fun. Laurence (Lolly) Carson: thanks for being my friend - even if I practically had to beat you over the head for it! I am so thankful for all the encouragement, for the music, and for the fun hangout times all over the world. Mark Stockton, where to start? Thanks for introducing me to L'Escalade, for sharing your church, and for all the hangouts and chats. Rawwwwrrr (to both you and Tom Blake) for teaching me to ski! Sam Harper - I knew I was with good people as soon as I met you. I so appreciate your time (and your couch), your encouragement through the thesis lows, and your willingness to always help me out with anything. And for the so many more at CERN: Tom, Sue, Katharine & Pierre, Manuela, Rodger, Michael, Sebastian, Rob, Tamara, and more - thank you for helping make Switzerland feel like home.

To Michel Lefebvre, thank you for inspiring me to do particle physics as an undergraduate, for teaching me how to program well, and for increasing my appreciation of great science fiction.

To my supervisor Rob McPherson, thank you for your enthusiasm about beyond the Standard Model physics, and especially for your help pushing through my thesis in the last couple months. It has been an honour working with you.

And to my supervisor and mentor, Richard Keeler, (without whom my thesis would be an annoying collection of mostly extraneous adverbs and overwhelmingly colloquial or unnecessarily jargony terms) I have appreciated your direction and advice more than I can say and I believe I will be a much better scientist for the principles you have taught me. Thank you!

Finally, most of all, thank you, Mark Elliot. You are the best, even if you are the difficult one. I love you so much. Thank you for your love and support throughout the good times and the bad. Whatever comes next, I look forward to tackling it together.

It is the glory of God to conceal a matter,
But the glory of kings to search out a matter.
Proverbs 25:2, NKJV

Chapter 1

Introduction

The search for cold dark matter is heating up. The last piece of the Standard Model of particle physics, the Higgs Boson [1], fell into place without pointing to or even hinting at any new physics. Thus, the fact that more than 80% of the gravitationally attracting matter in the universe is still inexplicable within this theory heralds the existence of physics beyond the Standard Model (SM) [2], [3]. The existence of dark matter is well-established by astrophysical observations of galaxies [4] and galaxy clusters [5]. Moreover, the fundamental structure and dynamics of the universe as a whole are impossible given the known laws of physics without a large amount of dark matter [6]. Discovery of particle dark matter through production in a collider is the focus of this dissertation. Specifically, this is a search for dark matter that is produced simultaneously with a SM Z boson, referred to as a 'Mono-Z' search.

Evidence of dark matter and detection potential are presented in Chapter 2. Following this, the Standard Model and possible physics beyond it are introduced in Chapter 3 where the use of the Z boson as a probe for a particle theory of dark matter is explored. Chapter 4 introduces the CERN Large Hadron Collider (LHC) [7] and the ATLAS detector [8] as the experimental setup to test the theory, and Chapter 5 discusses the dataset obtained from the experiment and the Monte Carlo simulations used to help analyze it. The analysis of the data is outlined in Chapter 6, with the object and event selections, including optimization from the simulations. The full background estimation is described in Chapter 7. The error estimates on the analysis are shown in Chapter 8. Finally, in Chapter 9, the interpretation of the analysis results is presented, testing whether the considered Mono-Z dark matter models are found in nature. Finally, a comparison with other experiments is made, with a look to future tests.

Chapter 2

Motivation

There is a real possibility of discovering dark matter at the Large Hadron Collider (LHC) [7], [9]. The existence of dark matter, and the possibility of it being a particle, will be motivated in this chapter. Simple theoretical models have been developed to explain the potential interactions of particle dark matter with observable Standard Model particles. In 2015 the first dataset at a centre-of-mass energy of 13 TeV was delivered by the LHC, and in 2016 the integrated luminosity of the dataset at 13 TeV was increased tenfold. This represents a huge leap forward in sensitivity for searches like the Mono-Z analysis, opening possibilities of new studies and offering potential for discovery.

2.1 Dark Matter Motivation

The Standard Model (SM) of particle physics describes the known, identified elementary particles and their interactions. However, there are some gaps in the knowledge described by this theory. One of these gaps is dark matter. Dark matter is the name for a well established phenomenon observed through its effects on large astronomical structures and their dynamics in the universe [10], [11], [2]. There are at least four significant indicators for the existence of matter that interacts gravitationally, but is not accounted for in the SM.

One of the most straightforward motivations for the existence of dark matter can be found in individual galaxies. The orbital velocity of a star around the centre of a galaxy is governed by the amount of matter that its orbit encloses, as illustrated in Figure 2.1. When measuring the luminous matter, hot gas, and even accounting for

possible supermassive black holes at the centre of the galaxies, there is a deficit of ordinary matter that is needed to account for the observed velocities of the stars. This observation suggests several times more mass in the galaxies than what is expected from using electromagnetic radiation to predict the amount of luminous mass.

The velocity dispersion of galaxies within galaxy clusters that are in thermal equilibrium is another indicator of dark matter, and was the first observed astronomical indication of gravitational, but otherwise non-interacting matter [5]. Velocity dispersion is a measure of the spread of velocities around a mean value, and through the virial theorem can provide an estimate of the mass of a galaxy cluster. When the velocity dispersion of galaxy clusters are measured, the galaxies are moving faster than the gravitational potential that the visible mass could provide. This implies a great deal of excess matter that must exist beyond the luminous matter observed through the electromagnetic radiation.

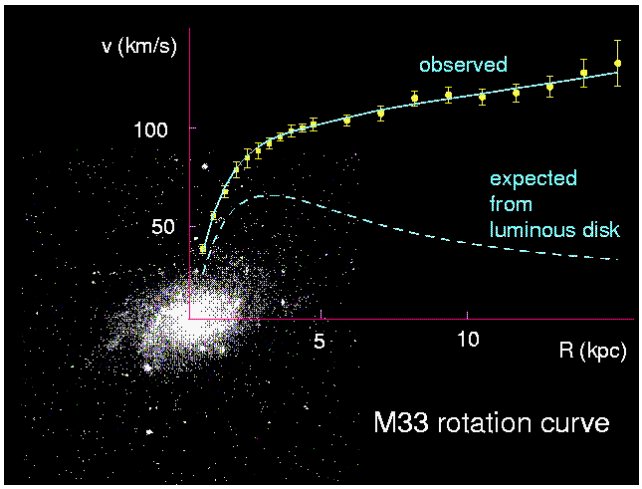

Figure 2.1: Observed rotation curve of a galaxy, superimposed on top of a visual observation of the galaxy, and the expected rotation curve for the luminous matter. [4]

High mass galaxy clusters distort the image of the distant galaxies behind them in a process known as 'lensing' as predicted by Einstein's theory of general relativity. The radius of curvature of the light from the lensed galaxy is related to the mass of the cluster. Once again, there appears to be much more mass contained in these galaxy clusters than can be accounted for with the stars and gas [12], [13], [14].

Finally, as described in the Review of Particle Physics [6] and the references contained within, the measurements of the anisotropies in the cosmic microwave background (CMB) indicate that there is an amount of non-luminous and non-reflective matter that is in excess of five times the amount of SM matter. This indicates that dark matter is not a phenomenon localized to galaxies or clusters of galaxies, but exists on the scale of the universe, and makes up more than 80% of the gravitationally

attractive matter.

Not only are inter- and intra-galactic kinematics, gravitational lensing, and the CMB each compelling evidence for dark matter on its own, but they also are in agreement with the amount of matter that would reconcile these observations. This is perhaps the most persuasive piece of evidence. Further large scale corroboration can be found in observations of type 1a supernovae [15], Big Bang nucleosynthesis [16], and baryon acoustic oscillations [17].

2.2 Dark Matter Particle Candidates

There are numerous popular theoretical candidates for dark matter (for an accessible introduction to many such candidates, see [10]), but the focus of this dissertation is the weakly interacting massive particle, or WIMP, candidate for dark matter. This particle, denoted by χ, is proposed to have a mass between 10 GeV and a few TeV, with an interaction cross section similar to SM weak interactions [6].

2.2.1 WIMP Miracle

Production and annihilation of dark matter as a stable weakly interacting massive particle would be in equilibrium in the early universe where the highest temperatures and densities existed. As the universe expanded and its temperature cooled below that corresponding to the mass of the χ particle, dark matter would fall out of creation and annihilation equilibrium. At the time when this happens, the number of χ particles becomes close to constant, known as the relic abundance, as it is no longer hot and dense enough for them to annihilate or be produced. What is often termed the 'WIMP Miracle' refers to the observation that if the dark matter has approximately electroweak mass and coupling, then it gives the relic densities estimated from cosmological observations [18].

2.2.2 Neutrinos

Neutrinos are a neutral SM particle that have been recently discovered to have mass [19]. They interact very weakly with other particles and, therefore, are a dark matter candidate particle. While they do make up a component of the dark matter in the universe, they cannot explain all dark matter. Due to their extremely light masses

and high velocities they are unable to reproduced the observed cosmological structure of the universe.

2.3 Dark Matter Searches

Dark matter searches described here are designed to discover non-relativistic 'cold' matter particles that interact not only through gravitation, but also through the weak force. There are three main ways a dark matter particle can be detected: direct detection, indirect detection, or production [10], [3]. See Figure 2.2 for a schematic of these processes. In direct detection, a dark matter particle scatters off a SM particle. For indirect detection the dark matter annihilates to produce SM particles. Collider production searches are where SM particles annihilate into a pair of dark matter particles. The collider production discussed in this dissertation is complementary to and has comparable discovery power to dark matter searches performed with the direct or indirect methods [20], [21], [22].

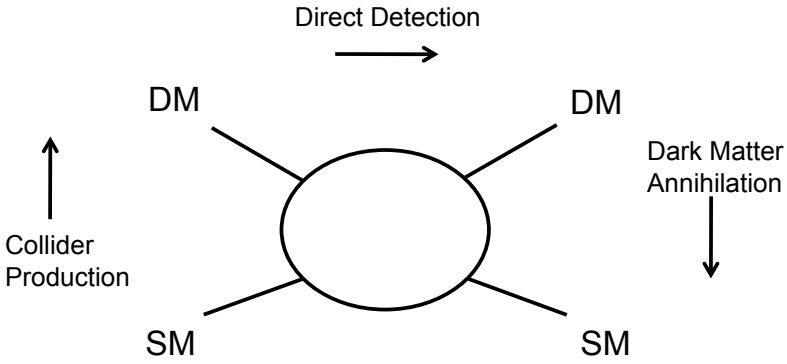

Figure 2.2: Dark matter (DM) interaction cross section.

2.3.1 Direct Detection

Direct detection searches for dark matter seek to detect an elusive interaction between a dark matter particle and the nucleus of an atom. The idea is to deploy a large volume of a stable material deep underground where there is a low radiation background rate. If the dark matter is weakly interacting, it may produce a detectable signal through an interaction with a nucleus in the material. This signal could be in the form of vibrational energy transferred to the nucleus as heat; it could be in the form of

scintillation from nuclear recoil as light; or it could be in the form of ionization of the nucleus as electrical energy.

There are two possible scenarios that direct detection has to consider - that the dark matter interaction is dependent on spin (SD), or it is independent of the spin of the nuclei (SI). The experiments LUX [23], XENON100 [24], and PandaX [25] place strong limits in the SI scenarios for a high mass dark matter particle, while CRESST-II [26] and SuperCDMS [27] place strong limits in the SI scenarios for lighter masses of dark matter. Experiments like DEAP-3600 [28] and Darkside-20k [29] have very low backgrounds and will be very sensitive to a dark matter mass at the EW scale for SI scenarios. For SD interactions, LUX and the PICO collaboration [30] place the strongest limits.

2.3.2 Indirect Detection

Indirect detection searches for dark matter are looking for radiation coming from the annihilation of two dark matter particles into one or more detectable SM particles. The idea is to observe an expected dense area of dark matter, such as the centre of a galaxy, and look for a signature consistent with annihilation into particles such as a photon or electron-positron pair. There have been observations of potential excesses in the Fermi-LAT high-energy gamma-ray data [31] that could be consistent with dark matter annihilation, but they have not been verified with other experiments. Similar searches are also ongoing at the Alpha Magnetic Spectrometer [32], and PAMELA [33].

2.3.3 Collider Production

Collider production is not as straight-forward as detecting an interaction or observing the annihilation products because dark matter particles do not leave a measurable signal within the detector. However, if the dark matter is produced with a net transverse[1] momentum with respect to the colliding particles, then it is possible to infer that a particle or particles were there but not seen. This is possible at the LHC where protons collide with protons. Here, some detectable SM particles (denoted here as X) could be created simultaneously that recoil against the dark matter ($\chi\bar{\chi}$) summarized

[1] In a collider, the transverse direction is defined by a plane perpendicular to the colliding beams.

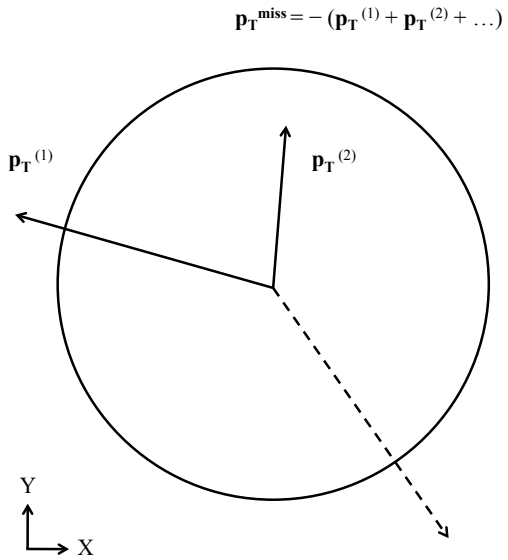

Figure 2.3: Illustration of missing transverse momentum. The vector sum of the momenta of the measurable particles (solid lines) in the X-Y plane, transverse to the beam in the negative direction (dashed line) is the missing transverse momentum: $\mathbf{p}_{\mathrm{T}}^{\mathrm{miss}} = -\big(\mathbf{p}_{\mathrm{T}}{}^{(1)} + \mathbf{p}_{\mathrm{T}}{}^{(2)} + ...\big)$. Its magnitude is commonly referred to as missing transverse energy, shortened to MET or $E_{\mathrm{T}}^{\mathrm{miss}}$.

in Equation 2.1.

$$pp \rightarrow \chi\bar{\chi} + X \tag{2.1}$$

By summing up the momentum of these SM particles and making use of the fact that the protons collide head on, and thus the total net momentum transverse to the beam should be zero, the noninteracting particles will reveal themselves as a nonzero recoil. The necessity of a beam pipe leaves a hole in the detector so only the momentum components perpendicular to the beam are used. This is missing transverse momentum; though, due to its being measured through deposits of energy in calorimeters, it is often known as 'missing transverse energy' (MET or $E_{\mathrm{T}}^{\mathrm{miss}}$) which refers to the magnitude of the quantity. This is illustrated in Figure 2.3.

The signature of dark matter is an event in a detector with missing energy recoiling from one or more SM particles. There are many different collision results that could produce an event with a signature that includes missing energy. The SM particle being produced at the same times as the dark matter for this dissertation is the Z boson, a massive, neutral mediator of the weak force that will be discussed in Chapter

3. This is summarized in Equation 2.2.

$$pp \to \chi\bar{\chi} + Z \tag{2.2}$$

In particular, the final state of interest here is the Z boson decaying to a charged lepton-antilepton pair (hereafter referred to as a 'lepton' pair, or $\ell^+\ell^-$). See Equation 2.3. This charged lepton pair originates from the decay of a Z boson. The lepton flavours of interest in this report are electron-positron pairs (hereafter referred to as 'electron' pairs) and muon-antimuon pairs (hereafter referred to as 'muon' pairs).

$$pp \to \chi\bar{\chi} + Z(\to \ell^+\ell^-) \tag{2.3}$$

There are known SM processes that produce an identical signature in the detector. The LHC detectors, including the ATLAS (A Toroidal LHC ApparatuS) detector, are unable to detect any direct signal from a neutrino (ν). Therefore neutrinos also produce a signal of missing energy. A major contributor to production of neutrinos in conjunction with a Z is where two Z bosons are produced together. Here one decays into a neutrino-antineutrino pair, while the other to a lepton-antilepton pair, in the process $pp \to ZZ \to \ell^+\ell^-\bar{\nu}\nu$. Another such signature is a Higgs boson decaying into two Z bosons, one of which decays to a lepton-antilepton, and the other to a neutrino-antineutrino pair: $pp \to H \to ZZ \to \ell^+\ell^-\bar{\nu}\nu$. There are other processes that will produce a similar signature, but have a different final state. One is where two W bosons produced together, and each decays to one lepton and one neutrino in the process $pp \to WW \to \ell^+\nu\ell^-\bar{\nu}$. Additionally, there are other SM processes that could fake a similar signature, such as $pp \to t\bar{t} \to \ell^+\nu b\,\ell^-\bar{\nu}\bar{b}$, $pp \to ZZ \to \ell^+\ell^-\bar{q}q$, $pp \to Wt \to \ell\nu\ell\nu b$, $pp \to WZ \to \ell\nu\ell^+\ell^-$, $pp \to WZ \to \bar{q}q\ell^+\ell^-$ or $pp \to Z$+jets, with misidentified or unreconstructed jets.

The theory that motivates this list of SM signatures will be discussed in Chapter 3.

Chapter 3

Theory

3.1 Standard Model

The Standard Model of particle physics as we know it began with a theory describing the unification of the electromagnetic and weak forces by Glashow, Salam, and Weinberg in the late 1960s [34], [35], [36] which was further developed throughout the 1970s. It describes everything known about the particles that make up the observable universe, and the fundamental forces that govern their interactions [37], [38], [39].

The particles are categorized by their properties. The broadest categories are fermions: particles that obey Fermi-Dirac statistics, and bosons: those that obey Bose-Einstein statistics. The particles and forces are shown in Figure 3.1. The quarks and leptons are fermions, with half spin values. Each fermion has an antiparticle partner (not pictured), which has the same mass and spin, but opposite electromagnetic (EM) charge. Quarks have fractional EM charge and couple through the strong force, while the leptons have whole (or zero) EM charge, and no strong coupling. The force carriers are boson particles, with spin 1. The Higgs boson [40] is a scalar particle, with spin 0, discovered by the ATLAS [41] and CMS collaborations [42] in

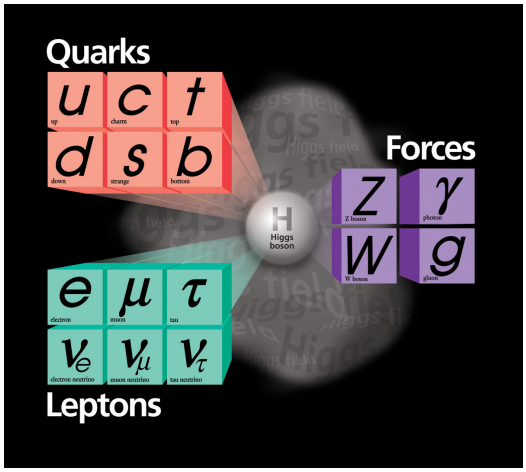

Figure 3.1: The Standard Model of particle physics. Image credit: Fermilab

2012.

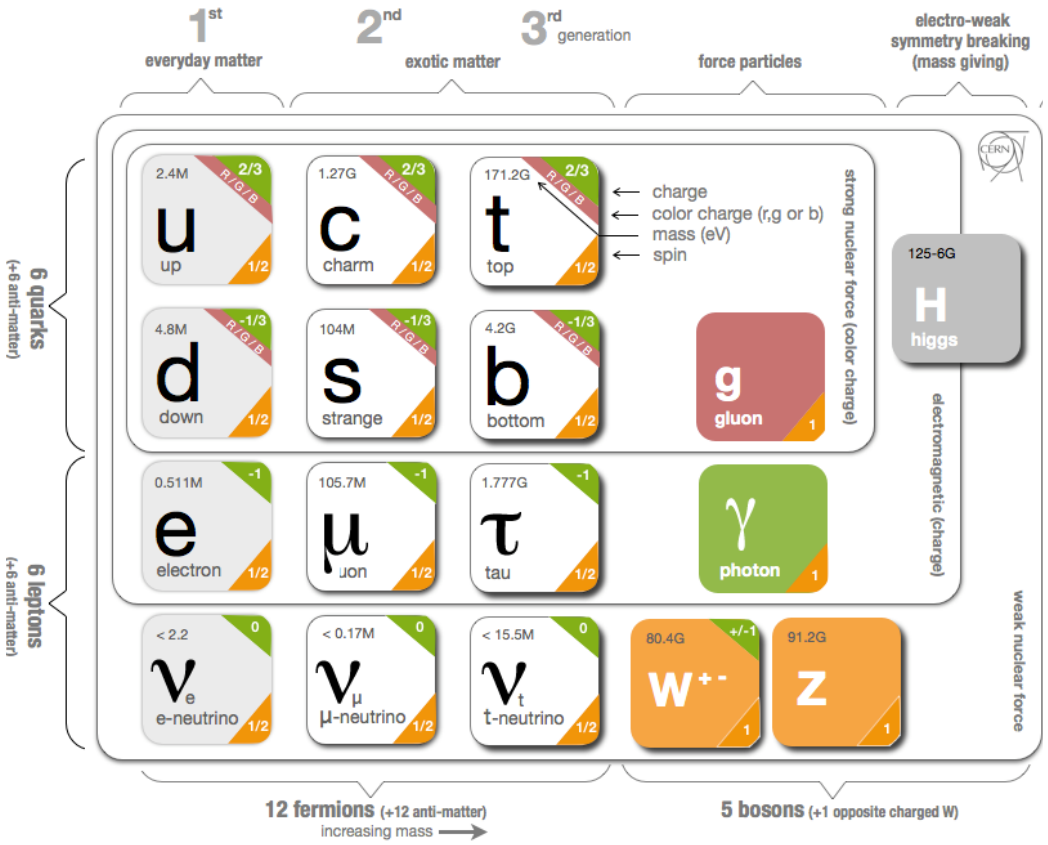

Figure 3.2: Table of the Standard Model particles and forces, along with their masses and couplings. [43]

The Standard Model (SM) describes the known forces and particles in the universe except gravity. Since its conception, it has made correct predictions and has been tested to a standard of precision that has established it as the accepted theoretical model of particles physics. The masses, charges, and interactions of these known particles are detailed in Figure 3.2. This will be discussed further in the following sections.

3.1.1 Fundamental Forces

There are three fundamental forces that are known to govern through the exchange of a force carrier particle. These forces are the electromagnetic, the weak, and the strong force. The gravitational force is very important to the understanding of the universe; however, it is not yet described by the exchange of a force carrier particle, and does not enter into the SM.

Electromagnetic Force

The electromagnetic force governs the interactions of particles with electric charge through the exchange or emission of a photon, γ. This boson is massless, electrically neutral, and does not interact through the weak force. It is responsible for most macroscopic phenomenon observed in matter. At very low energies, such as exchanges near the mass of the γ, the fundamental strength of the electromagnetic interactions are $g_e \propto \alpha_{EM} \approx 1/137$, while interactions happening near the mass of the Z boson (m_Z) have a strength of $\alpha_{EM}(m_Z) \approx 1/128\,(\approx 0.0078)$ [6]. The theory of electromagnetism is known as Quantum Electrodynamics (QED).

Strong Force

The strong force is the force that governs the interactions of particles with 'colour' charge through the exchange or emission of a gluon. Gluons are massless bosons with no electric charge, but they interact with themselves. The force acts on a short range, as it is confined due to its self interactions; however, it is much stronger than the electroweak force. It is responsible for the binding of quarks into hadrons. Colour charge is comprised of three charges: red, green, and blue (r, g, b). It has three anticharges as well: antired, antigreen, and antiblue ($\bar{r}$, $\bar{g}$, $\bar{b}$). The fundamental constant for the scale of the strong interactions at m_Z is $\alpha_s(m_Z) \approx 0.1185$ [6]. This is more than ten times stronger than the electroweak force at this scale. The theory of the interactions involving the strong force is known as Quantum Chromodynamics (QCD).

Weak and Electroweak Forces

The weak force is analogous to the electromagnetic force, and governs the interactions of fermions through the exchange or emission of the weak bosons, the W^+, W^-, and

Z. The Z boson is neutral, while the two W bosons are electrically charged. The mediators of this force are self-interacting in the same manner as the strong force previously described. However, the weak force is much weaker than the electromagnetic force because, unlike the photon, the weak bosons have mass. The coupling of the weak force is $\alpha_w \approx 1/29\,(\approx 0.034)$, but is suppressed by a factor proportional to the square of the mass of the W boson. At higher energies, near the mass scale of the weak bosons (~ 100 GeV), the unification of the weak and electromagnetic forces becomes apparent and is known as the electroweak (EW) force [34], [35], [36].

3.1.2 Fundamental Particles

Any SM particle can be produced in proton-proton collisions. The SM particles as well as their properties and interactions are presented here. Each of these particles will have some contribution to this Mono-Z search for dark matter.

Bosons

Photons Photons are bosons that are electromagnetically neutral, colour neutral, and massless. They are the charge carriers of the electromagnetic force, described by QED. When photons are produced at the very high energies of the LHC, their signature in a calorimeter detector appear very similar to those of the electron. The coupling of the photons to electroweak particles can be modelled by the process in Figure 3.3.

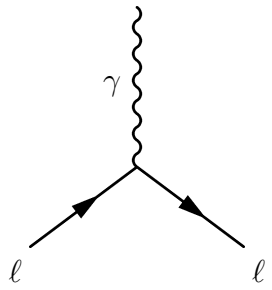

Figure 3.3: Fundamental QED interactions, where γ is a photon, and ℓ is a charged lepton.

Gluons Gluons are massless bosons with no electric charge. Gluons exist in linear combinations of colour and anticolour charges. They carry the colour charge of the strong force. As they are themselves charged, along with coupling to quarks, they are self-interacting. These interactions are illustrated in Figure 3.4. If gluons or quarks are produced or pulled from other constituents in a collision, they will attempt to form colour singlets, or hadronize, and produce a collimated 'jet' of particles in a detector.

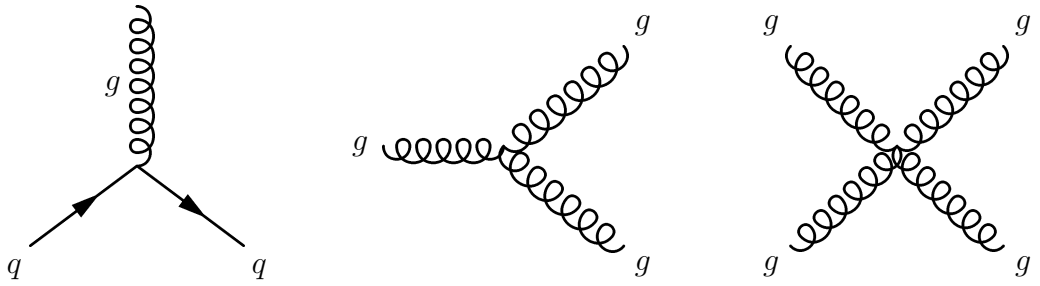

Figure 3.4: Fundamental QCD interactions.

W **and** Z **Bosons** The W and Z bosons are the massive carriers of the weak force. They have masses of 80 GeV and 91 GeV respectively (see Figure 3.2). The W bosons have electromagnetic charge, while the Z boson is electromagnetically neutral. They interact with various fermions differently as shown in Figure 3.5. As introduced earlier, like the gluons, these mediators are self-interacting. The self-interactions are shown in Figure 3.6. As they are so massive, they are unstable and decay on a short time scale. Therefore they are not observed directly; rather their decay products are measured in a detector. The Z boson decays can be inferred from their fundamental interactions shown here, and will be explored further in Section 3.1.4.

Fermions

Charged Leptons Electrons, muons and taus are leptons with half-integer spin, an electric charge of -1, and no colour charge. They each have an antiparticle of the same mass and opposite charge. Leptons interact through the electroweak force. The three flavours of leptons are in the same family of particles, but are different generations. These generations are different only in mass, all other properties remain unchanged.

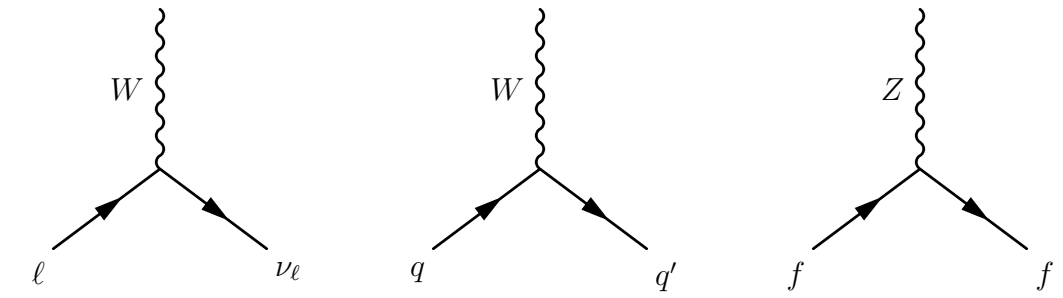

Figure 3.5: Fundamental EW interactions of bosons with various fermions with all fermions (f), charged leptons (ℓ), neutral leptons (ν_ℓ), and quarks (q, q') where q and q' differ by ± 1 in electric charge.

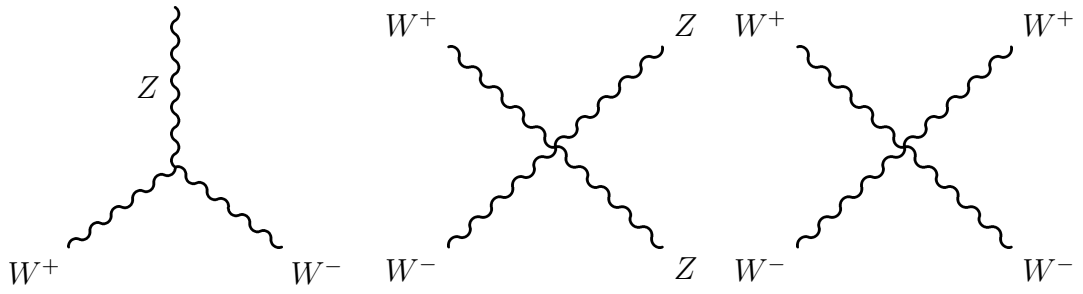

Figure 3.6: Fundamental EW self interactions of bosons. Note: anywhere the Z boson appears, it could be replaced by a photon, γ.

The electron and muon particles are a focus of this dissertation. The electron has a mass of 0.511 MeV and the muon has a mass of 106 MeV (see Figure 3.2). This large mass disparity causes profound differences in the procedure for detecting them, as will be shown in Chapter 4.

Quarks Quarks are fermions that have fractional electric charge as well as colour charge. There are three generations of positively and negatively charged quarks that only differ from each other by mass. The large masses of the second and third generation quarks, see Figure 3.2, mean that they decay into lighter quarks by means of a fundamental quark interaction, see Figure 3.5. For example, the heaviest quark, the t-quark, will decay to a b-quark by the emission of a W boson. The b-quark in turn will also decay by emission of a W. The antiquarks follow the same rules as quarks, differing only in electrical charge sign.

As quarks have a colour charge, when they are produced from the colliding particles in an interaction they will attempt to form colour singlets, or hadronize. Hadronization will be explained more in the next section. In a detector this appears as a collimated group of particles known as a 'jet'.

Neutrinos Finally, the most elusive of the Standard Model particles are the electrically neutral leptons known as neutrinos. They have masses much smaller than the electron (as yet there are only upper bounds on their masses [44]), and do not carry colour charge. Neutrinos interact only through the weak and gravitational forces and therefore rarely interact with ordinary matter. This makes neutrinos effectively invisible to the detectors at the LHC.

3.1.3 Hadronic Collisions

Hadrons are not fundamental particles. At the simplest level, they are made up of two or three quarks held together with the strong force. The hadronic particle collided at the LHC is the proton. Protons are made up of two up quarks and a down quark. However, at the high energies in a collider environment, this simple picture is too naive to describe the interactions observed.

In order to describe protons at high energies, a model called the Parton Model was proposed by Feynman [45]. This model shows the proton as made up of not only the three quarks in the simple picture, which are now known as valence quarks, but

also gluons and quark-antiquark pairs known as sea quarks.

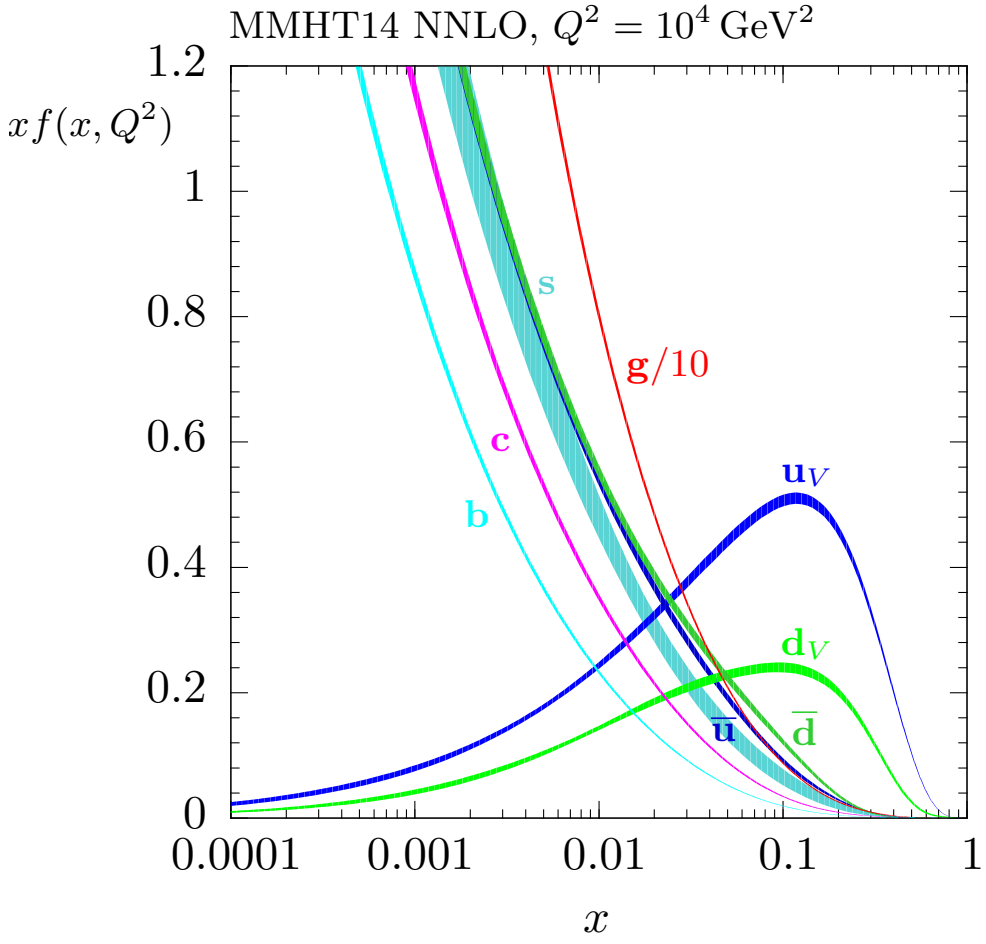

Figure 3.7: Parton distribution function at a momentum transfer of $Q^2 = 10^4$ GeV^2 of gluons (g), valence quarks (q_V), and sea quarks or antiquarks (q or $\bar{q}$), for fraction of total momentum (x) that each parton carries. [46]

The distribution of gluons and quarks (or partons, collectively) changes with the energy available to the proton. These are known as the Parton Distribution Functions (PDFs), as seen in Figure 3.7. Once the PDFs are measured as a function of x, the fraction of momentum of the proton that the parton carries can be calculated through equations known as the DGLAP equations [47], [48], [49], which evolve the PDF with the momentum exchange Q^2. New data are continually being added using empirical observations from all high energy colliders.

Proton-Proton Collisions

Proton-proton collisions are complicated. This is illustrated in Figure 3.8. Protons are comprised of quarks and gluons interacting through both the strong and electroweak forces. Many outcomes are therefore possible during any given collision. The high-energy collision where the partons in the proton interact to form new particles is referred to as the 'hard scatter'. The hard scatter could involve the collision of any two partons: a $q\bar{q}$ pair, a gg pair, or a qg or $\bar{q}g$ pair.

In addition to the hard scatter event, the incoming or outgoing constituents give off secondary radiation known as initial state radiation (ISR) or final state radiation (FSR). As well, since the hard scatter only occurs between one parton from each proton, the remaining partons are no longer in a colour singlet and there is a leftover soft interaction known as the underlying event which appears as soft jets in the detector.

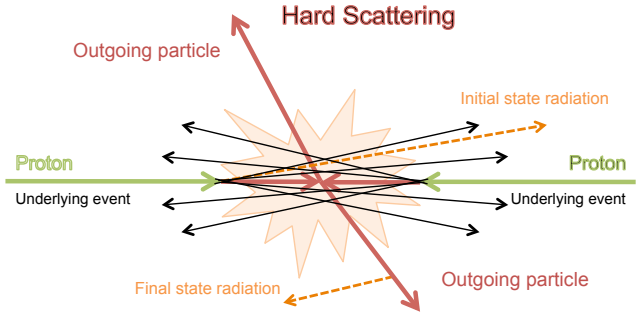

Figure 3.8: Proton-proton collision schematic (based on figure in [50]).

The hard scatter products of the collision are those of interest to a search for new physics. In order to increase the number of hard scatters, the beams are collided with an intensity that leads to multiple protons interacting in each beam crossing, called 'pileup'. This makes the already complex situation even more chaotic but increases the probability of rare interactions occurring. The goal is to discover any possible new particles. As the creation of any particles that interact by the strong or the electroweak forces is possible from the annihilation of the partons, it is conceivable that particles not yet discovered (beyond the Standard Model particles in Figures 3.1, 3.2) will be created. If these processes are rare, then they require large amounts of integrated luminosity to discover.

Luminosity

Luminosity is a measure of the rate of interactions per area per time. Luminosity is typically measured in $\text{cm}^{-2}\ \text{s}^{-1}$. The luminosity of a collider is dependent on its operating parameters, according to the equation:

$$\mathcal{L} = \frac{fN^2}{4\epsilon\beta^*} \tag{3.1}$$

where f is the frequency of collisions, N is the number of particles in each beam, ϵ is a measure of emittance, and β^* is a measure of the beam cross-sectional size at the collision point [51].

Cross Section

The cross section for an interaction, σ, is a quantity with units of area (measured in barns, where 1 barn $= 10^{-24}$ cm^2). It is a measure of the probability of an interaction to occur. When particles collide in an accelerator, the rate of these interactions, R, is the instantaneous luminosity, $\mathcal{L}$, times the corresponding cross section as in Equation 3.2. Integrating that luminosity over a period of time gives the integrated luminosity, $\int \mathcal{L}\, dt$, which, instead of interaction rate, will give the number, N, of interactions over that period of time, as in Equation 3.3.

$$R = \sigma\mathcal{L} \tag{3.2}$$

$$N = \sigma \int \mathcal{L}\, dt \tag{3.3}$$

The cross section determines how many interactions are expected at a particular luminosity. The cross section is dependent on the momentum transfer of the interacting particles in the collisions.

3.1.4 The Z Boson

The Z boson is a fundamental particle of the Standard Model. It is a massive, neutral mediator of the weak force. It can be produced in proton-proton collisions from a quark and an antiquark as in Figure 3.9 but its large mass means it decays quickly.

Once produced, either through the hard scatter or initial state radiation, the neutral Z boson will decay to a fermion-antifermion pair ($f\bar{f}$). The relative probability

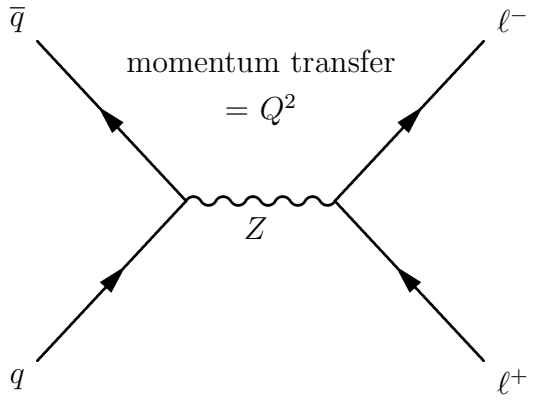

Figure 3.9: Z boson decaying to lepton-antilepton pairs. The magnitude of the momentum transfer of the interaction is labelled in the diagram, Q^2.

of decay to a particular final state is known as the branching fraction (indicated by the abbreviation Br). This final state is the observable quantity in the detector, and the probability of producing it is proportional to the cross section multiplied by the branching fraction, which is determined by the decay width of the final state divided by the total decay width. For example, the cross section of the decay of a Z boson to an electron-positron pair is defined in Equation 3.4, where $\sigma(Z)$ is the cross section for a Z boson to be produced, and $Br(Z \to e^+e^-)$ is the probability for the Z boson to decay into an e^+e^- pair.

$$\sigma(Z \to ee) \equiv \sigma(Z) \times Br(Z \to e^+e^-) \tag{3.4}$$

The branching ratio for $Br(Z \to e^+e^-)$ is the ratio of the decay width for the Z boson to electrons: $\Gamma(Z \to e^+e^-)$, to the total decay width: $\Gamma(Z)$:

$$Br(Z \to e^+e^-) = \Gamma(Z \to e^+e^-)/\Gamma(Z), \tag{3.5}$$

where the width for the Z boson to decay [39] is

$$\Gamma(Z) = \frac{g_Z^2 M_Z c^2}{48\pi\hbar}\left(|c_V^f|^2 + |c_A^f|^2\right). \tag{3.6}$$

Here g_Z, c_V, and c_A are the weak coupling constants and depend on the fundamental parameter known as the weak mixing angle (θ_w), electric coupling and charge (g_e and q_e), and weak isospin.

Each of the possible final states has a probability based on the ratio of the decay width of that state to the total decay width of the Z, and depends on the mass of the Z and the weak coupling constants. The values of the probability of the Z decaying into a given final state are shown in Table 3.1 [52]. The Z boson decays primarily to lepton-antilepton ($\ell^+\ell^-$) pairs, neutrino-antineutrino ($\nu\bar{\nu}$) pairs, and hadron pairs (which will not be studied in this report). Note that the decay mode for $\nu\bar{\nu}$ pairs is indicated by the designation 'invisible'. This is because neutrinos and antineutrinos are invisible to collider experiments that have studied these decay modes. The only Standard Model particles that could be responsible for an invisible final state from the Z boson are the previously mentioned $\nu\bar{\nu}$ pairs. This is supported by the precise measurement of the decay width of the Z boson at the CERN LEP experiments [53], [54].

Decay Mode (Γ)	Decay Fraction (%)
e^+e^-	3.363 ± 0.004
$\mu^+\mu^-$	3.366 ± 0.007
$\tau^+\tau^-$	3.370 ± 0.008
invisible ($\nu\bar{\nu}$)	20.00 ± 0.06
hadrons	69.91 ± 0.06

Table 3.1: Decay Modes for the Z boson from the Particle Data Group [52].

Initial State Radiation

Initial state radiation (ISR) of a strongly interacting particle, such as a gluon, is relatively common in proton-proton collisions. It is also possible to radiate photons or weakly produced particles such as Z bosons. This is less common than the radiation of a strongly interacting particle, which happens with the strength of $\alpha_s \approx 0.1$, or approximately 10% of the time. As the electroweak force is responsible for the emission of a Z boson as initial state radiation, it is a less frequent occurrence. Despite occurring less frequently than ISR of quarks or gluons, it can be easier to identify an ISR Z boson in the ATLAS detector, as will be discussed in Chapter 4.

3.1.5 Effective Field Theories

An effective field theory assumes that the mediator of any interaction is heavy compared to the momentum transfer of that interaction, and can therefore be integrated

out. As an example, the interactions mediated by the weak force happen through a massive mediator particle: the Z or $W^{\pm}$ bosons. (This is analogous to the electromagnetic interactions, which are mediated by the massless photon, γ.) Because the mediators are massive, the interactions are short-ranged. If the momentum transfer is small compared to the mass of the mediator ($Q^2 << M_{W,Z}$), then the scattering amplitude, f, is independent of the momentum transfer. This can be treated as a point-like interaction with a strength proportional to the mass of the mediator, as can be seen in Equation 3.7. This simplifies the couplings between the weak bosons and quarks and leptons to be through the weak coupling constant g_w:

$$f(Q^2) = \frac{g_w^2}{Q^2 + M_{W,Z}^2}, \tag{3.7}$$

where g_w is related to the electromagnetic coupling (g_e) through

$$g_w = \frac{g_e}{\sin\theta_w}. \tag{3.8}$$

Fermi theory was postulated in the 1930's to explain weak decay [37] with a coupling strength G between the fermions, which is defined as the scattering amplitude in a low-momentum transfer scenario as in Equation 3.9.

$$G \equiv \frac{g_w^2}{M_{W,Z}^2} \tag{3.9}$$

This can be further illustrated by looking at muon decay as an example, where the muon decays to an electron and two neutrinos ($\mu^- \rightarrow e^- \bar{\nu_e} \nu_\mu$). As seen in Figure 3.10, the interaction can be thought of as a point-like interaction between the four fermions (left). Only when the momentum transfer nears the mass of the W^- boson does the full interaction (right) need to be considered.

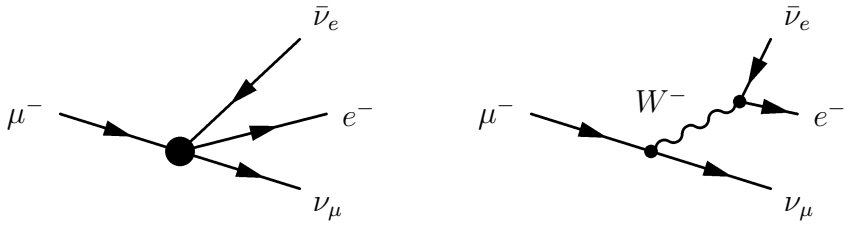

Figure 3.10: Muon decay through a contact interaction effective field theory (left) and through a mediator particle, the W boson (right).

This illustrates the effective field theory nature of the Standard Model at low

momentum transfer. This picture will be useful for imagining a similar scenario for dark matter production, described in the next section.

3.2 Beyond the Standard Model: Dark Matter

The Standard Model is a theory that has been exceptionally well-tested to a high degree of precision [6] and has been an incredibly powerful prediction tool over the decades. However, as it stands today, it cannot explain the prevalence of dark matter in the universe. Therefore, many attempts to extend the SM in order to explain dark matter are currently being experimentally tested.

3.2.1 Effective Field Theory of Dark Matter

Dark Matter (DM), if it interacts with SM particles through any force other than gravity, interacts in an unknown way. In order to make predictions for searches, some assumptions must be made. The most model independent case is to construct a new effective field theory (EFT) [55]. As stated in Section 3.1.5, an EFT is valid in the region where the momentum transfer of any interaction does not approach the mass of a given mediator particle. As the energy of the LHC is increased, it becomes more likely that a theoretical heavy mediator (for example, on the order of 1 TeV, which is a natural assumption in DM theories) will be accessible in the collisions, and the validity will break down. This will be discussed at the end of this section.

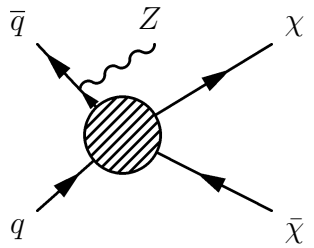

Figure 3.11: Diagram for ISR in an effective field theory.

As can be seen in Figure 3.11, the form of the interaction that produces DM can be effectively described as a contact interaction between the SM and DM particles. Under the assumption that the DM particle, in the form of WIMP DM as described in Chapter 2, is the only new particle accessible at the energies of the LHC, and that

the EFT assumption is valid, the Lagrangian describing the interaction between the quarks (q) and DM (χ) [56] seen in the EFT is

$$\mathcal{L} = \mathcal{L}_{SM} + \bar{\chi}\gamma^{\mu}\partial_{\mu}\chi - M_{\chi}\bar{\chi}\chi + \sum_{q}\sum_{i,j}\frac{G_{qij}}{\sqrt{2}}[\bar{\chi}\Gamma_{i}^{\chi}\chi][\bar{q}\Gamma_{q}^{j}q]. \tag{3.10}$$

In Equation 3.10, the first term, $\mathcal{L}_{SM}$, describes the interaction of the quarks and the SM particle 'X' in the diagram. The second and third terms describe the DM kinematic and mass elements. The final term in the Lagrangian describes the interaction between the SM and DM particles. The i and j indices of Γ and the coefficient G run through the scalar, pseudo-scalar, vector, axial-vector, and tensor couplings that are possible, where G_{qij} are the various coupling strengths, in the style of the Fermi coupling in Equation 3.9. The operators Γ, that couple the DM to either the quarks or the gluons, when written explicitly, can be seen in Table 3.2, where the DM couplings G_{χ} are expressed in terms of the energy scale M_* which is the scale of validity of the EFT model, and is often denoted as Λ.

Name	Operator	Coefficient
D1	$\bar{\chi}\chi\bar{q}q$	m_q/M_*^3
D2	$\bar{\chi}\gamma^5\chi\bar{q}q$	im_q/M_*^3
D3	$\bar{\chi}\chi\bar{q}\gamma^5 q$	im_q/M_*^3
D4	$\bar{\chi}\gamma^5\chi\bar{q}\gamma^5 q$	m_q/M_*^3
D5	$\bar{\chi}\gamma^{\mu}\chi\bar{q}\gamma_{\mu}q$	$1/M_*^2$
D6	$\bar{\chi}\gamma^{\mu}\gamma^5\chi\bar{q}\gamma_{\mu}q$	$1/M_*^2$
D7	$\bar{\chi}\gamma^{\mu}\chi\bar{q}\gamma_{\mu}\gamma^5 q$	$1/M_*^2$
D8	$\bar{\chi}\gamma^{\mu}\gamma^5\chi\bar{q}\gamma_{\mu}\gamma^5 q$	$1/M_*^2$
D9	$\bar{\chi}\sigma^{\mu\nu}\chi\bar{q}\sigma_{\mu\nu}q$	$1/M_*^2$
D10	$\bar{\chi}\sigma_{\mu\nu}\gamma^5\chi\bar{q}\sigma_{\alpha\beta}q$	i/M_*^2
D11	$\bar{\chi}\chi G_{\mu\nu}G^{\mu\nu}$	$\alpha_s/4M_*^3$
D12	$\bar{\chi}\gamma^5\chi G_{\mu\nu}G^{\mu\nu}$	$i\alpha_s/4M_*^3$
D13	$\bar{\chi}\chi G_{\mu\nu}\tilde{G}^{\mu\nu}$	$i\alpha_s/4M_*^3$
D14	$\bar{\chi}\gamma^5\chi G_{\mu\nu}\tilde{G}^{\mu\nu}$	$\alpha_s/4M_*^3$

Name	Operator	Coefficient
C1	$\chi^{\dagger}\chi\bar{q}q$	m_q/M_*^2
C2	$\chi^{\dagger}\chi\bar{q}\gamma^5 q$	im_q/M_*^2
C3	$\chi^{\dagger}\partial_{\mu}\chi\bar{q}\gamma^{\mu}q$	$1/M_*^2$
C4	$\chi^{\dagger}\partial_{\mu}\chi\bar{q}\gamma^{\mu}\gamma^5 q$	$1/M_*^2$
C5	$\chi^{\dagger}\chi G_{\mu\nu}G^{\mu\nu}$	$\alpha_s/4M_*^2$
C6	$\chi^{\dagger}\chi G_{\mu\nu}\tilde{G}^{\mu\nu}$	$i\alpha_s/4M_*^2$
R1	$\chi^2\bar{q}q$	$m_q/2M_*^2$
R2	$\chi^2\bar{q}\gamma^5 q$	$im_q/2M_*^2$
R3	$\chi^2 G_{\mu\nu}G^{\mu\nu}$	$\alpha_s/8M_*^2$
R4	$\chi^2 G_{\mu\nu}\tilde{G}^{\mu\nu}$	$i\alpha_s/8M_*^2$

Table 3.2: Lagrangian operators coupling DM particles to SM particles. Operator names beginning with D, C, R apply to Dirac fermions, complex scalars or real scalars, respectively. From Goodman, *et.al.* [21]

Initial State Radiation EFTs

Typically, the initial state radiation (ISR) phenomenon is studied in the context of a quark or gluon radiation from one of the incoming partons in the interaction. However, it can also be discussed in the context of electroweak radiation of a boson [57], [58], [59]. Other than a quark or gluon, the incoming partons can also radiate a photon, or a Higgs, W, or Z boson. The difference between the couplings α_{EM} and α_s means that electroweak ISR is ten times less likely than strong ISR. See the previous discussion of ISR in Section 3.1.4.

As can be seen in Figure 3.11, DM is only inferable in the detector because of the ISR. In this particular figure, a Z boson is shown as the ISR particle that recoils against the invisible DM. A Lagrangian for this process is shown in Equation 3.10 and uses the interaction coefficients D1, D5, and D9 from Table 3.2. This choice of coefficients is motivated by theory in order to avoid redundant or suppressed channels [21]. This contact portion of the Lagrangian for these coefficients is shown in Equation 3.11, where Λ is the scale of validity for the theory, often expressed as the mass scale M_* of the coefficients.

$$\mathcal{L} \supset \sum_q \Big(\frac{m_q}{(\Lambda_{D1})^3} \bar{\chi}\chi\bar{q}q \; + \frac{1}{(\Lambda_{D5})^2} \bar{\chi}\gamma^\mu\chi\bar{q}\gamma_\mu q + \frac{1}{(\Lambda_{D9})^2} \bar{\chi}\sigma^{\mu\nu}\chi\bar{q}\sigma_{\mu\nu}q \Big) \tag{3.11}$$

Contact Interaction EFTs

In addition to the ISR production of a SM particle, SM particles can be produced in conjunction with DM particles when the DM particle pair is radiated from an intermediately produced Z boson or photon, in an interaction called a 'contact interaction'. The operator for this channel is $ZZ\chi\chi$, and the Lagrangian is given by Equation 3.12, where k_1 and k_2 are related to the coupling of Z and DM particles, respectively, and Λ is the cutoff, or validity scale. See Figure 3.12 for the Feynman diagram of the process.

$$\mathcal{L}_{\text{int}} = \frac{k_1}{\Lambda^3}\chi\bar{\chi}F^1_{\mu\nu}F_1^{\mu\nu} + \frac{k_2}{\Lambda^3}\chi\bar{\chi}F^2_{\mu\nu}F_2^{\mu\nu} \tag{3.12}$$

This is a model where the Z boson (or photon) has direct interaction with DM particles. It is the identical signature in the detector, but it has some differences in the intermediate particle, which can be either a Z or a $\gamma*$, so the relative contributions

are a parameter of the model. These differences have an effect on the kinematics of the final state Z boson [60].

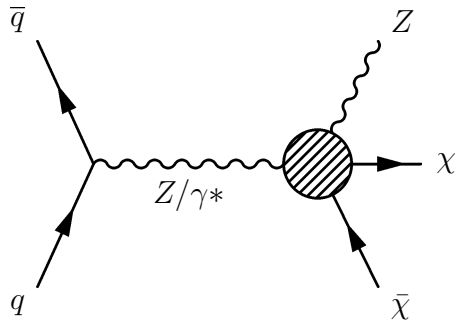

Figure 3.12: Diagram for contact interaction effective field theory.

Validity of EFTs

EFTs are only valid when the momentum transfer of the collision (Q^2) is less than the mass scale of the mediator (Λ) [61]. Therefore, at the centre-of-mass energies now accessible by the LHC, it becomes increasingly complicated to ensure the validity of the EFTs. Another approach to make a simple model of DM is to choose a few additional parameters to extend the validity of the EFT at these energy regimes. The most basic additional parameters to extend such a model are mediators and their couplings. A model with these additional parameters is known as a 'simplified model', and extends the EFT by adding only a single mediator directly connecting the SM particle to the DM particle. However, simplified models also have validity limitations, as will be discussed later.

3.2.2 Simplified Models

Simplified models are theoretical models that use the minimum number of parameters necessary to build a mediator connected model of SM and DM particles. This requires extending the EFTs to include a small number of degrees of freedom: the mass of the DM (m_χ), mass of the mediating particle (m_{med}), and the mediator couplings to both SM and DM particles (g_q and g_χ) [62].

A set of parameters is required that gives a small number of representative simplified models that cover a maximum of possible kinematic regions of the final states.

This is important, as there are many possible mass values to consider, for both the mediator and the DM particles.

Mediators

In Table 3.3 the first three lines list interactions with a scalar mediator (η) that decays to a Dirac fermion DM particle (χ) in the t- or s-channel, through either a scalar or pseudo-scalar coupling.

The last two lines in Table 3.3 summarize the Dirac fermion DM particle with vector or axial-vector couplings to a vector mediator (ξ). This interaction can be seen in Figure 3.13, and is the model used in this Mono-Z search.

Mediator	Channel	Coupling	Lagrangian Interaction Term
Scalar (η)	t-channel	Scalar	$\mathcal{L}_{int} = g_s\bar{\chi}q\eta + g_s\bar{q}\chi\eta$
Scalar (η)	s-channel	Scalar	$\mathcal{L}_{int} = g_s\bar{q}q\eta + g_{\chi s}\bar{\chi}\chi\eta$
Scalar (η)	s-channel	Pseudo-Scalar	$\mathcal{L}_{int} = g_{p\bar{q}}\bar{q}\gamma^5 q\eta + g_{\chi p}\bar{\chi}\gamma^5\chi\eta$
Vector (ξ)	s-channel	Vector	$\mathcal{L}_{int} = g_v\bar{q}\gamma^\mu q\xi_\mu + g_{\chi v}\bar{\chi}\gamma_\mu\chi\xi^\mu$
Vector (ξ)	s-channel	Axial-Vector	$\mathcal{L}_{int} = g_a\bar{q}\gamma^\mu\gamma^5 q\xi_\mu + g_{\chi a}\bar{\chi}\gamma_\mu\gamma^5\chi\xi^\mu$

Table 3.3: Lagrangian operators coupling Dirac fermion DM particles to SM quarks through a mediator.

In order to eventually combine the results from analyses in various channels (searching for DM tagged with a photon, for example), the DM models used in each search need to be the same. An effort was made across the detector collaborations at the LHC to not only harmonize the DM model choices between searches in different channels, but also in different subgroups, groups, and even experiments [9]. This will allow for a broad comparison of results. The choice of model was done in order to allow these comparisons to be possible through a combination of results.

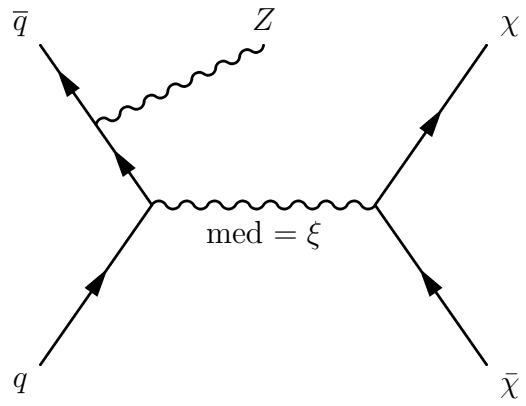

Figure 3.13: Diagram for ISR Z boson in a simplified model theory. The mediator (ξ) is shown decaying into fermionic DM ($\bar{\chi}\chi$), while the quarks ($\bar{q}q$) are shown radiating an ISR Z boson.

The signal model chosen for this analysis was the s-channel vector mediator model, with vector couplings $g_\chi = 1.0$ and $g_q = 0.25$.

Validity of Simplified Models

Simplified models, as they have been presented here, have serious limitations as a particle DM theory. They are meant to guide DM searches in terms of what particle final states to look for, and at what energy scale. However, they are far from being a complete theory. They fail when it comes to "gauge invariance" or "perturbative unitarity". In order to make a more physically motivated theory, these issues would need to be addressed. However, these models are extremely useful as a guide, providing parameters for a search analysis, and a common point for different analyses to compare results with each other.

Chapter 4

Accelerator and Detector

4.1 The Large Hadron Collider

The Large Hadron Collider (LHC) is a synchrotron accelerator that collides protons. The LHC has a circumference of 26.7 km, and is 100 m underground, running underneath Switzerland and France. Its two beams of counter-circulating protons are brought into collision at four points. The four main detectors at the four collision points along the LHC are ATLAS and CMS [63], the two general purpose detectors, LHCb [64], a detector built for b-physics, and ALICE [65], a detector purposed for heavy lead ion collisions. Data from the ATLAS detector were used in this dissertation.

The source of protons in the LHC is a bottle of hydrogen gas. The hydrogen atoms are first stripped of their electrons with an electric field, and the resulting protons are accelerated in Linac 2, the first of a chain of accelerators, up to 50 MeV. They are sent to the Proton Synchrotron Booster, which brings them up to 1.4 GeV, then to the Proton Synchrotron ring, and then to the Super Proton Synchrotron ring, accelerating to 25 GeV and 450 GeV respectively. Finally they are injected into the LHC travelling in two opposite directions. Each are accelerated to 6.5 TeV, delivering a collision energy of 13 TeV for this dataset.

4.2 The ATLAS Detector

The ATLAS detector, located at Point 1 along the LHC ring, has a design particularly suited to measuring the energy and momentum of electromagnetic particles, hadrons,

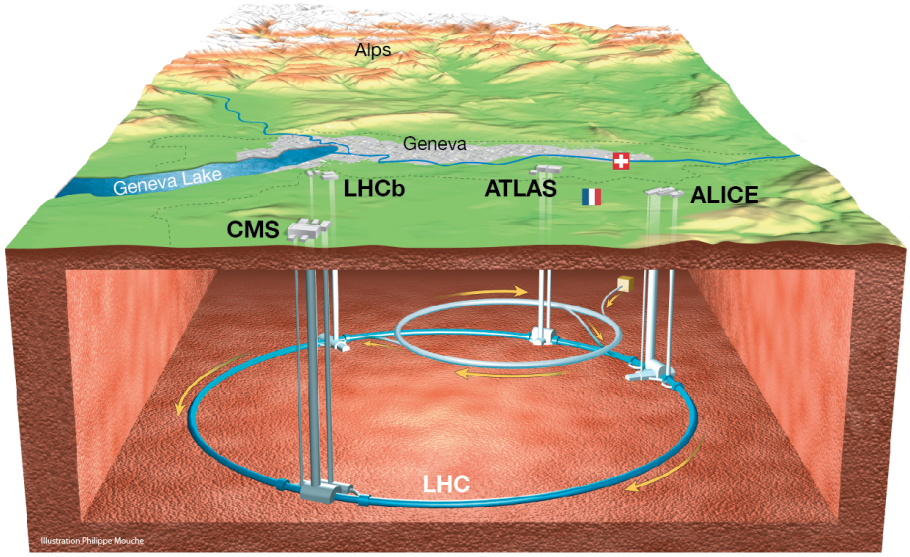

Figure 4.1: A schematic of the Large Hadron Collider [66].

and muons. These features make it an excellent tool for measuring the Z boson decaying to electron-positron or muon-antimuon pairs in conjunction with missing energy, and searching for possible new physics with that signature. The specifications and performance of the ATLAS detector and its individual components can be found in [8], and the citations contained therein. The pieces most relevant for the search for dark matter are detailed below.

The ATLAS detector is depicted schematically in Figure 4.2. It has four layers: the inner detector is positioned right next to the beam pipe; wrapped around the inner detector are the two calorimeters – electromagnetic first, and then hadronic; finally, the outermost layer is the muon spectrometer. Each of these sections has an azimuthal, or ϕ-symmetric 'barrel' component, which provides hermetic coverage perpendicular to the beam pipe. An extended 'end-cap' component increases the angular coverage towards the beam pipe. The ATLAS coordinate system defines the z-axis by the beam direction, with the plane transverse to the beam direction defining the x- (inward) and y- (upward) axes. The angular measurements ϕ and θ represent the azimuthal angle (measured around the beam axis) and the polar angle (angle from the beam axis). The pseudorapidity, η, used as the angular measurement from the beam pipe is defined as $\eta = -\ln(\tan(\theta/2))$.

4.2.1 The Inner Detector

The inner detector (ID) [67] measures the trajectory of charged particles. The signature of the trajectory is known as a track. Extrapolating tracks to where they meet determines the origin of a track, known as a vertex. This extrapolation to the origin is often referred to as 'vertexing'. Tracking and vertexing are crucial in the identification and measurement of the momentum and charge of electrons and muons. Vertexing is important to identify the origin of the components of the hard scatter in a collision. This is of particular importance when there are multiple collisions, which is the case with the bunches of protons that are collided in the ATLAS detector. The primary vertex has the largest scalar momentum sum. It is crucial to correctly identify it as an essential element of the detector.

This innermost component of ATLAS is surrounded by a solenoid magnet with a strength of 2 T to bend the tracks of charged particles [8]. The ID itself is made up of three layers of finely spaced pixel detectors [68]. In 2014, before the start of Run-2, the pixel detector was upgraded by inserting a fourth layer right next to a reduced diameter beam pipe, called the **i**nsertable **b**-**l**ayer, or IBL [69]. This layer was meant to enhance the tracking and vertexing of the ID. Outside of that are eight layers of the **s**ili**c**on microstrip **t**racker (SCT) [70]. Fully surrounding these are tightly packed straw transition radiation tubes known as the **t**ransition **r**adiation **t**racker (TRT) [71]. The TRT contributes to the measurement of the momenta of particles passing through the ID and identifies electrons through transition radiation.

4.2.2 The Electromagnetic Calorimeter

The Electromagnetic (EM) Calorimeter [73] is a sampling calorimeter [6] designed to precisely measure the energies of photons and electrons incident on the detector [8]. The barrel is built around the ID, hermetic in azimuthal angle, and uses liquid argon (LAr) as the active material with lead absorbers to find the position and energy of clusters from electromagnetic showers [74]. The EM showers ionize the liquid argon, and an electric field causes the ions to drift. The current from the drifting ions is proportional to the energy deposited. The EM Calorimeter electrodes have an accordion-shaped design ensuring azimuthal uniformity which is optimized to have uniform coverage with no gaps while maintaining short readout lines. Motivation for the design of this calorimeter was the ability to distinguish between electrons, photons, and photons that convert into an electron-positron pair before reaching the

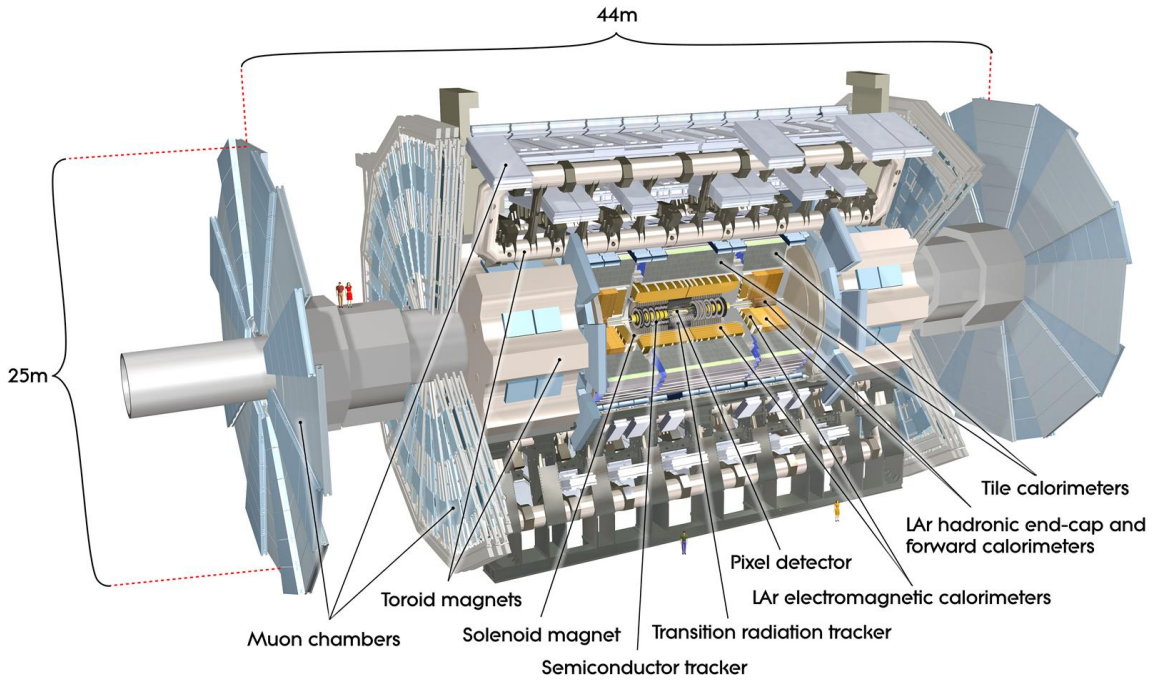

Figure 4.2: Cutaway view of the ATLAS detector, showing the Inner Detector, EM Calorimeter, Hadronic Calorimeter, and the Muon Spectrometer, with their components [72].

calorimeter. The fractional energy resolution of the EM calorimeter is parameterized by the formula

$$\frac{\sigma(E)}{E} = \frac{a}{E} \oplus \frac{b}{\sqrt{E}} \oplus c, \tag{4.1}$$

where a is the noise term, b is the sampling term, and c is the constant term. The values for these terms for the barrel and end-cap calorimeters are described below, and shown in Table 4.1. From these values, the resolution for a 100 GeV electron in the barrel is $\sim 1\%$.

In order to provide extended coverage towards the beam pipe, there are end-caps on each side of the calorimeter, just outside the barrel calorimeter. The resolution of the end-caps is not as good as the barrel, but provides essential coverage of the $|\eta|$ range. The Forward Calorimeter (FCal) [75], which uses LAr ionization with a copper layer followed by two tungsten layers, is located inside the EM end-caps and the hadronic end-caps to provide further $|\eta|$ coverage, and to absorb more radiation.

Detector Component	Resolution	η coverage
EM calorimeter (electrons)		
barrel	$\sigma_E/E = 9.3\%/\sqrt{E} \oplus 0.56\%$	$\|\eta\| < 1.475$
end-cap	$\sigma_E/E = 19.4\%/\sqrt{E} \oplus 0.43\%$	$1.375 < \|\eta\| < 3.2$
EM calorimeter (photons)		
barrel	$\sigma_E/E = 8.6\%/\sqrt{E} \oplus 0.61\%$	$\|\eta\| < 1.475$
end-cap	$\sigma_E/E = 12.2\%/\sqrt{E} \oplus 0.59\%$	$1.375 < \|\eta\| < 3.2$
FCal (electrons)	$\sigma_E/E = 28.5\%/\sqrt{E} \oplus 3.5\%$	$3.1 < \|\eta\| < 4.9$
FCal (hadrons)	$\sigma_E/E = 94.2\%/\sqrt{E} \oplus 7.5\%$	

Table 4.1: Measured resolutions for electrons and photons in the Electronic Calorimeter [8].

4.2.3 The Hadronic Calorimeter

The Hadronic Calorimeter (HCal) [76] is made of three main parts. The central barrel and extended barrel use scintillation tiles as active material and iron absorbers to measure the energy of hadrons in conjunction with the EM calorimeter [8]. The scintillation tiles have fibre readouts to measure the energy deposited by particles passing through. The absorber material also acts as the return yoke of the solenoidal magnetic field. The HCal is optimized to measure the energy of hadronic jets, and contributes to the missing energy calculation. The hadronic end-cap calorimeter (HEC) [77] uses LAr ionization readout and copper absorbers, and is located at each end of the detector. The measured resolution in the various components of the HCal is given in Table 4.2. Using these figures, a jet of 100 GeV in the barrel region has an energy resolution of $\sim 8\%$.

Detector Component	Resolution	η coverage
Hadronic calorimeter (hadrons)		
barrel	$\sigma_E/E = 56.4\%/\sqrt{E} \oplus 5.5\%$	$\|\eta\| < 1.52$
end-cap	$\sigma_E/E = 70.6\%/\sqrt{E} \oplus 5.8\%$	$1.5 < \|\eta\| < 3.2$

Table 4.2: Measured resolutions for jets in the Hadronic Calorimeter [8], [78].

4.2.4 Muon Spectrometer

Finally, surrounding the calorimeters, there is the Muon Spectrometer MS [79], which uses very large toroidal magnets for bending tracks from muons escaping the detector

[8]. In order to precisely determine the position and momentum of high momentum muons, high granularity Monitored Drift Tubes (MDTs) and Cathode Strip Chambers (CSCs) work together with the triggering Resistive Plate Chambers (RPCs) in the barrel and Thin Gap Chambers (TGCs) in the end-caps. The muons also leave charged tracks inside the ID, and this additional piece of information can be combined with the MS recorded information to get an even more precise measurement.

4.2.5 Trigger

Events that occur in the detector are recorded after being selected by a sophisticated, two-tiered data trigger system. At the lowest level, Level-1 (L1), the trigger is hardware only, and looks for either a cluster of energy in the calorimeter (L1EM) [80], or coincidences in the muon chambers (L1MU) [81]. As the event is passed up to the software level, known as the High-Level Trigger (HLT) [82], this selection becomes more refined. (The HLT, used in Run-2, was combined from the Run-1 Level-2 and Event Filter trigger levels [83].) Events that do not pass both levels of trigger are discarded. The L1 trigger is designed to reduce rates to 100 kHz, and the HLT further restricts the rates to ≈ 1 kHz [84]. In an ideal world, data would not have to be discarded, and the rates would be unrestricted. However, it is not feasible to record the amount of information in the large number of interactions occurring per second; moreover, most are uninteresting. As the luminosity of the collider increases, it is not possible to record even all the interesting interactions. Only a fraction of some more frequently occurring triggered interactions are recorded, in a process known as prescaling. There are also unprescaled triggers that do not have overwhelming rates of events being produced, and therefore allow all passing events to be recorded.

For this analysis, events that were triggered by very energetic single electrons or muons were analyzed. The specific electron and muon triggers for this analysis can be found in Table 6.4. ATLAS triggers follow a conventional naming scheme. Electron triggers start with 'e'; muon triggers start with 'm'. This is followed by the HLT threshold in GeV. The identification selection is then given (e.g., loose, lhloose, lhmedium), and then any isolation information (e.g., iloose, ivarmedium). Finally, if it differs from the default, the L1 seed is given for either the electromagnetic (EM) or muon (MU) system. Take for example the trigger e24_lhmedium_nod0_L1EM20VH. The first piece, e24, says that an **e**lectron trigger of at least **24** GeV fired the HLT. The next bits refer to specific algorithms in the trigger for identification, etc. The

final piece, L1EM20VH, says that the **L1EM** trigger fired on **20** GeV of energy being deposited in the calorimeter, while VH refers to additional requirements on the L1 trigger where **V** indicates a threshold variation as a function of pseudorapidity, while **H** is a hadronic calorimeter isolation requirement.

Chapter 5

Dataset and Simulations

5.1 Dataset

Proton-proton collisions were delivered to the ATLAS detector by the LHC in 2015 and 2016, during the recording period called 'Run-2'. The data used in this dissertation were recorded in 2015, and for the period of 2016 up to July 18. The peak instantaneous luminosity of the LHC during this period was $1.2 \times 10^{34}\,\mathrm{cm}^{-2}\,\mathrm{s}^{-1}$. Up to 2496 bunches of protons in each beam, with 25 ns bunch spacing, were collided at an energy of 6.5 TeV per beam, or a centre of mass energy of 13 TeV.

The mean number of interactions per crossing is denoted by μ, and the distribution of μ can be seen in Figure 5.1. The average of μ in a time period is $<\mu>$. In 2015, the mean number of interactions per bunch crossing was $<\mu> \approx 13.5$ (removing the data taken with 50 ns bunch spacing); during 2016, including data up to July 18, the value of $<\mu>$ is ≈ 23. The luminosity-weighted combined $<\mu>$ for each pb^{-1} of data collected in 2015 and 2016 can be seen in Figure 5.1. The total recorded integrated luminosity in 2015 was 3.2 fb^{-1} and for the period of 2016 up to July 18 was 10.1 fb^{-1}, making a combined dataset of 13.3 fb^{-1} used in this dissertation. The total integrated luminosity can be seen in Figure 5.2 for both years (note that only the first $\sim 1/3$ of the total integrated luminosity of 2016 was used).

At 13 TeV, the total cross section for proton-proton interaction is ≈ 100 mb. This is comprised of a quarter elastic collisions, and three-quarters inelastic collisions, of which a third are diffractive. The non-diffractive inelastic collisions, where neither proton remains intact, are the collisions that could produce dark matter and have a cross section for interaction of $\approx$ 50-60 mb [85].

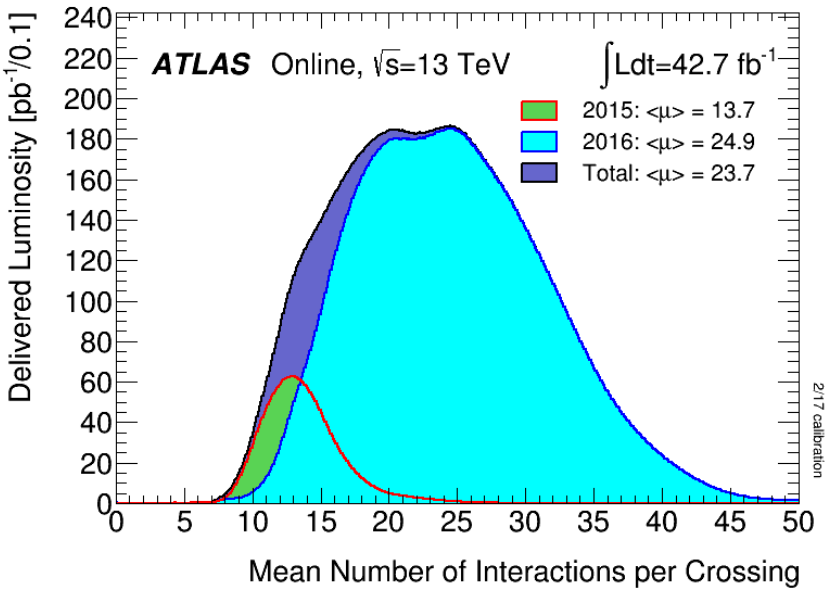

Figure 5.1: Histogram of luminosity-weighted mean number of interactions per crossing (μ) for each pb^{-1} of data collected in 2015 and 2016.

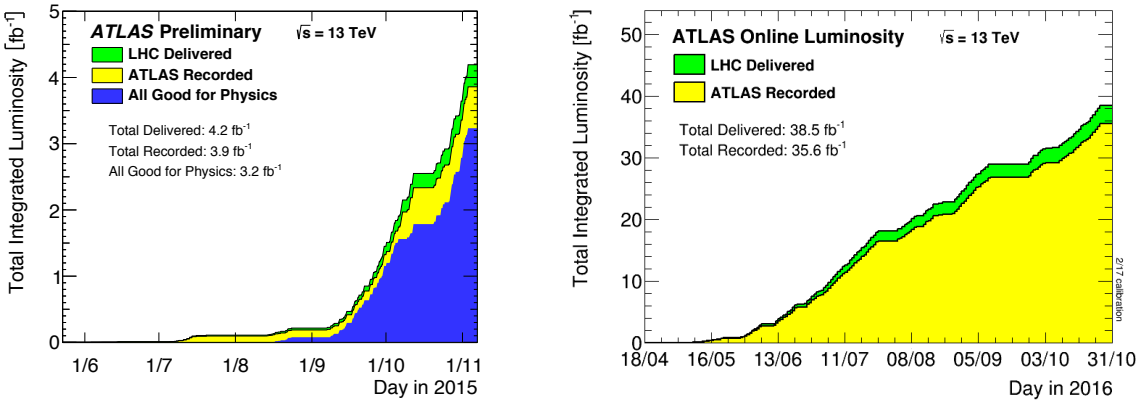

Figure 5.2: Integrated luminosity by day for 2015 (left) and 2016 (right).

5.2 Monte Carlo Modelling

Monte Carlo (MC) background simulations were produced with the generators Madgraph [86], Sherpa [87], or Powheg [88] interfaced with either Pythia v6 [89] or Pythia v8 [90] to model the parton shower and fragmentation.

MC background generated samples were put through a full ATLAS detector simulation based on GEANT4 [91]. These were then reconstructed using the same algorithms that were used for actual data.

5.2.1 Background Samples

In order to investigate what final states could be produced in the ATLAS detector, simulated events are generated of the possible outcomes of the collisions of two protons. The decay products of the possible outcomes are then generated from the particles produced in the initial high momentum transfer. These generated events are then run through a program to evolve in QCD the final state partons down to the GeV-scale, and then hadronize them. These hadronized events, called jets, are then run through a simulation of the ATLAS detector and recorded as a real event would be. Finally, the events are reconstructed, or pieced back together to try and find what different particles were involved in the event by looking at the signatures that they leave in the detector. The reconstruction program produces objects such as jets, electrons, and muons. The MC objects are analyzed and compared to objects in events from collision data. The MC samples used by this analysis can be seen in Table 5.1 through 5.7.

In order to correctly compare MC samples to the data, there are several factors that must be considered. The first is that the number of MC events must be normalized to the total luminosity of the data. The equivalent integrated luminosity of the MC can be found by solving Equation 3.3 for $\int \mathcal{L}\, dt$, where $N = N_{gen}$, or the number of generated MC events, and σ is the cross section of the MC process,

$$\left(\int \mathcal{L}\, dt\right)_{MC} = \frac{N_{gen}}{\sigma_{MC}}. \tag{5.1}$$

MC samples are often generated with a filter, such as a requirement on the lower transverse momentum for the partons, so that fewer unimportant events are generated. This means that the cross section of the sample is actually smaller than the full physics process. The cross section in Equation 5.1 must therefore be multiplied

by the generator filter efficiency, ϵ_{filt}.

Another factor that must be accounted for is pileup. Because of the very large number of protons in any given bunch that is collided in the accelerator, there may be multiple collisions in the detector at the same time; see Chapter 4. This leads to multiple collisions, seen as multiple hard-scatter vertices in the event. The MC simulation tries to account for this, but will not be perfect, as pileup is luminosity dependent, and will change as the data-taking progresses. Therefore, a run-by-run correction of pileup is made to the MC by reweighting events according to the number of primary vertices in each event, and the average number of interactions for each proton bunch collided in the detector.

Diboson

The diboson backgrounds (ZZ, WZ, WW) are the largest backgrounds to the analysis. The simulations for the diboson backgrounds were performed with Powheg + Pythia8. They are listed in Table 5.1.

Diboson

Process	Sample	Type	Generator	σ[pb]	N_{gen}	ϵ_{filt}
$gg \to ZZ$	343233	$ZZ \to \ell\ell\nu\nu$	PowhegPythia8	0.10323	100k	1.00
$qq \to ZZ$	361603	$ZZ \to \ell\ell\ell\ell$	PowhegPythia8	0.10323	100k	1.00
	361604	$ZZ \to \ell\ell\nu\nu$	PowhegPythia8	0.10323	100k	1.00
	361605	$ZZ \to \nu\nu\nu\nu$	PowhegPythia8	0.10323	100k	1.00
WZ	361601	$WZ \to \ell\nu\ell\ell$	PowhegPythia8	1.179	100k	1.00
	361602	$WZ \to \ell\nu\nu\nu$	PowhegPythia8	1.179	200k	1.00
	361607	$WZ \to qq\ell\ell$	PowhegPythia8	1.179	200k	1.00
	361609	$WZ \to \ell\nu qq$	PowhegPythia8	1.179	199.5k	1.00
WW	361600	$WW \to \ell\nu\ell\nu$	PowhegPythia8	2.3540	198.5k	0.27156
	361606	$WW \to \ell\nu qq$	PowhegPythia8	1.5590	199.5k	0.32575

Table 5.1: Monte Carlo background samples for diboson processes.

Z+jets

The Z+jets background is one of the most challenging backgrounds to model, as is the case for multiple jets events. While it only makes up $\approx 10\%$ of the background,

the uncertainty on this background dominates the precision at which the analysis can be performed. The samples were simulated with Madgraph slices given by the number of partons, as shown in Table 5.2, and slices given by the total scalar sum of the energy in Tables 5.3 and 5.4. Both complete sets of Z+jets samples were averaged for the analysis. The samples sliced by number of partons suffered from a minor bug in which the muon mass was set to zero. However, given the statistics needed for the analysis, and an insufficient timescale for reproduction of the whole dataset, they were included in the search after the impact on the signal region was observed to be insignificant relative to the errors.

$Z \to \ell\ell$

Process	Sample	Name	Generator	σ (pb)	k-factor	ϵ_{filt}
$Z \to ee$ + jets	361500	Np0	MADGRAPH	1401.6	1.232	1.0
	361501	Np1	MADGRAPH	211.99	1.232	1.0
	361502	Np2	MADGRAPH	67.305	1.232	1.0
	361503	Np3	MADGRAPH	18.68	1.232	1.0
	361504	Np4	MADGRAPH	7.29	1.232	1.0
$Z \to \mu\mu$ + jets	361505	Np0	MADGRAPH	1402.0	1.232	1.0
	361506	Np1	MADGRAPH	211.95	1.232	1.0
	361507	Np2	MADGRAPH	67.353	1.232	1.0
	361508	Np3	MADGRAPH	18.633	1.232	1.0
	361509	Np4	MADGRAPH	7.3013	1.232	1.0
$Z \to \tau\tau$ + jets	361510	Np0	MADGRAPH	1397.8	1.232	1.0
	361511	Np1	MADGRAPH	211.4	1.232	1.0
	361512	Np2	MADGRAPH	67.176	1.232	1.0
	361513	Np3	MADGRAPH	18.609	1.232	1.0
	361514	Np4	MADGRAPH	7.275	1.232	1.0

Table 5.2: MC background samples for Z+jets processes sliced by number of partons in the final state.

Top Quark

The top quark backgrounds includes any process containing a t-quark. This includes processes from: $t\bar{t}$, single t, Wt, $t\bar{t}$ $+V$, and $t\bar{t}$ $+VV$. The modelling was performed with Powheg+Pythia and the samples are listed in Table 5.5.

$Z \to \mu\mu$

Process	Sample	E [GeV]	HF	Generator	σ[pb]	k-factor	ϵ_{filt}
	363123	0-70	$\not{C}\,\not{B}$	MADGRAPH	1714.5	1.141	0.83157
	363124	0-70	$C\,\not{B}$	MADGRAPH	1715.5	1.141	0.10835
	363125	0-70	B	MADGRAPH	1715.7	1.141	0.05916
	363126	70-140	$\not{C}\,\not{B}$	MADGRAPH	84.539	1.141	0.71802
	363127	70-140	$C\,\not{B}$	MADGRAPH	84.511	1.141	0.17357
	363128	70-140	B	MADGRAPH	84.807	1.141	0.10768
	363129	140-280	$\not{C}\,\not{B}$	MADGRAPH	35.731	1.141	0.67636
	363130	140-280	$C\,\not{B}$	MADGRAPH	35.907	1.141	0.20006
	363131	140-280	B	MADGRAPH	35.798	1.141	0.12654
	363132	280-500	$\not{C}\,\not{B}$	MADGRAPH	8.173	1.141	0.62684
	363133	280-500	$C\,\not{B}$	MADGRAPH	8.206	1.141	0.22641
$Z \to \mu\mu$	363134	280-500	B	MADGRAPH	8.174	1.141	0.14276
	363135	500-700	$\not{C}\,\not{B}$	MADGRAPH	1.253	1.141	0.59567
	363136	500-700	$C\,\not{B}$	MADGRAPH	1.253	1.141	0.25547
	363137	500-700	B	MADGRAPH	1.276	1.141	0.15225
	363138	700-1000	$\not{C}\,\not{B}$	MADGRAPH	0.436	1.141	0.57118
	363139	700-1000	$C\,\not{B}$	MADGRAPH	0.446	1.141	0.25948
	363140	700-1000	B	MADGRAPH	0.445	1.141	0.15965
	363141	1000-2000	$\not{C}\,\not{B}$	MADGRAPH	0.149	1.141	0.54908
	363142	1000-2000	$C\,\not{B}$	MADGRAPH	0.146	1.141	0.27164
	363143	1000-2000	B	MADGRAPH	0.147	1.141	0.17299
	363144	2000+	$\not{C}\,\not{B}$	MADGRAPH	0.006	1.141	0.56337
	363145	2000+	$C\,\not{B}$	MADGRAPH	0.006	1.141	0.29294
	363146	2000+	B	MADGRAPH	0.006	1.141	0.16307

Table 5.3: MC background samples for Z+jets processes (where the Z decays to $\mu^+\mu^-$) sliced by total energy (E [GeV]) and number of heavy flavour (HF) quarks in the final state. In this table, B and C indicate the presence of the b- or c-quark respectively. $\not{B}$ and $\not{C}$ indicate the vetoing of the b- or c-quark respectively.

$Z \to ee$

Process	Sample	E [GeV]	HF	Generator	σ[pb]	k-factor	ϵ_{filt}
	363147	0-70	$\not{C}\ \not{B}$	MADGRAPH	1719.7	1.141	0.83292
	363148	0-70	$C\ \not{B}$	MADGRAPH	1719.4	1.141	0.10775
	363149	0-70	B	MADGRAPH	1719.4	1.141	0.59156
	363150	70-140	$\not{C}\ \not{B}$	MADGRAPH	85.105	1.141	0.71754
	363151	70-140	$C\ \not{B}$	MADGRAPH	85.041	1.141	0.17377
	363152	70-140	B	MADGRAPH	85.175	1.141	0.10763
	363153	140-280	$\not{C}\ \not{B}$	MADGRAPH	36.005	1.141	0.67279
	363154	140-280	$C\ \not{B}$	MADGRAPH	36.028	1.141	0.19996
	363155	140-280	B	MADGRAPH	36.060	1.141	0.12486
	363156	280-500	$\not{C}\ \not{B}$	MADGRAPH	8.2054	1.141	0.62864
	363157	280-500	$C\ \not{B}$	MADGRAPH	8.2126	1.141	0.22726
$Z \to ee$	363158	280-500	B	MADGRAPH	8.2474	1.141	0.14193
	363159	500-700	$\not{C}\ \not{B}$	MADGRAPH	1.2733	1.141	0.5966
	363160	500-700	$C\ \not{B}$	MADGRAPH	1.2730	1.141	0.24847
	363161	500-700	B	MADGRAPH	1.2722	1.141	0.15256
	363162	700-1000	$\not{C}\ \not{B}$	MADGRAPH	0.4455	1.141	0.57676
	363163	700-1000	$C\ \not{B}$	MADGRAPH	0.4461	1.141	0.26137
	363164	700-1000	B	MADGRAPH	0.4460	1.141	0.16181
	363165	1000-2000	$\not{C}\ \not{B}$	MADGRAPH	0.1521	1.141	0.55543
	363166	1000-2000	$C\ \not{B}$	MADGRAPH	0.1525	1.141	0.27476
	363167	1000-2000	B	MADGRAPH	0.1533	1.141	0.16618
	363168	2000+	$\not{C}\ \not{B}$	MADGRAPH	0.0057	1.141	0.53136
	363169	2000+	$C\ \not{B}$	MADGRAPH	0.0057	1.141	0.29230
	363170	2000+	B	MADGRAPH	0.0057	1.141	0.17489

Table 5.4: MC background samples for Z+jets processes (where the Z decays to e^+e^-) sliced by total energy (E [GeV]) and number of heavy flavour (HF) quarks in the final state. In this table, B and C indicate the presence of the b- or c-quark respectively. $\not{B}$ and $\not{C}$ indicate the vetoing of the b- or c-quark respectively.

Top quark

Process	Sample	Name	Generator	σ[pb]	N_{gen}	ϵ_{filt}
$t\bar{t}$	410000	nonallhad	PowhegPythia	3.3514	999.5k	1.00
	410009	dilepton	PowhegPythia	68.459	958.5k	1.00
Wt	410015	dilepton top	PowhegPythia	3.3514	999.5k	1.00
	410016	dilepton anti top	PowhegPythia	68.459	958.5k	1.00
$ttV(V)$	410066	ttW Np0	PowhegPythia8	3.3514	999.5k	1.00
	410067	ttW Np1	PowhegPythia8	3.3514	999.5k	1.00
	410068	ttW Np2	PowhegPythia8	3.3514	999.5k	1.00
	410069	ttZ Np0	PowhegPythia8	3.3514	999.5k	1.00
	410070	ttZ Np1	PowhegPythia8	68.459	958.5k	1.00
	410081	$ttWW$	PowhegPythia8	3.3514	999.5k	1.00
single t	410025	s-chan top	PowhegPythia	25.778	1000k	1.00
	410026	s-chan anti top	PowhegPythia	43.775	999k	1.00
	410011	t-chan top	PowhegPythia	25.778	1000k	1.00
	410012	t-chan anti top	PowhegPythia	43.775	999k	1.00

Table 5.5: MC samples for backgrounds that include a t-quark.

W+jets

The W+jets background is almost non-existent after all analysis selections are applied. There is negligible contribution in the final signal region. However, it is present in some control regions, so it needs to be modelled. The MC samples for this background were simulated with Powheg+Pythia and are listed in Table 5.6.

$W \to \ell\nu$

Process	Sample	Name	Generator	σ[pb]	N_{gen}	ϵ_{filt}
W+jets	361100	$W^+ \to e\nu$	PowhegPythia8	11302	5359k	1.00
	361101	$W^+ \to \mu\nu$	PowhegPythia8	11302	5997k	1.00
	361102	$W^+ \to \tau\nu$	PowhegPythia8	11302	4969.5k	1.00
	361103	$W^- \to e\nu$	PowhegPythia8	8280.0	5992k	1.00
	361104	$W^- \to \mu\nu$	PowhegPythia8	8280.0	5998.5k	1.00
	361105	$W^- \to \tau\nu$	PowhegPythia8	8280.0	4997.5k	1.00

Table 5.6: MC samples for the W+jets background.

Triboson

The triboson backgrounds have a very low cross section, but can imitate the expected signal, and need to be modelled, as the dark matter signal may also be very small. These processes were modelled with Sherpa and are listed in Table 5.7.

Triboson

Process	Sample	Name	Generator	σ[fb]	N_{gen}	ϵ_{filt}
VVV	361620	$WWW \to 3\ell 3\nu$	Sherpa	8.343	59.8k	1.00
	361622	$WWZ \to 2\ell 4\nu$	Sherpa	3.430	59.8k	1.00
	361621	$WWZ \to 4\ell 2\nu$	Sherpa	1.734	59.6k	1.00
	361624	$WZZ \to 3\ell 3\nu$	Sherpa	1.925	49.8	0.44444
	361623	$WZZ \to 5\ell 1\nu$	Sherpa	0.21783	49.8k	1.00
	361627	$ZZZ \to 2\ell 4\nu$	Sherpa	0.44530	35k	0.44815
	361626	$ZZZ \to 4\ell 2\nu$	Sherpa	0.44125	34.6k	0.22542
	361625	$ZZZ \to 6\ell 0\nu$	Sherpa	0.01706	35k	1.00

Table 5.7: MC samples for triboson processes.

5.2.2 Signal Modelling

Of the theoretical models laid out in Section 3, the ones presented here correspond to the Lagrangians shown in Table 3.3 for the vector mediated simplified model. The vector mediated signal grid shown in Table 5.8 was modelled with Madgraph + Pythia8 for event generation and parton showering. The version of Pythia was A14 NNPDF30 at leading order. For each mediator mass in the first column, a sample was generated with the dark matter masses indicated in its row.

The model was generated with many different mass points of the mediator and the dark matter. The sensitivity of the analysis to any sample is dependent on the cross section of the process and the kinematics determined by the masses. The analysis is more sensitive to the kinematics of the points with higher mediator masses, though this is offset by those samples having smaller cross sections. These trends can be seen in Table 5.9, which shows the models with a dark matter mass of 1 GeV for all of the generated mediator masses. The cross section decreases with increasing mediator mass but the filter efficiency (a $E_{\mathrm{T}}^{\mathrm{miss}}$ filter of 40 GeV) increases.

The signal points were chosen in order to allow comparisons to be possible through a combination of results with other searches, and to cover the full range of masses that are accessible at the energy and integrated luminosity provided from the LHC in this dataset.

Vector mediated dark matter models											
m_{med} [GeV]	m_χ [GeV]										
10	1	10	30	50		150				500	1000
50	1		30								
95				50							
100	1	10	30	55	100						
150			25		80						
200	1			50	105	150					
250						130					
295						150					
300	1	10	30	50	100	155	200				
350							180				
400	1			50	100	150	205	250			
450								230			
500	1	10	30	50	100		200	255	280		
550									280		
600	1			50			200				
700	1		30	50	100		200		300		
800	1				100		200		300		
995										500	
1000						150					1000
1995											1000
2000	1									500	
10000		10								500	

Table 5.8: The grid of 68 simulated mass points for different mediator masses (m_{med}) and dark matter masses (m_χ) in the vector mediated dark matter models. For each of these points, 10k events were generated (aside from the (50, 95) and (500, 995) points (m_χ, m_{med}), where 20k events were generated).

Vector mediated dark matter models for $m_\chi = 1$ GeV				
Sample	m_{med} [GeV]	m_χ [GeV]	σ[pb]	Gen ϵ_{filt}
303511	10	1	11550.0	0.11699
306080	50	1	1403.5	0.45496
303512	100	1	468.2	0.65181
306085	200	1	142.4	0.78542
303513	300	1	63.97	0.82645
306093	400	1	31.87	0.85903
305710	500	1	18.28	0.87827
306103	600	1	11.36	0.88253
305711	700	1	7.416	0.89534
306109	800	1	5.016	0.90147
303514	2000	1	0.1636	0.93449

Table 5.9: Details for samples generated with a dark matter mass (m_χ) of 1 GeV.

Chapter 6

Analysis Selection and Optimization

The goal of the analysis is to find the first evidence of the particle nature of dark matter. Equation 6.1 gives the signal cross section, σ_{sig}, calculated from the total number of observed events, N_{total}, subtracting the number of background events, $N_{\text{background}}$, for the selection efficiency times detector acceptance ($\epsilon_{\text{tot}} \times A_{\text{MC}}$), defined as the number of events passing the selection requirements, all normalized to the integrated luminosity, $\int \mathcal{L}\, dt$, of the data collected at the ATLAS detector. The total acceptance times efficiency of the event selection and reconstruction is required to find the total cross section:

$$\sigma_{\text{signal}} = \frac{\left(N_{\text{total}} - N_{\text{background}}\right)}{\epsilon_{\text{tot}}\, A_{\text{MC}} \int \mathcal{L}\, dt}. \tag{6.1}$$

This problem can be turned around if the cross section is estimated using MC techniques. If the cross section for a process is known, the number of expected events, N, can be estimated from

$$N = \sigma\, \epsilon\, A \int \mathcal{L}\, dt. \tag{6.2}$$

Knowing how many events are expected from a particular signal or background model will allow a statement to be made on the number of events expected to be observed, and whether or not the signal can be distinguished from the background.

6.1 Physics Objects

In order to find a candidate dark matter event, the constituent objects of such an event must be identified in the detector. When a particle passes through the ATLAS detector, the energy it deposits and the tracks it leaves give clues to what kind of object it is. The Mono-Z event is made up of the following identifiable objects: charged lepton pairs – either electron-positron pairs (e^+e^-) or muon-antimuon pairs ($\mu^+\mu^-$) – missing transverse momentum ($E_{\mathrm{T}}^{\mathrm{miss}}$), and jets. Jets can be further classified based on whether they are identified as originating from a heavy b-quark (b-jet), as the candidate events will be excluded if the events include a b-jet with significant energy. Lepton, jet, and $E_{\mathrm{T}}^{\mathrm{miss}}$ objects are found using a set of criteria, or cuts, called object selection cuts. The choice of cuts will determine the quality of the objects and affect the feasibility of identifying a candidate Mono-Z event.

6.1.1 Electrons

Reconstructed electrons (for a complete ATLAS definition of electron objects see [92]) are identified in the data event by event by examining signals in the calorimeter and tracks in the ID. Every electron from data or MC has corrections, determined from data, applied to the energy and position [93]. These corrections are taken from the actual performance of the detector relative to its expected or past performance in the reconstruction algorithm.

The total number of electrons at the start of the selection comprises the bins `ALL`, containing the total electrons as seen in Figure 6.1. (These electrons have already had discrimination from photons applied, so the bin `AUTH`, that discriminates between electrons and photons, does not remove any objects.) The electrons are then required to pass a likelihood 'loose' cut (`LLoose`), which uses shower shape information and track requirements to select electrons while rejecting hadronic activity. They are then required to have a transverse momentum $p_{\mathrm{T}} > 7$ GeV (`ET7`), with a direction of $|\eta| < 2.47$ (`ETA`). They are required to have good object quality with regards to the originating energy cluster (`OQ`), and that their tracks come from the primary vertex of the event (`VTX`), which is selected using impact parameters d_0 significance < 5 and $z_0 \sin(\theta) < 0.5$ mm. After this step, any overlap between the electron and other objects is taken care of by the procedure outlined in Section 6.1.4 (`OR`). After the overlap is removed, the selection on the remaining electrons and positrons is tightened to require $p_{\mathrm{T}} > 20$ GeV (`PT20`), and have a likelihood 'medium' cut (`LMed`).

A summary of these selection criteria can be found in Table 6.1. The number of electrons and positrons remaining after each of these criteria, an 'object cutflow', for an MC sample can be seen in Figure 6.1.

After passing the object cutflow, electrons have scale factors applied to correct for the relative efficiencies from data/MC comparisons. These are calculated by dedicated working groups for a variety of working points, and are multiplied together. Different scale factors exist for reconstruction, identification, isolation, and trigger efficiencies. They have associated uncertainties that will be discussed in Chapter 8 [94].

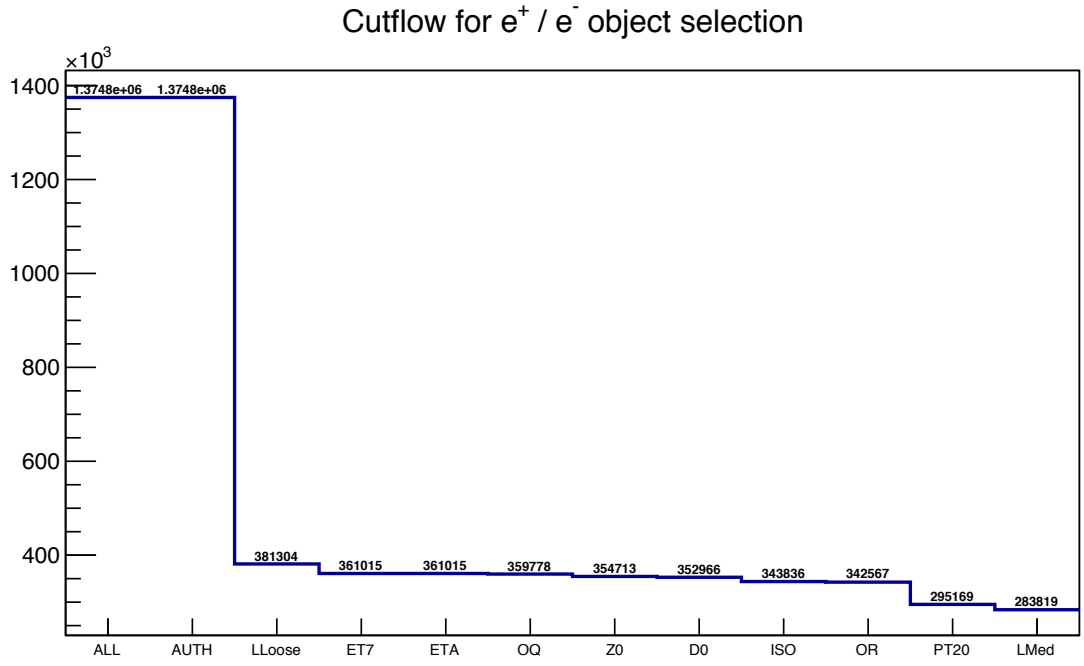

Figure 6.1: The number of electrons passing the object selection cuts in a MC sample of $gg \to ZZ$ (sample identification 343233 from Table 5.1), where one Z decays to charged leptons, and the other Z to neutrinos: $ZZ \to \ell^+\ell^-\bar{\nu}\nu$.

The plots in Figures 6.2 and 6.3 were made using a MC sample (sample identification 343233 from Table 5.1) that contains events generated from gluon-gluon fusion that decays into a Higgs particle, which subsequently decays into two Z bosons where one decays to either an electron-positron pair or muon-antimuon pair, and the other to a neutrino-antineutrino pair, $gg \to ZZ$, $ZZ \to e^+e^-\bar{\nu}\nu$ or $ZZ \to \mu^+\mu^-\bar{\nu}\nu$. The transverse momentum of the two highest p_{T} electrons in the event are plotted in Figure 6.2. Shown there is the p_{T} of the candidate ZZ events reconstructed from 1) e^+e^- pairs that have not passed any of the electron object criteria, and they are

Identification	Likelihood Medium ID (Likelihood Loose ID before overlap removal)
Object Quality	Good quality
Kinematic cuts	$p_{\mathrm{T}} > 20$ GeV ($p_{\mathrm{T}} > 7$ GeV before overlap removal) $\lvert\eta\rvert < 2.47$
Cosmic / pileup cuts	$\lvert d_0 \text{ significance}\rvert < 5$ $\lvert z_0 \sin(\theta)\rvert < 0.5$ mm
Isolation	Loose

Table 6.1: Summary of electron selections.

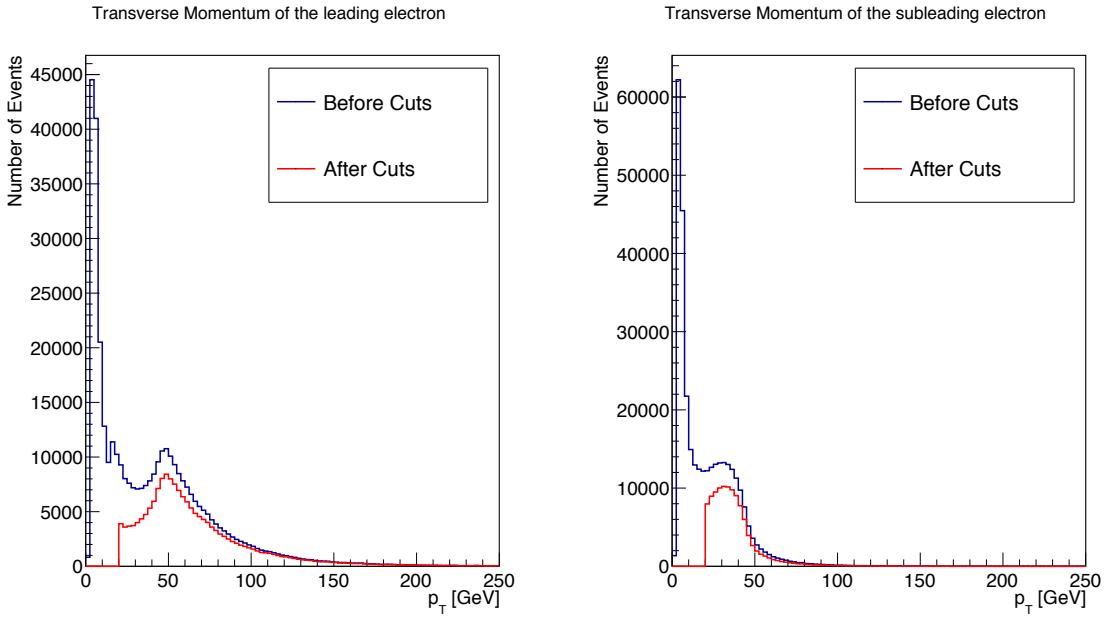

Figure 6.2: First- (left) and second-highest p_{T} (right) electron transverse momentums in a MC sample of $gg \to ZZ$. The blue line shows the electrons before all the object selection criteria have been applied, and the red line shows the electrons after all the object selections are applied.

compared to the candidates reconstructed from 2) e^+e^- pairs that have passed the electron object criteria. By comparing the two plots, it is apparent that the object selection cuts remove many of the low momentum electrons. Low momentum e^+e^- pairs will not produce much $E_{\mathrm{T}}^{\mathrm{miss}}$, and will be indistinguishable from the background.

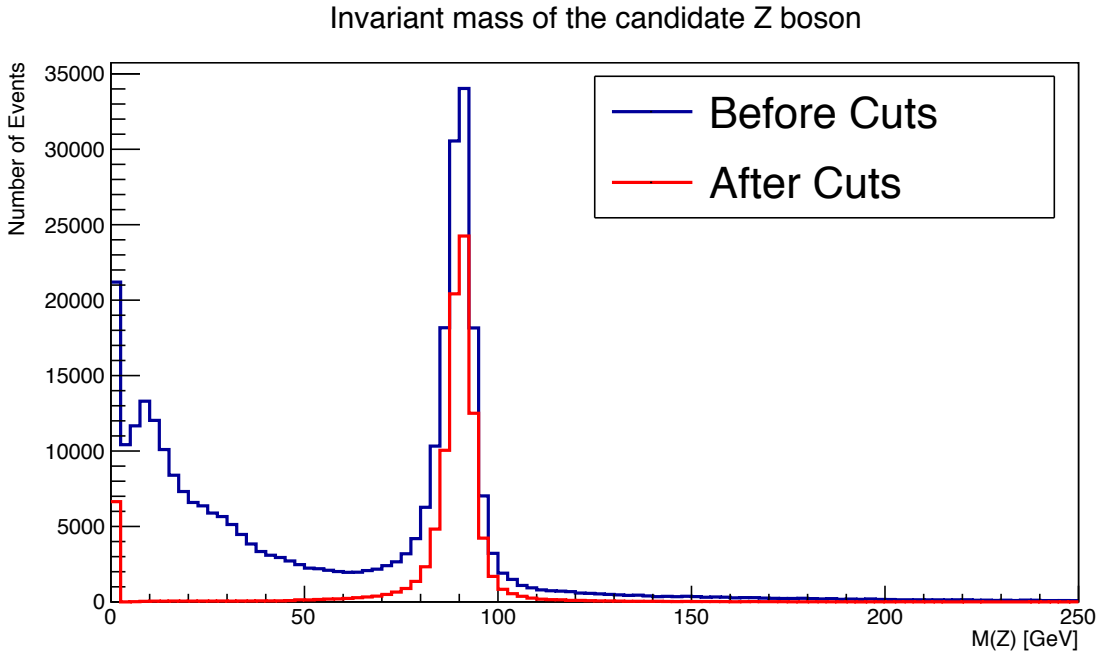

Figure 6.3: Invariant mass of the four-vector addition of the first- and second-highest p_{T} electrons in a MC sample of $gg \to ZZ$. The blue line shows the invariant mass of the electrons before any of the selection criteria have been applied, and the red line shows the invariant mass of the electrons in the sample after all selections are applied.

The candidate Z bosons reconstructed from e^+e^- pairs passing object selection will be used to determine if it is a candidate Mono-Z event. As seen in Figure 6.3, after an electron-positron pair have been selected, the invariant mass of the pair is added to a histogram, where the Z peak is observed. Considering that the MC sample is a diboson sample and most, if not all, of the hard scatter electrons and positrons will come from a Z decay, it is expected that their invariant mass will peak around the Z mass. This $gg \to ZZ$ is a part of the irreducible background being studied here. It primarily contains events that look like the signal, and so exhibits the same behaviour expected for the Mono-Z signals. The electrons passing all of the object selection cuts are found to be the ones near the mass peak of the Z boson, while the ones being cut out are the low energy electrons which will not produce much $E_{\mathrm{T}}^{\mathrm{miss}}$.

For the $gg \to ZZ$ sample, the events should have very little transverse momentum boost, and so the Z bosons are produced back to back. When one Z decays to $\nu\bar{\nu}$ yielding $E_{\mathrm{T}}^{\mathrm{miss}}$, the other Z boson's momentum should be equal to (but in the opposite direction of) the $E_{\mathrm{T}}^{\mathrm{miss}}$ in the event. This can be seen in Figure 6.4. The distributions are plotted on the same graph in order to compare their shapes. The agreement is much better after the objects are selected as the object selection cuts eliminate electrons in the event that may come from soft radiation, or perhaps originate from the underlying event being loosely reconstructed as an electromagnetic object.

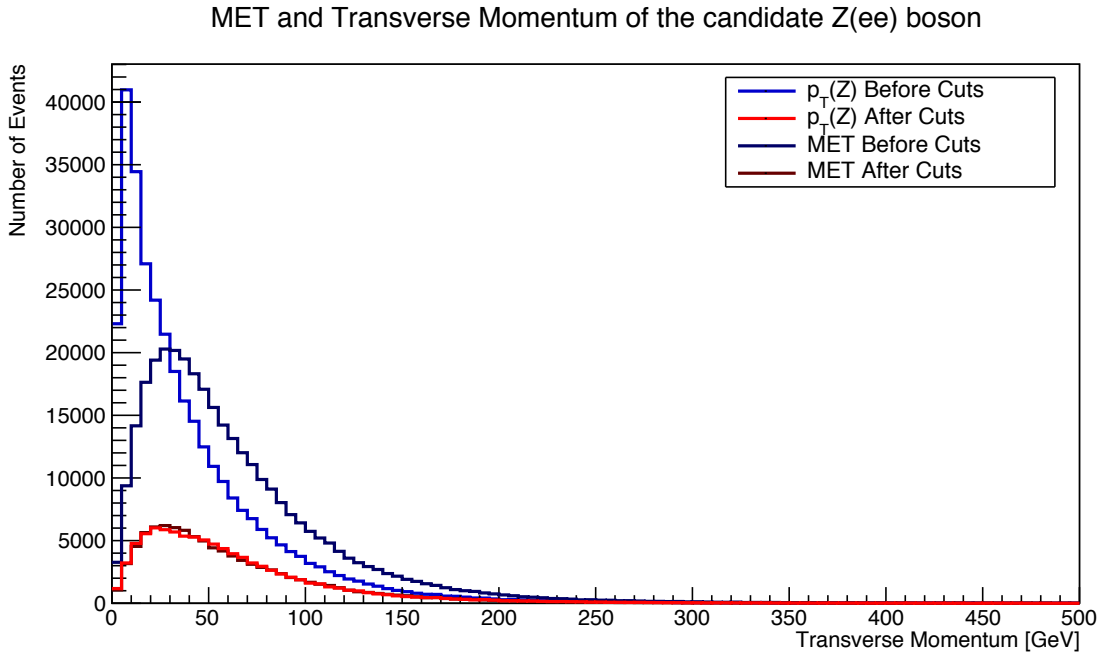

Figure 6.4: Comparison of the p_{T} ($Z \to e^+e^-$) and the missing transverse momentum in a MC sample of $gg \to ZZ$ after all of the object selection cuts have been performed, and keeping events with two selected electrons. The red (p_{T} ($Z \to e^+e^-$)) and dark red ($E_{\mathrm{T}}^{\mathrm{miss}}$) distributions show very good agreement after keeping events with two selected electrons.

6.1.2 Muons

Reconstructed muons (for a complete ATLAS definition of muon objects see [95]) are identified in the data event by event by examining signals in the Muon Spectrometer. Every muon from MC has corrections, determined from data, applied to the energy and position. As with the electrons, these corrections are from the actual performance

of the detector relative to its expected or past performance in the reconstruction algorithm.

Candidate muons are required to pass a loose quality selection criterion or 'cut', (`Loose`), designed to maximize reconstruction efficiency. They are then required to be of the type Combined Muon (`COMB`) – one that produces a full track in both the inner detector and muon spectrometer. They are required to have $p_{\mathrm{T}} > 7$ GeV (`ET7`), and $|\eta| < 2.5$, with sufficient hits in the pixel, silicon, and transition radiation tracker portions of the detector (`TRK`) (this track cut is included in the combined muon definition and so does not remove any muon objects). They are also required to have a track that comes from the primary vertex, which is strengthened using impact parameters $z_0 \sin(\theta) < 0.5$ mm (`Z0`) and d_0 significance < 3 (`D0`). Any muon overlapping with a jet ($\Delta R < 0.2$) is removed (`OR`), and isolated from other activity in the detector (`ISO`). The remaining muons are required to have a $p_{\mathrm{T}} > 20$ GeV (`PT20`), and a quality of 'medium' (`Med`). A summary of these selections is seen in Table 6.2. The object cutflow for muons and antimuons remaining after each of these criteria can be seen in Figure 6.5.

Muons, similar to electrons, have scale factors applied to MC events to correct for the relative efficiencies from data/MC. These are calculated by dedicated working groups for a variety of working points, and are multiplied together. Different scale factors exist for reconstruction, isolation, and trigger efficiency. They have associated uncertainties that will be discussed in Chapter 8 [95].

Identification	Combined with Medium Quality (Combined with Loose Quality before overlap removal)
Object Quality	Good quality
Kinematic cuts	$p_{\mathrm{T}} > 20$ GeV ($p_{\mathrm{T}} > 7$ GeV before overlap removal) $\lvert\eta\rvert < 2.5$
Cosmic cuts	$\lvert d_0$ significance$\rvert < 3$ $\lvert z_0 \sin(\theta)\rvert < 0.5$ mm
Isolation	Loose

Table 6.2: Summary of muon selections.

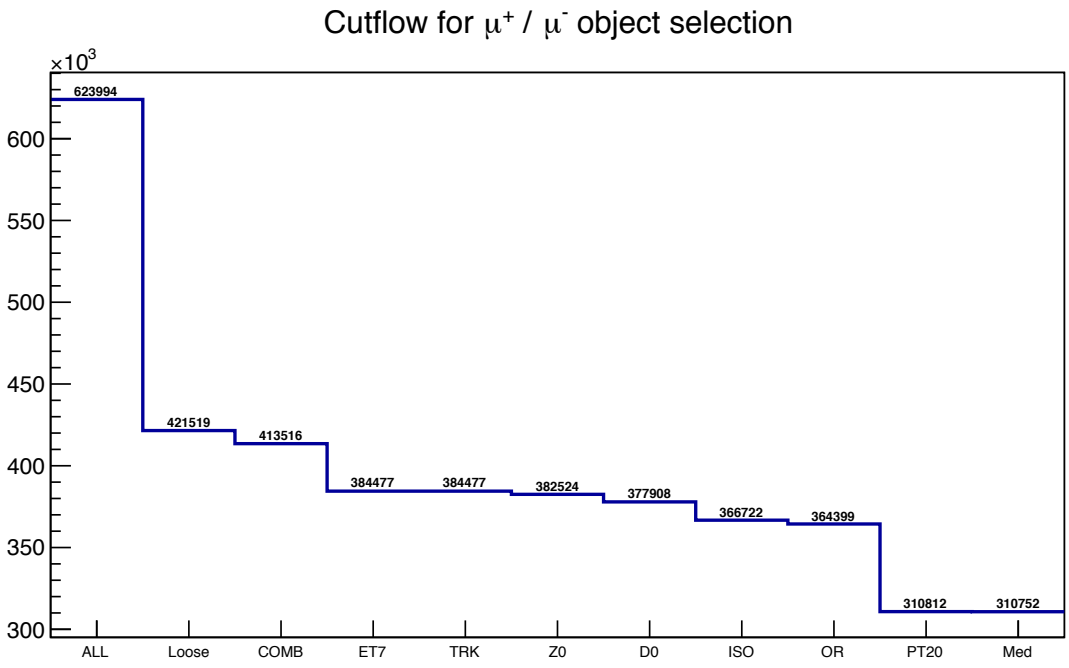

Figure 6.5: The number of muons passing the object selection cuts in a MC sample of $gg \to ZZ$ (sample identification 343233 from Table 5.1), where one Z decays to charged leptons, and the other Z to neutrinos: $ZZ \to \ell^+\ell^-\bar{\nu}\nu$.

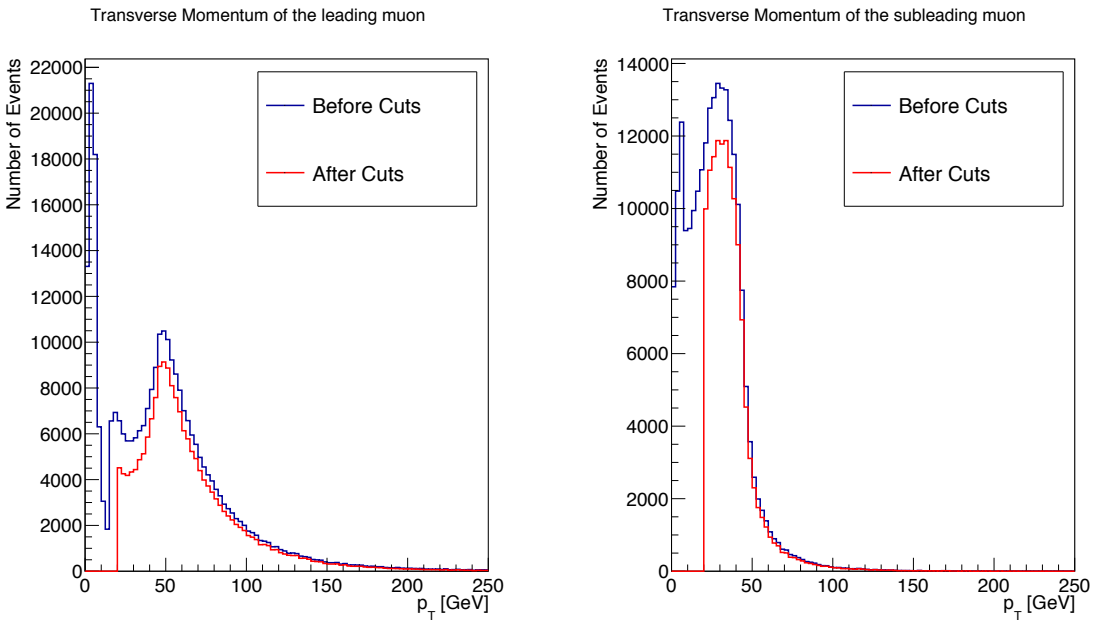

Figure 6.6: First- (left) and second-highest (right) muon transverse momentums in a MC sample of $gg \to ZZ$. The blue line shows the muons before all the object selection criteria have been applied, and the red line shows the muons after all the object selections are applied.

The transverse momentum of the two highest p_{T} muons in the event is plotted in Figure 6.6. Shown there is the p_{T} of the candidate ZZ events reconstructed from 1) $\mu^+\mu^-$ pairs that have not passed any of the muon object criteria, and they are compared to the candidates reconstructed from 2) $\mu^+\mu^-$ pairs that have passed the muon object criteria. By comparing the two plots, it is apparent that the object selection cuts remove the low momentum muons that will not produce much $E_{\mathrm{T}}^{\mathrm{miss}}$ and therefore are not interesting to the analysis.

Similar to candidate Z bosons reconstructed from e^+e^-, the candidate pairs passing the object selection reconstructed from $\mu^+\mu^-$ will also be used to determine whether this is a candidate Mono-Z event, as seen in Figure 6.7. The invariant mass of the selected muon-antimuon pair have been selected are also observed to be largely consistent with the mass of the Z. The muons passing all of the object selection cuts can be seen to be those near the mass peak of the Z boson, while the ones being removed are the low energy muons, likely not originating from a Z decay.

For the $gg \to ZZ$ sample, the events should have very little transverse momentum boost, and so the Z bosons should be produced back to back. When one Z decays

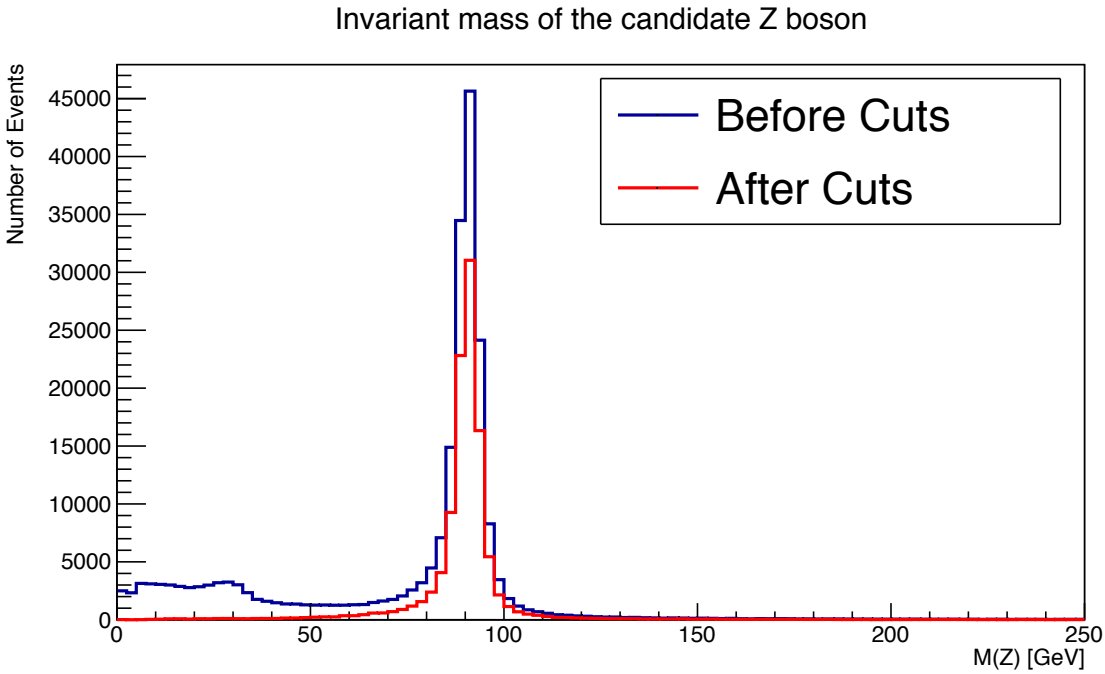

Figure 6.7: Invariant mass of the four-vector addition of the first- and second-highest p_{T} muons in a MC sample of $gg \to ZZ$. The blue line shows the invariant mass of the muons before any of the selection criteria have been applied, and the red line shows the invariant mass of the muons in the sample after all selections are applied.

to $\nu\bar{\nu}$ yielding $E_{\mathrm{T}}^{\mathrm{miss}}$, the other Z boson's momentum should be equal to (but in the opposite direction of) the $E_{\mathrm{T}}^{\mathrm{miss}}$ in the event. This can be seen in Figure 6.8, where the distributions are plotted on the same graph in order to compare their shapes. The agreement is much better after the objects are selected as the object selection cuts eliminate muons in the event that may originate from the decay of a jet, not from the decay of a Z boson.

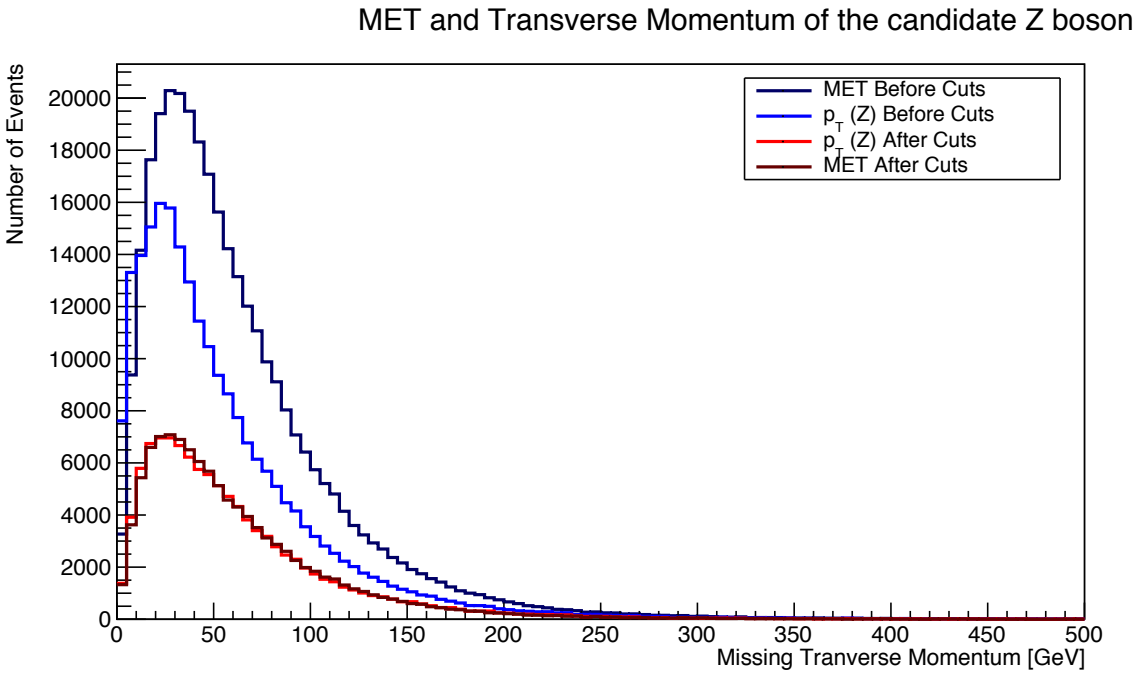

Figure 6.8: Comparison of the $\mu\mu$ p_{T} ($Z \to \mu^+\mu^-$) and the missing transverse momentum in a MC sample of $gg \to ZZ$, after all of the object selection cuts have been performed, and keeping events with two selected muons. The red (p_{T} ($Z \to \mu^+\mu^-$)) and dark red ($E_{\mathrm{T}}^{\mathrm{miss}}$) distributions show very good agreement after keeping events with two selected muons .

6.1.3 Jets

Candidate jets (see [78] for a complete ATLAS definition of jet objects) are required to be reconstructed with the anti-k_t [96] clustering algorithm, using three dimensional topological clusters to build jets, with the size parameter of 0.4. The energy of the jet is calibrated to the hadronic scale, and pileup effects are removed. Jets are required to have a $p_{\mathrm{T}} > 20$ GeV (`PT20`), and $|\eta| < 4.5$ (`ETA45`). Pileup suppression is achieved with a sophisticated algorithm requiring a percentage of the tracks in a

jet to be associated with the primary vertex (JVTX) [97]. Jets having overlapping tracks with electrons ($\Delta R < 0.2$) are removed (OR). After this any remaining jets with technical reconstruction problems are rejected by requiring the jets to fulfill the 'bad-loose' quality criteria (CLEAN). Depending on what variable the jets are being used to define, there may also be a p_{T} cut of 25 GeV (PT25). A summary of these selections are seen in Table 6.3. The object cutflow for jets remaining after each of these criteria can be seen in Figure 6.9.

Identification	AntiKt4EMTopo Jets
Kinematic cuts	$p_{\mathrm{T}} > 20$ GeV $\lvert\eta\rvert < 4.5$
Pileup Removal	JVT < 0.59 for $p_{\mathrm{T}} > 60$ GeV, $\lvert\eta\rvert < 2.4$ Jets
Quality	Bad-Loose Jets accepted
b-jet tagging	MV2c10 > 0.1758

Table 6.3: Summary of jet selections.

b-jets

Jets can be further classified depending on whether they originated from a heavy flavour quark. The heavy flavour quarks are often produced in events that contain t-quarks, as the t-quark decay includes a b-quark, and are important to identify in order to reject events originating from a background process.

Operating points are defined by a single cut value on the discriminant output distribution and are chosen to provide a specific b-jet efficiency on an inclusive $t\bar{t}$ sample. The 85% working point was used for tagging b-jets for this analysis [98].

Correction factors are applied to the simulated event samples to compensate for differences between data and simulation in the b-tagging efficiency for b, c and light-jets. The correction for b-jets is derived from $t\bar{t}$ events with final states containing two leptons, and the corrections are consistent with unity with uncertainties at the level of a few percent over most of the jet p_{T} range [99].

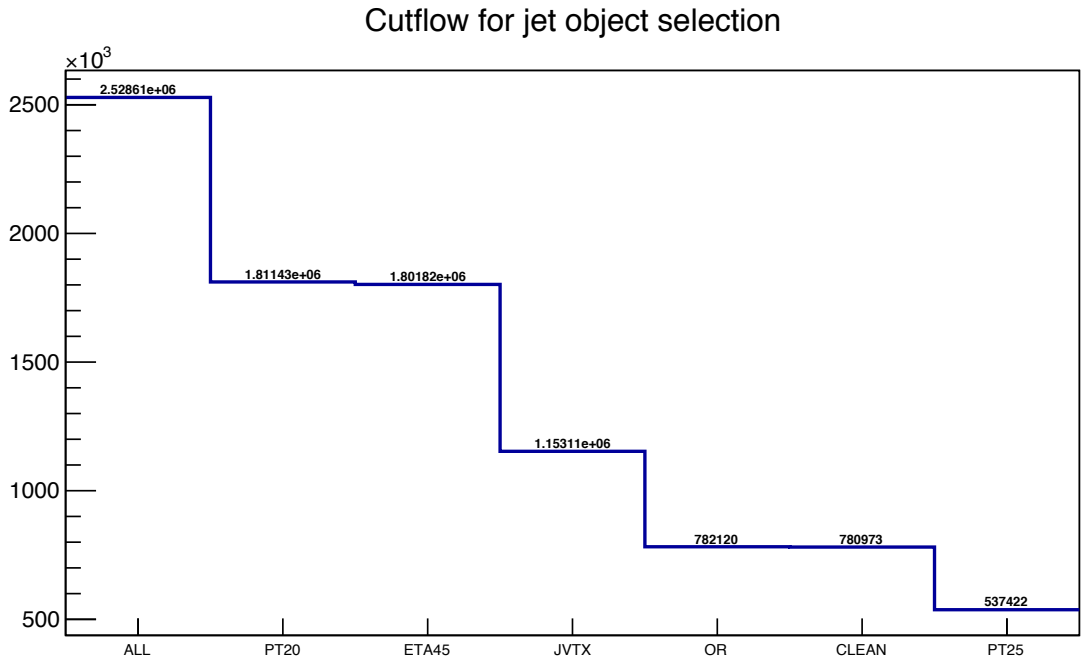

Figure 6.9: The number of jets passing the object selection cuts in a MC sample of $gg \to ZZ$ (sample identification 343233 from Table 5.1), where one Z decays to charged leptons, and the other Z to neutrinos: $ZZ \to \ell^+\ell^-\bar{\nu}\nu$.

6.1.4 Overlap Removal

Overlap removal is performed on the reconstructed objects to guard against double counting any object. The ATLAS strategy for overlap removal is outlined in [100]. Overlap occurs when a single physical object in the detector has been reconstructed as two or more objects (as identified by the object selection criteria) or if two physically nearby objects have been reconstructed as a single object. In order to define whether two objects are likely the same, the ATLAS strategy recommends to use an angular distance measurement (defined with rapidity y) defined as $\sqrt{(\Delta\phi)^2 + (\Delta y)^2}$. After overlap removal, the selected electrons, muons, and jets will refer to unique objects.

6.1.5 Missing Transverse Energy

Finally, missing energy is identified by taking the negative direction of the vector sum of the momenta of the calibrated objects in the event. Tracks and energy clusters that have not been used in a jet, electron, or muon object are called soft terms. There are two ways to add them into the missing transverse energy calculation. Either they are added using the track-based terms, or by adding the cluster-based soft terms. For a higher pileup environment, the track-based method is more robust, as it is based on primary vertex tracks [101].

$$\mathbf{p}_{\mathrm{T}}^{\mathrm{miss}} = -\left(\Sigma\mathbf{p}_{\mathrm{T}}^{\mathbf{jets}} + \Sigma\mathbf{p}_{\mathrm{T}}^{\mathbf{el}} + \Sigma\mathbf{p}_{\mathrm{T}}^{\mathbf{mu}} + \Sigma\mathbf{p}_{\mathrm{T}}^{\mathbf{Soft\,track}}\right) \tag{6.3}$$

During the calculation of missing energy from calibrated objects, an internal overlap removal is performed. Of particular importance to this analysis was to ensure that any double-counting between jets and high p_{T} muons was avoided. This double-counting can occur when jets due to pileup are close to high-energy muons.

The magnitude of the missing momentum vector is the distinguishing variable in this analysis:

$$E_{\mathrm{T}}^{\mathrm{miss}} \equiv \left|\mathbf{p}_{\mathrm{T}}^{\mathrm{miss}}\right|. \tag{6.4}$$

This quantity, $E_{\mathrm{T}}^{\mathrm{miss}}$, is referred to as missing energy and sometimes abbreviated as MET.

6.2 Pre-selection

Some events in the detector are not worth considering. Such events may be contaminated with extraneous energy, bad reconstruction, or non-physical events. This could be due to many different factors. The cases where events should be removed before optimizing the event selections that are considered in this analysis are discussed below. This is known as pre-selection of the events, and ensures a higher quality of events go into the analysis. However, care is taken to avoid cutting out any possible signal that may look like a bad event.

Vertex The presence of a hard-scattering vertex with at least two associated tracks is required. The hard-scattering vertex is known as the primary vertex of the event, and is reconstructed by associating the vertex with the highest $\Sigma\, p_{\mathrm{T}}^2$ of objects in the event [102]. Further details of reconstruction and performance can be found in public notes [103].

Fake Jets When jets of particles originate from sources other than a hard collision in the detector, this leads to an event that is either uninteresting to the analysis, or an event that has been contaminated. In either case, the event should be rejected from consideration in the analysis. These events could come from either non-collision backgrounds, such as beam loss protons or cosmic ray showers, or they could come from a large amount of noise in the calorimeter. Removing events with this contamination is accomplished using a software package called JetSelector [104], with its associated cleaning tool properties `CutLevel = LooseBad` and `DoUgly = False`.

Trigger When an event has been recorded, it is because the event has passed both the hardware level trigger and the higher level, software-based trigger. In order to make sure that the right events are being analyzed, it is required that a trigger relevant to the analysis has fired. In this analysis, the triggers of interest are single-lepton muon and electron triggers. If the objects have passed a different trigger, it is likely that the event will not be relevant for the analysis. Trigger information is included in the MC simulation. The trigger menu used for the 2015+2016 dataset is reported in Table 6.4. As the triggers are not prescaled, they all correspond to the same integrated luminosity.

Period	Trigger selection
	Single Muon
2015	mu20_iloose_L1MU15 OR mu50
Early 2016	mu24_ivarmedium OR mu50
Late 2016	mu26_ivarmedium OR mu50
	Single Electron
2015	e24_lhmedium_L1EM18VH OR e60_lhmedium OR e120_lhloose
Early 2016	e24_lhtight_nod0_ivarloose OR e60_lhmedium_nod0 OR e140_lhloose_nod0
Late 2016	e26_lhtight_nod0_ivarloose OR e60_lhmedium_nod0 OR e140_lhloose_nod0

Table 6.4: Trigger requirements in 2015 and 2016 data periods. The single lepton triggers were all unprescaled in the 2015 and 2016 data-taking period. Late 2016 indicates the period after the luminosity increased to $> 10^{34}\text{cm}^{-2}\text{s}^{-1}$. For single muon triggers, isolation of low p_{T} muons was required. In 2015 data runs e24_lhmedium_L1EM18VH was not available and so was replaced by e24_lhmedium_L1EM20VH. For a single run (298687) the trigger e24_lhmedium_nod0_L1EM20VH was used, because L1_EM20VHI was partially prescaled. See Section 4.2.5 for an explanation of the trigger naming conventions in ATLAS.

Trigger Matching The next step in triggering is to make sure one of the analysis physics objects is the one that fired the trigger. This ensures that a trigger efficiency value can be calculated for the event, which is an important scale factor for the analysis. This is done for both data and MC simulation. The software tool used to check which object is associated with the trigger that was fired is the TriggerMatchingTool. It uses an angular distance ΔR to match the trigger object to a reconstructed object.

Good Runs List Data quality is scrutinized for every 'lumiblock', where a lumiblock is defined as a short period of time in a run where the conditions are assumed stable (nominally 60 seconds). Any poor quality data are flagged, and only data that are of the highest quality are put on the Good Runs List (GRL). Any portion of the reconstructed data that is not on the GRL is disregarded for the analysis. A GRL is associated with a luminosity. This luminosity can be found by querying a database to find what fraction of the time the trigger/triggers were active for during data collection.

Error Flags In case any error flags were considered too specific for the GRL, additional checks may be done on each relevant part of the detector to look for an error state on an event by event basis in the data. For this analysis, the following checks were done to ensure no error states occurred which may or may not have been covered by the GRL:

- Events affected by the recovery procedure for 'single event upsets' [105] in the Semiconductor Tracker (SCT) component of the Inner Detector.
- Calorimeter quality flags are required to have no error codes.
- Incomplete events are vetoed by checking event error codes.

6.3 Event Selection

Reconstructed selected objects from an event are used to determine whether it is a candidate Mono-Z dark matter event. These events with selected objects are then required to pass pre-selection. Subsequently, they will be used to determine an optimal set of event selection criteria, referred to as 'cuts'. These cuts were tested and optimized in order to maximize sensitivity to the various Mono-Z signals, and minimize the Standard Model backgrounds. (The major backgrounds have been listed in Section 5.2.1.)

Candidate events are required to have a charged lepton pair of opposite sign, either e^+e^- or $\mu^+\mu^-$, that pass the object selection criteria. Events with a third charged lepton are rejected, as these are events that likely come from diboson events such as WZ or ZZ. Events are required to have missing transverse energy > 90 GeV, and be in the Z mass window of $76 < m_{\ell^+\ell^-} < 106$. The $E_{\mathrm{T}}^{\mathrm{miss}}$ cut removes most of the Z+jets background but is low enough not to remove most of the signal. The Z mass window cut selects events with a Z boson in them. Together these two cuts remove much of the background and select a region with potential signal. Further kinematic criteria include an angular cut between the leptons $\Delta R_{\ell^+\ell^-} < 1.8$, and an angular cut between the Z and the missing transverse energy of $\Delta\phi(Z, E_{\mathrm{T}}^{\mathrm{miss}}) > 2.7$. These kinematic cuts select Z bosons that are boosted in the transverse direction, opposite to the missing energy. Events with a fractional p_{T} difference

$$\frac{||\mathbf{p}_{\mathrm{T}}^{\mathrm{miss}} + \Sigma\mathbf{p}_{\mathrm{T}}(\mathrm{jet})| - p_{\mathrm{T}}(\ell^+\ell^-)|}{p_{\mathrm{T}}(\ell^+\ell^-)} > 0.2 \tag{6.5}$$

tend to be badly measured and are removed. Another selection that removes events with mismeasured jets is the minimum angular cut of $\Delta\phi(\mathrm{jet}, E_{\mathrm{T}}^{\mathrm{miss}})_{\mathrm{min}}$, removing primarily Z+jets events. Finally, a $p_{\mathrm{T}}(Z)/m_{\mathrm{T}}$ cut is applied to ensure the quality of Z+jets events in the background control region. Here, m_{T} is defined as $\sqrt{2p_{\mathrm{T}}(Z)E_{\mathrm{T}}^{\mathrm{miss}}(1 - \cos(\Delta\phi(Z, E_{\mathrm{T}}^{\mathrm{miss}})))}$. Additionally, events with b-jets passing the object selection criteria are discarded, as a b-jet in the event often originates from t-quark decays occurring primarily in the backgrounds. These selection criteria are summarized in Table 6.5.

Signal Regions Definition	
Trigger	Lowest unprescaled single lepton
Lepton	Same flavour, opposite sign (e^+e^-, $\mu^+\mu^-$) $p_{\mathrm{T}} > 20(30)$ GeV leading(subleading)
3rd Lepton	Vetoed with Loose ID and p_{T} >7 GeV
Z mass window	76 GeV $< m(\ell^+\ell^-) <$ 106 GeV
$E_{\mathrm{T}}^{\mathrm{miss}}$	$>$ 90 GeV
$\Delta R(\ell, \ell)$	$<$ 1.8 rad
$\Delta\phi(Z, E_{\mathrm{T}}^{\mathrm{miss}})$	$>$ 2.7 rad
$\lvert\lvert\mathbf{p}_{\mathrm{T}}^{\mathrm{miss}} + \Sigma\mathbf{p}_{\mathrm{T}}(\mathrm{jet})\rvert - p_{\mathrm{T}}(Z)\rvert / p_{\mathrm{T}}(Z)$	$<$ 0.2%
$\Delta\phi(\mathrm{jet}, E_{\mathrm{T}}^{\mathrm{miss}})_{\mathrm{min}}$	$>$ 0.6 rad for jets $>$ 25 GeV
$p_{\mathrm{T}}(Z)/m_{\mathrm{T}}$	$<$ 0.9
b-jet veto	for b-jets $>$ 20 GeV, $\lvert\eta\rvert < 2.5$, tagged at 85%

Table 6.5: Summary of event selections for the ee and $\mu\mu$ signal regions.

6.4 Significance and Optimization

A measure of how well a signal sample can be distinguished from the background is the significance. The significance of the signal, denoted here by S, is proportional to how many signal events, s, pass the selection, divided by the square root of the number of background events, $\sqrt{b}$. Here b is the number of MC based background events. This is an approximation that is only valid for $s \ll b$.

$$S \propto \frac{s}{\sqrt{b}} \tag{6.6}$$

The full equation for significance, Equation 6.7, is necessary when the signal and background values are comparably sized. This has been used for optimization, rather than the approximation above [106].

$$S = \sqrt{2\big((s+b)\ln\left(1+\frac{s}{b}\right) - s\big)} \tag{6.7}$$

Using this on the yields from MC generated backgrounds and signal, the significance of a signal sample can be estimated. Without making any selection beyond requiring good physics objects and the pre-selection, the significance will be very low.

Simple selection criteria can be applied on the signal and background sets, removing events unlikely to be signal events. The selections introduced in the previous section were chosen to optimize the significance. Some of the selections are simple, such as requiring a particular number of a type of particle in the detector, and cannot be optimized further. Others have a choice of threshold, such as the minimum amount of missing energy ($E_{\mathrm{T}}^{\mathrm{miss}}$) required in the detector. The selection quantity can be scanned across a range of physically meaningful options to discover the most optimal value. This can be seen in Figure 6.10, where the most significant value for the $E_{\mathrm{T}}^{\mathrm{miss}}$ selection is labelled, and Figure 6.11, where the most significant value for the $\Delta\phi(Z, E_{\mathrm{T}}^{\mathrm{miss}})$ selection is labelled.

Beyond significance, the efficiency and the rejection were used to discriminate the best selection value. The efficiency at a selection cut value, ϵ_{cut}, is calculated as the signal at that cut value (s_{cut}) divided by the total signal (s_{tot}). The rejection, r_{cut}, is defined as the background at that cut value (b_{cut}) subtracted from the total background (b_{tot}), all divided by the total background. Both these terms are normalized to vary between 0 and 1, and are summarized in Equations 6.8 and 6.9.

$$\epsilon_{\text{cut}} = \frac{s_{\text{cut}}}{s_{\text{tot}}} \tag{6.8}$$

$$r_{\text{cut}} = \frac{b_{\text{tot}} - b_{\text{cut}}}{b_{\text{tot}}} \tag{6.9}$$

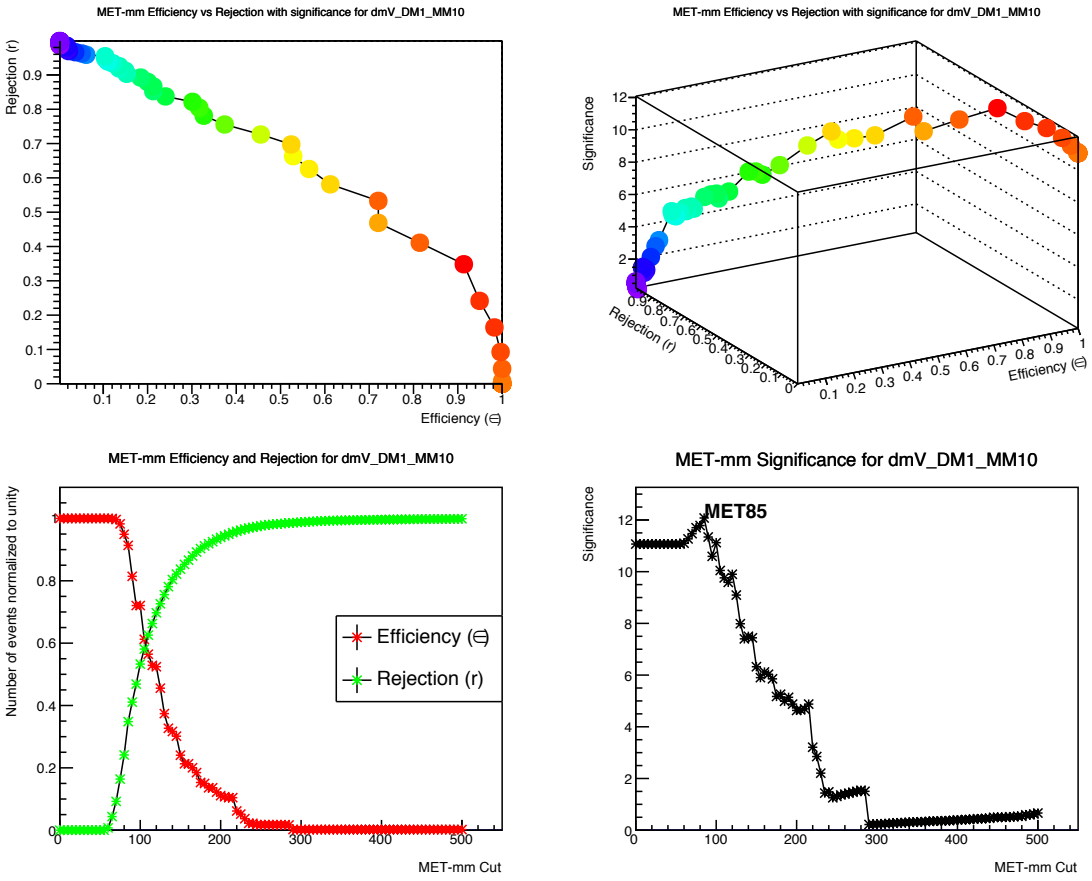

Figure 6.10: Optimization example of the missing energy. The significance as a function of the cut value can be seen in the lower right plot. The lower left plot shows the efficiency and rejection curves as a function of cut values. The top left plot shows the efficiency as a function of rejection, where the colour indicates the value of the significance at each point, that corresponds to the values in the top right plot. Finally, the top right plot shows the same as the top left, but as a three-dimensional plot with the significance on the third axis (with coloured values).

The overall optimization was done using the following procedure. Nominal values were chosen for each selection using values from previous analyses. Then one selection at a time was stepped through the physical values it could take on, while all other

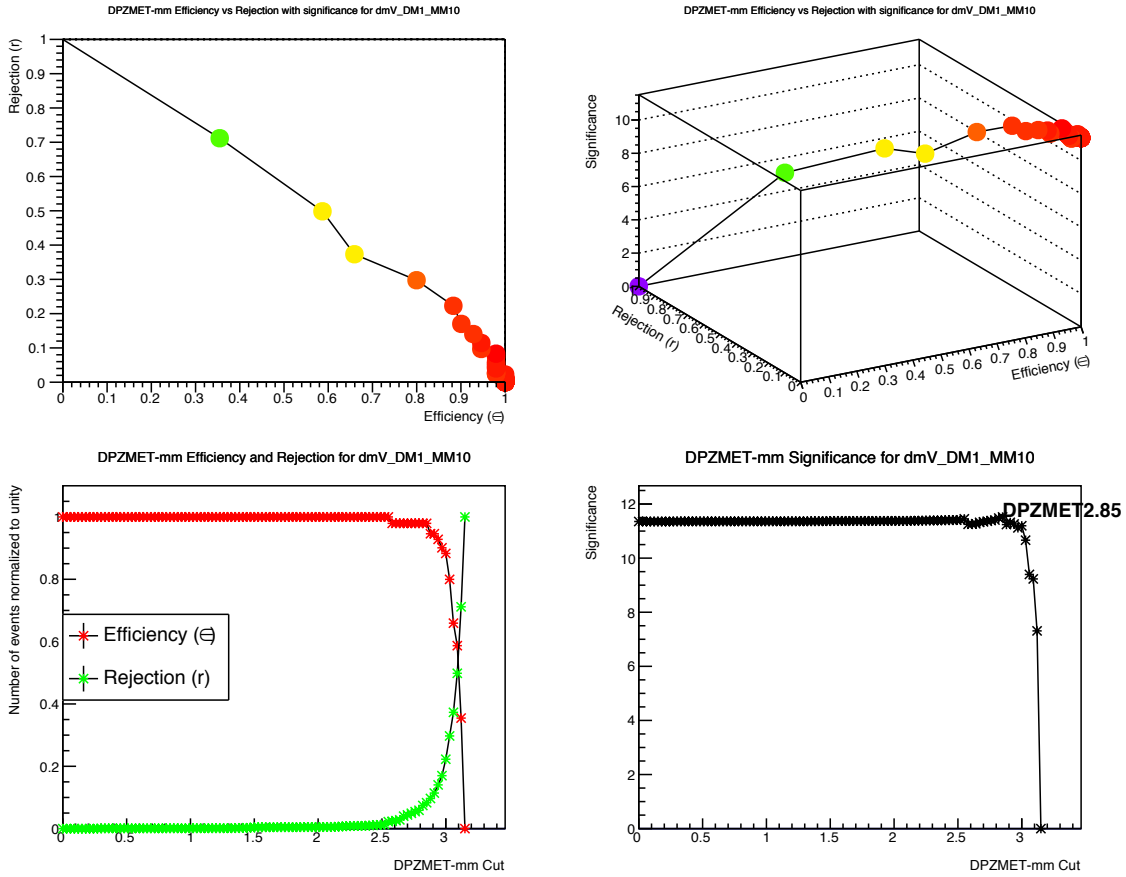

Figure 6.11: Optimization example of the angular distribution between the Z p_{T} and the $E_{\mathrm{T}}^{\mathrm{miss}}$ ($\Delta\phi(Z, E_{\mathrm{T}}^{\mathrm{miss}})$). The significance as a function of the cut value can be seen in the lower right plot. The lower left plot shows the efficiency and rejection curves as a function of cut values. The top left plot shows the efficiency as a function of rejection, where the colour indicates the value of the significance at each point, that corresponds to the values in the top right plot. Finally, the top right plot shows the same as the top left, but as a three-dimensional plot with the significance on the third axis (with coloured values).

selections were held at their nominal values. At each of these selection values, a significance was calculated for the signal sample.

As there were multiple signal samples that were being considered, this procedure was repeated for each sample. The point of highest significance depends on the properties of the signal sample, as the different samples have different mediator particle and dark matter masses and therefore different kinematic distributions. Each of the values of highest significance are added to a histogram in order to see if there were any values that applied for all samples. See Figures 6.12 and 6.13.

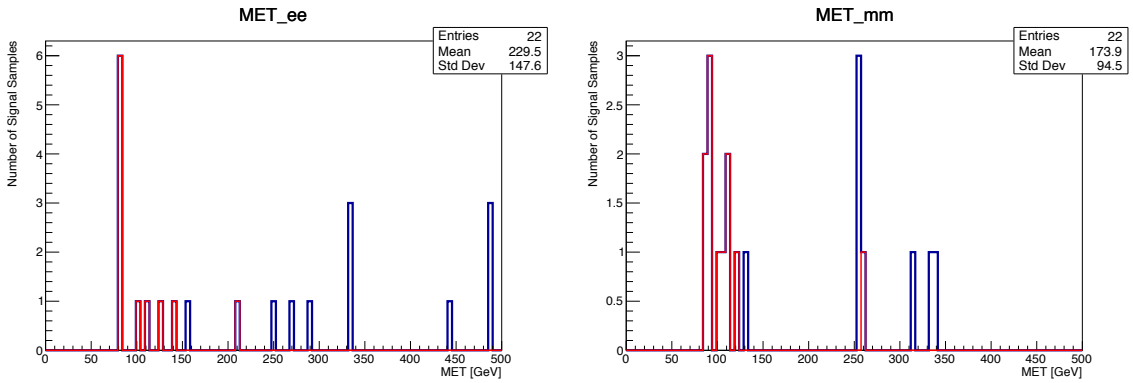

Figure 6.12: The most significant values of $E_{\mathrm{T}}^{\mathrm{miss}}$ for a subset of vector samples in blue, with the ten most significant samples highlighted in red, for both ee (left) and $\mu\mu$ (right).

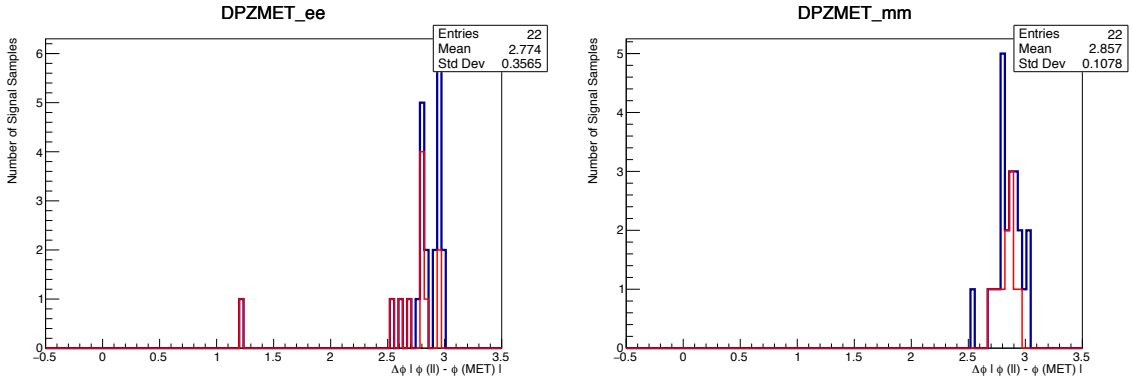

Figure 6.13: The most significant values of $\Delta\phi(Z, E_{\mathrm{T}}^{\mathrm{miss}})$ for a subset of vector samples in blue, with the ten most significant samples highlighted in red, for both ee (left) and $\mu\mu$ (right).

Due to the clustering of the significant samples at the same value, it was possible to choose the same cuts for all DM vector model samples. The angular cuts were similar, and a lower $E_{\mathrm{T}}^{\mathrm{miss}}$ cut, while not optimal for higher masses, was inclusive of both the low and high mass samples.

Chapter 7

Background Estimation

All of the MC modelling of backgrounds in this analysis have been laid out in Section 5.2.1. However, as was mentioned, some of the backgrounds are poorly modelled in the MC. Since there are enough statistics in the data, many of these backgrounds can be estimated using data-driven techniques. This could involve estimating either the yields or the distribution shapes, or both, using data. The methods to obtain the data-driven backgrounds are validated with the MC, but can be applied to the data. This analysis uses $E_{\mathrm{T}}^{\mathrm{miss}}$ as the discriminating variable in six bins with bin edges in GeV given by: $[90, 100, 120, 140, 200, 300, 1000]$.

ZZ Background The irreducible ZZ background is estimated through MC simulated samples for both shape and yield.

WZ Background The WZ background shape is estimated with MC simulation. The WZ yield is estimated through data methods.

WW, $t\bar{t}$, Wt, $Z \to \tau\tau$ Backgrounds These non-resonant dilepton backgrounds have their shape estimated through MC simulation, and their yields estimated through data.

Z+jets Background This background has its shape estimated through Madgraph MC simulation, and yield estimated through data.

W+jets, ttV, $ttVV$, and VVV Backgrounds These smaller backgrounds are estimated entirely through MC simulation.

Each of these will be described in detail in the following text.

7.1 ZZ Background

The SM process $ZZ \to \ell^+\ell^-\bar{\nu}\nu$ has the same final state as the DM signal models, and is therefore the main background to this search.

Because the kinematics of this diboson background are similar to the kinematics of the signal, it is difficult to define a control region to estimate the ZZ background from data. Previous ATLAS analyses have used MC predictions for this background process, as uncertainties from estimating the SM ZZ process in data were larger than uncertainties arising from theoretical predictions by MC [107].

The ZZ background consists of contributions from two production modes: the dominant quark-antiquark production ($q\bar{q} \to ZZ$), and gluon-gluon production ($gg \to ZZ$). The MC samples used to simulate ZZ production for both processes are the POWHEG samples presented in Chapter 5. Higher order corrections, NLO/LO, to the $gg \to ZZ$ continuum are accounted for in a k-factor calculated for massless quark loops, for heavy top and for $gg(\to h^*) \to ZZ$. This k-factor is calculated to be compatible with a flat value of 1.7 ± 1.0. These corrections are obtained from theoretical calculations [108] from groups studying similar higgs processes.

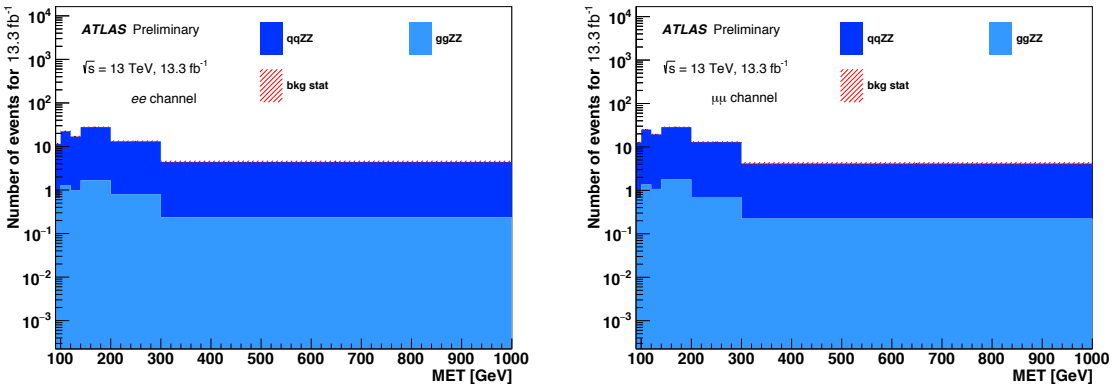

Figure 7.1: ZZ background estimated with MC in the (left) ee and (right) $\mu\mu$ channels. The error band includes the statistical error on the samples. This is after the Z mass requirement selection is applied in the sequential cutflow from Table 6.5.

The ZZ yields from the MC samples with the k-factor applied and uncertainties[1] are shown in Table 7.1. The shapes of this background in $E_{\mathrm{T}}^{\mathrm{miss}}$ are shown in Fig-

[1]Unless otherwise stated, all results will be quoted in number of events as: **yield** $\pm$ **stat** $\pm$ **syst**. If only one error is quoted, it will refer to **yield** $\pm$ **stat**.

ure 7.1. Theoretical uncertainties are considered for the shape and yield, and are computed as a function of m_{ZZ}, as they were calculated by groups studying heavy higgs decays to ZZ. The sources of theoretical uncertainties include the variation of the QCD scale and variation of the PDF. The systematic uncertainties will be discussed in Chapter 8.

	$q\bar{q} \to ZZ$ estimate
SR ee	**90.4 ± 1.4 ± 5.8**
SR $\mu\mu$	**97.2 ± 1.5 ± 8.0**
	$gg \to ZZ$ estimate with k-factor applied
SR ee	**5.6 ± 0.1 ± 3.4**
SR $\mu\mu$	**5.8 ± 0.1 ± 3.5**

Table 7.1: Summary of the ZZ background events in the signal region (SR) estimated using MC with higher order k-factors applied, and showing both statistical and systematic uncertainties.

7.2 WZ Background

The WZ background shape is evaluated with MC simulated samples using Powheg interfaced with Pythia, as discussed in Section 5.2.1.

The WZ background yield can be estimated using a three lepton control region (3ℓCR) in data. This requires redefining the event selection to let events with a third lepton pass the selection, and seeing how many events pass this new selection criteria. This redefined cutflow is in Table 7.2, described in detail below. As will be shown, the events passing these selection criteria will almost exclusively come from a diboson event consisting of a W and a Z.

$WZ \to \ell\nu\ell^+\ell^-$ events, in which the lepton from the W decay is not reconstructed, or does not fall within acceptance, is the second largest background for this analysis in the $E_{\mathrm{T}}^{\mathrm{miss}}$ region. To correct the normalization of $WZ \to \ell\nu\ell^+\ell^-$ prediction with data, the three lepton control region is defined to have one additional lepton in addition to the two leptons from Z boson decay. The third lepton is defined in the same way as

3ℓCR definition	
Trigger	Lowest unprescaled single lepton
Lepton	Same flavour, opposite sign (e^+e^-, $\mu^+\mu^-$) $p_{\mathrm{T}} > 20(30)$ GeV leading(subleading)
3rd Lepton	Required with Medium ID and $p_{\mathrm{T}} > 20$ GeV
Z mass window	76 GeV $< m(\ell^+\ell^-) <$ 106 GeV
$m_{\mathrm{T}}(W)$	> 60 GeV
b-jet veto	for b-jets > 20 GeV, $\lvert\eta\rvert < 2.5$, tagged at 85%

Table 7.2: Summary of event selections applied to define the 3ℓ Control Region for the WZ background estimation.

are the two leptons from the Z (Tables 6.1 and 6.2). This third lepton (ℓ_3) and the $E_{\mathrm{T}}^{\mathrm{miss}}$ are used to define the transverse mass of the W boson, $m_{\mathrm{T}}(W)$, as in Equation 7.1:

$$m_{\mathrm{T}}(W) \equiv \sqrt{2p_{\mathrm{T}}^{\ell_3} E_{\mathrm{T}}^{\mathrm{miss}}(1 - \cos(\Delta\phi(E_{\mathrm{T}}^{\mathrm{miss}}, \ell_3))}. \tag{7.1}$$

Figures 7.2 and 7.3 show p_{T}, η and ϕ distributions for the third lepton in the 3ℓCR. Four separate channels are defined by adding either an electron or muon to one of the two signal regions. In the case where all three leptons are the same flavour ($ee + e$ or $\mu\mu + \mu$), the ℓ_3 is identified by finding the highest p_{T}, opposite sign pair of leptons that are closest to the Z mass and assigning them as coming from the Z boson. The remaining lepton is assigned as coming from the W boson. The $m_{\mathrm{T}}(W)$ from the ℓ_3 is required to have a minimum value of 60 GeV in order to ensure the channels have predominantly events from WZ dibosons. These selection requirements are summarized in Table 7.2.

Theoretical uncertainties are only considered for shape and computed as a function of m_{WZ}. The sources of theoretical uncertainties include the variation of QCD scale and variation of the PDF, and have been obtained similarly to the ZZ theoretical corrections [108]. Systematic uncertainties of the WZ background are estimated from the selection dependencies of the scale factor for the inclusive category.

7.2.1 Calculating the Scale Factor for WZ Events

The 3ℓCR is used to obtain a scale factor for the correction between observed events and the WZ expectation from MC. The scale factor is applied to normalize the WZ expectation in the signal regions. In events with a transverse mass between the additional lepton and the $E_{\mathrm{T}}^{\mathrm{miss}}$ greater than 60 GeV, and a b-jet veto, WZ events dominate. The m_{T} (W) selection removes the Z+jets contribution from the 3ℓCR, and the events remaining in the control region turn out to be $\sim 90\%$ WZ events. In Table 7.3 the number of backgrounds and data events in the 3ℓCR is given for each decay mode of the Z and W bosons, together with the corresponding scale factors obtained.

The WZ contribution in the signal region is calculated as

$$N_{WZ}^{\mathrm{SR}} = N_{WZ,\,\mathrm{MC}}^{\mathrm{SR}} \times f_{WZ} = N_{WZ,\,\mathrm{MC}}^{\mathrm{SR}} \times \frac{N_{\mathrm{data}}^{\ell_3} - N_{\text{non-}WZ,\,\mathrm{MC}}^{\ell_3}}{N_{WZ,\,\mathrm{MC}}^{\ell_3}}, \tag{7.2}$$

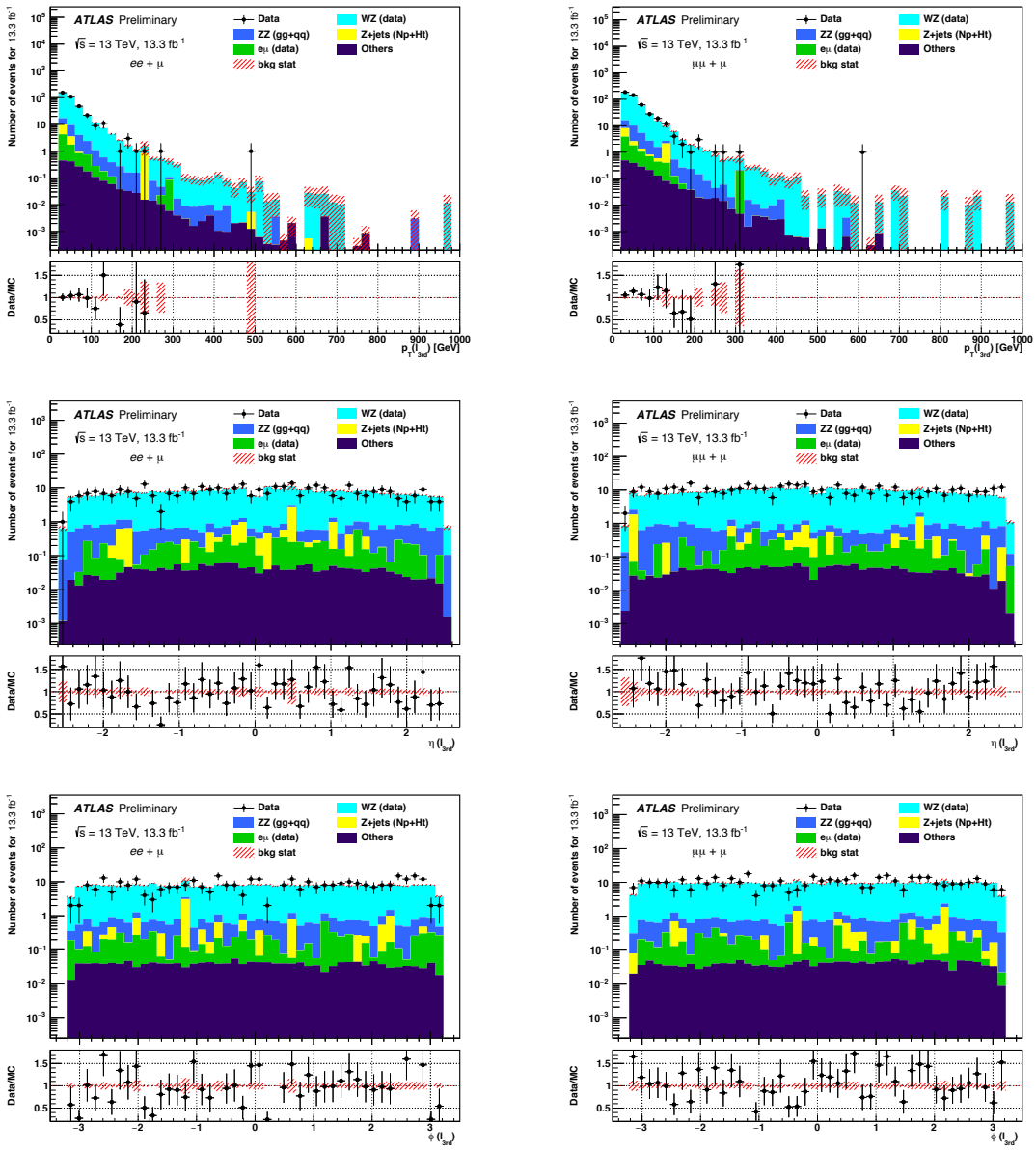

Figure 7.2: The p_{T} (top two), η (middle two) and ϕ (bottom two) distributions of the additional muon in events with a third lepton. The left column contains events with $ee + \mu$ and the right column contains events with $\mu\mu + \mu$. MC samples are normalized to their cross section values as given in Chapter 5 and re-scaled to the data integrated luminosity reported in the figure. The error band in the ratio plot includes the MC statistical uncertainty.

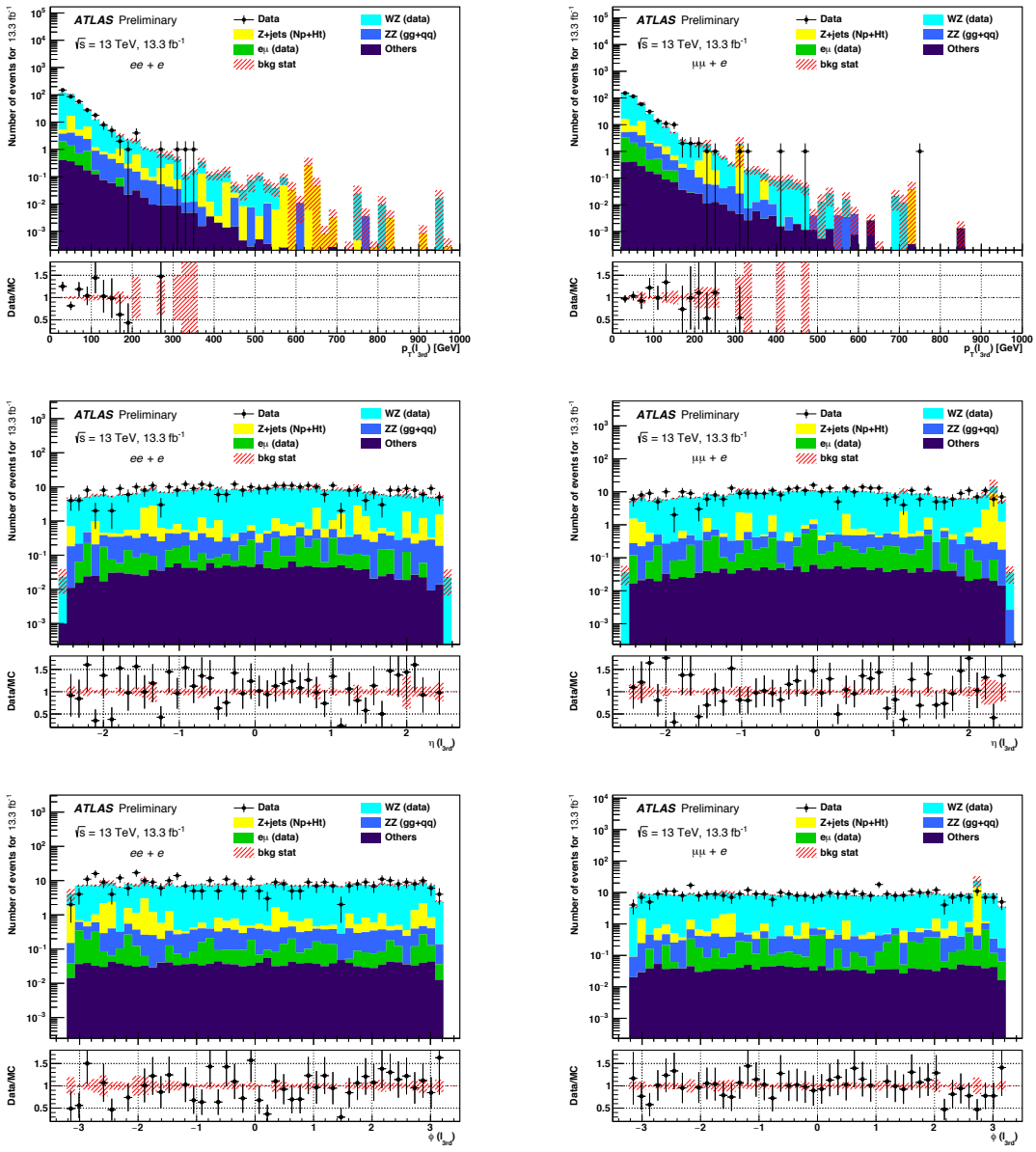

Figure 7.3: The p_{T} (top two), η (middle two) and ϕ (bottom two) distributions of the additional electron in events with a third lepton. The left column contains events with $ee + e$ and the right column contains events with $\mu\mu + e$. MC samples are normalized to their cross section values as given in Chapter 5 and re-scaled to the data integrated luminosity reported in the figure. The error band in the ratio plot includes the MC statistical uncertainty.

where $N^{\mathrm{SR}}_{WZ,\,\mathrm{MC}}$ is the MC prediction of the WZ yield in the signal region, $N^{\ell_3}_{\mathrm{data}} - N^{\ell_3}_{\text{non-}WZ,\,\mathrm{MC}}$ is the observed data yield subtracting the non-WZ contribution estimated from MC in the ℓ_3 control region, and $N^{\ell_3}_{WZ,\,\mathrm{MC}}$ is the MC expectation in the ℓ_3 control region for the WZ background.

The normalization factor to the MC expectation, f_{WZ}, is evaluated for all four possible final states, eee, $ee\mu$, $\mu\mu e$, and $\mu\mu\mu$. The four f_{WZ} values are then averaged using weights that correspond to the expected WZ contribution from data in each of the final states. These values are shown in Table 7.3. The weighted average f_{WZ} is used in the estimation of the WZ background in all final states. The maximal difference between the average f_{WZ} and the various values in each final state is taken as a systematic uncertainty on the yield. This procedure yields $f_{WZ} = \mathbf{1.26 \pm 0.05(stat) \pm 0.05(syst)}$. After applying this scale factor, the four final states are consistent with the data, as seen in Figure 7.4.

The $E_{\mathrm{T}}^{\mathrm{miss}}$ shape in the signal region (SR) is then taken from MC and normalized to the data yield through f_{WZ} as explained above. Systematic uncertainties on the $E_{\mathrm{T}}^{\mathrm{miss}}$ shape from the MC are computed as a function of m_{WZ} from the variation of QCD scale and variation of PDF. The results are summarized in Table 7.4.

channel	WZ expected	non-WZ background	observed	scale factor (f_{WZ})
$ee + e$	248.5 ± 1.9	40.0 ± 4.4	363	1.30 ± 0.16
$ee + \mu$	267.6 ± 2.0	35.9 ± 3.0	361	1.22 ± 0.12
$\mu\mu + e$	290.1 ± 2.1	48.7 ± 10	406	1.23 ± 0.26
$\mu\mu + \mu$	327.2 ± 2.3	39.2 ± 2.6	466	1.30 ± 0.10
Total	1133 ± 4	163.9 ± 11.7	1596	**1.26 ± 0.05 ± 0.05**

Table 7.3: The expected number of background and observed number of events in the 3ℓCR in the $m_{\mathrm{T}}(W) > 60$ GeV and b-jet veto region. The final column shows the scale factor. It is obtained by subtracting other backgrounds (found from MC) from the observed yields in data, and taking the ratio between this and the expected number of events from the WZ MC. Number of observed events is for an integrated luminosity of 13.3 fb^{-1}. The largest variation among different channels is the systematic quoted on the total result.

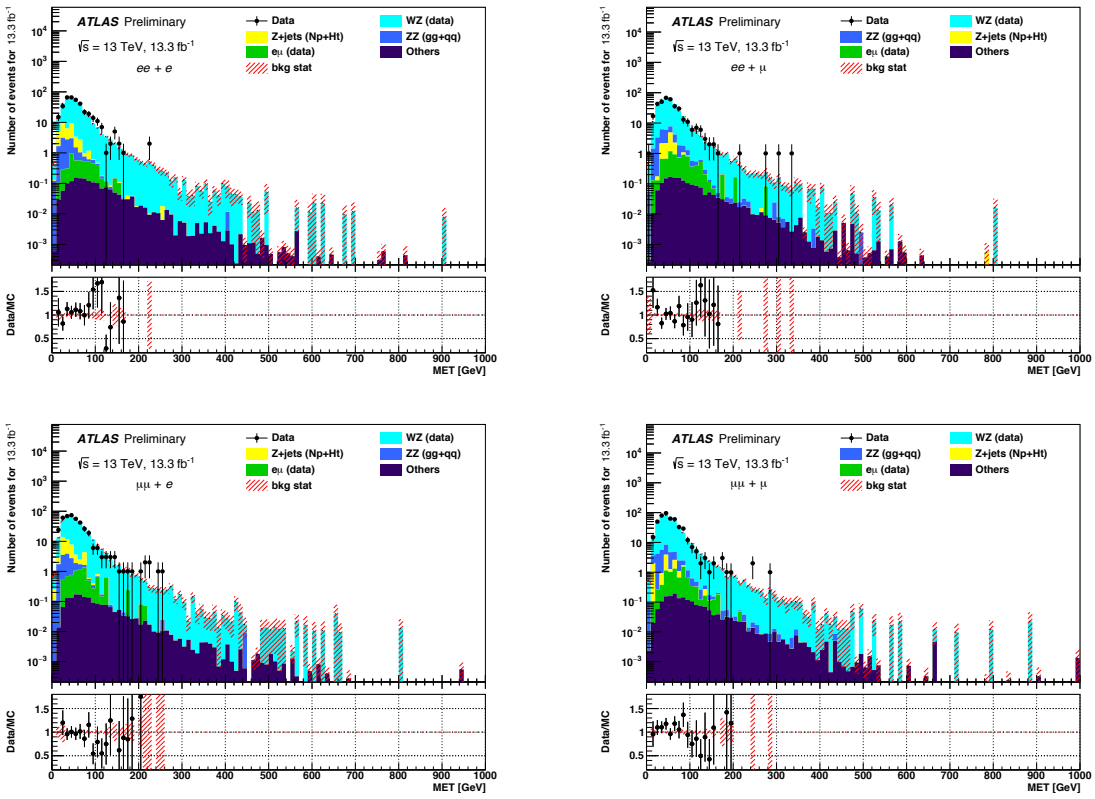

Figure 7.4: $E_{\mathrm{T}}^{\mathrm{miss}}$ distributions after the m_{T} (W) cut for data and MC in (a) the $ee + e$ channel, (b) $ee + \mu$ channel, (c) $\mu\mu + e$ channel and (d) $\mu\mu + \mu$ channel in events with one additional electron or muon with respect to the lepton pair whose invariant mass is consistent with the Z boson mass. MC samples are normalized to their cross section values as given in Chapter 5 and re-scaled to the data integrated luminosity reported in the figure. The bottom plots show the ratio of the data and MC.

	WZ event estimates with scale factor applied	MC expected events
SR ee	**44.9 ± 1.1 ± 2.2**	(35.6 ± 0.9)
SR $\mu\mu$	**51.4 ± 1.2 ± 2.6**	(40.8 ± 1.0)

Table 7.4: Summary of the WZ background events estimated using the scale factor derived from data to normalize the MC yield. The statistical and systematic uncertainties are as described in the text.

7.3 WW, $t\bar{t}$, Wt, and $Z \to \tau\tau$ Backgrounds

The set of processes: WW, $t\bar{t}$, Wt and $Z \to \tau\tau$, are grouped together because each can be estimated by exploiting flavour symmetry in their decay modes. Each has a small impact on the total background of the analysis, but together make up about 10% of the total background. Physics processes with one or more top quarks in the final state, such as $t\bar{t}$ or Wt, are suppressed by applying a b-jet veto and, in the case of Wt, by the small cross section. The WW contribution is greatly reduced by first requiring that the two leptons have an invariant mass compatible with that of a Z boson, and then by applying a $E_{\mathrm{T}}^{\mathrm{miss}}$ cut. Finally, the $Z \to \tau\tau$ is suppressed as the two leptons resulting from the τ decay usually have a lower invariant mass than the Z boson due to the presence of neutrinos which removes part of the measurable energy ($\tau \to e^{-}\bar{\nu_e}\nu_\tau$ or $\tau \to \mu^{-}\bar{\nu_\mu}\nu_\tau$).

7.3.1 The Opposite Flavour Lepton ($e\mu$) Method

The contribution of these backgrounds is estimated from data through a dedicated control region, called the $e\mu$ control region, or $e\mu$CR, built with the same selections as the signal region, apart from the requirement of two opposite flavour leptons (see Table reftab:emuCRDefinition).

Selecting opposite flavour leptons takes advantage of the fact that WW, $t\bar{t}$, Wt and $Z \to \tau\tau$ backgrounds all decay into $ee : \mu\mu : e\mu$ channels with the relative probabilities of $1 : 1 : 2$. There are few backgrounds apart from the ones listed that decay into the $e\mu$ channel. This allows the measurement of the yields of these backgrounds directly from data using the $e\mu$ final state. The contribution in the signal region is obtained by considering the difference in the relative probability, and the electron/muon reconstruction efficiency, accounted in the ϵ-*factor*, defined as

$$\epsilon^2 = \frac{N_{ee}}{N_{\mu\mu}}, \tag{7.3}$$

where N_{ee} and $N_{\mu\mu}$ are respectively the number of ee and $\mu\mu$ events with an invariant mass compatible with that of a Z boson.

With this definition, the number of $e\mu$ background events in the signal region is

$e\mu$**CR definition**	
Lepton	Opposite flavour Opposite sign leptons ($e^{\pm}\mu^{\mp}$) $p_{\mathrm{T}} > 20(30)$ GeV leading(subleading)
No 3rd Lepton	Vetoed with Loose ID and p_{T} >7 GeV
Z mass window	$76 < m(e\mu) < 106$ GeV
$E_{\mathrm{T}}^{\mathrm{miss}}$	> 90 GeV
$\Delta R(e,\mu)$	< 1.8 rad
$\Delta\phi(Z, E_{\mathrm{T}}^{\mathrm{miss}})$	> 2.7 rad
$\lvert\lvert\mathbf{p}_{\mathrm{T}}^{\mathrm{miss}} + \Sigma\mathbf{p}_{\mathrm{T}}(\mathrm{jet})\rvert - \mathbf{p}_{\mathrm{T}}(Z)\rvert / p_{\mathrm{T}}(Z)$	$< 0.2\%$
$\Delta\phi(\mathrm{jet}, E_{\mathrm{T}}^{\mathrm{miss}})_{\mathrm{min}}$	> 0.6 rad for jets > 25 GeV
$p_{\mathrm{T}}(Z)/m_{\mathrm{T}}$	< 0.9
b-jet veto	for b-jets > 20 GeV, $\lvert\eta\rvert < 2.5$, tagged at 85%

Table 7.5: Event selection applied to define the $e\mu$ Control Region. The control region reflects the SR definition apart from the opposite flavour requirement of the two selected leptons.

obtained as

$$N^{e\mu}_{\mathrm{SR}ee} = \frac{1}{2} \times \epsilon \times N^{\mathrm{data,sub}}_{e\mu}$$
$$N^{e\mu}_{\mathrm{SR}\mu\mu} = \frac{1}{2} \times \frac{1}{\epsilon} \times N^{\mathrm{data,sub}}_{e\mu}, \tag{7.4}$$

where $N^{\mathrm{data,sub}}_{e\mu}$ is the number of $e\mu$ data events in the CR, estimated as

$$N^{\mathrm{data,sub}}_{e\mu} = N^{\mathrm{data}}_{e\mu} - N^{\mathrm{other}}_{\mathrm{sub}}. \tag{7.5}$$

$N^{\mathrm{other}}_{\mathrm{sub}}$ is defined as the non-$WW/t\bar{t}/Wt/Z \to \tau\tau$ background subtracted using data-driven (DD) estimates where available, or MC simulations where no DD estimates are available from

$$N^{\mathrm{other}}_{\mathrm{sub}} = \sum_{i}^{\mathrm{non}-e\mu} N_i. \tag{7.6}$$

The control region is defined with two opposite flavour leptons in order to keep the contribution from $N^{\mathrm{other}}_{\mathrm{sub}}$ small. Most of the signal region cuts are built to select contributions from processes with a Z boson, which (aside from $Z \to \tau\tau$) should be eliminated by the opposite flavour requirement. This method is robust when $N^{\mathrm{other}}_{\mathrm{sub}}$ is small.

7.3.2 Data-Driven Estimation in the $e\mu$CR

The estimation of $e\mu$ background is obtained from data. The modelling of the variables used to define the CR is checked with data. As can be seen in Figure 7.5, most distributions are statistically consistent after the Z mass window selection. The number of jets is modelled well in MC up to a jet multiplicity of about five, and the b-jets multiplicity up to about two. The selection cuts that are applied subsequently include a b-jet veto and others that remove events with a higher number of jets, so a discrepancy here does not affect the results. In general, statistical consistency is observed between data and MC in events with a lower number of jets which is considered for the signal region.

The efficiency factor, ϵ, is extracted from the data after the Z mass window selection according to Equation 7.3. This factor is found to be $\mathbf{0.9018 \pm 0.0002(stat)}$. The total number of events from these backgrounds falling into the signal region is calculated from the number of data events passing the $e\mu$CR selection, and using Equation 7.4, and this ϵ factor. Since the expected number of events from MC is on the order of ten, the shape of $E^{\mathrm{miss}}_{\mathrm{T}}$ in data will have insufficient statistics. There-

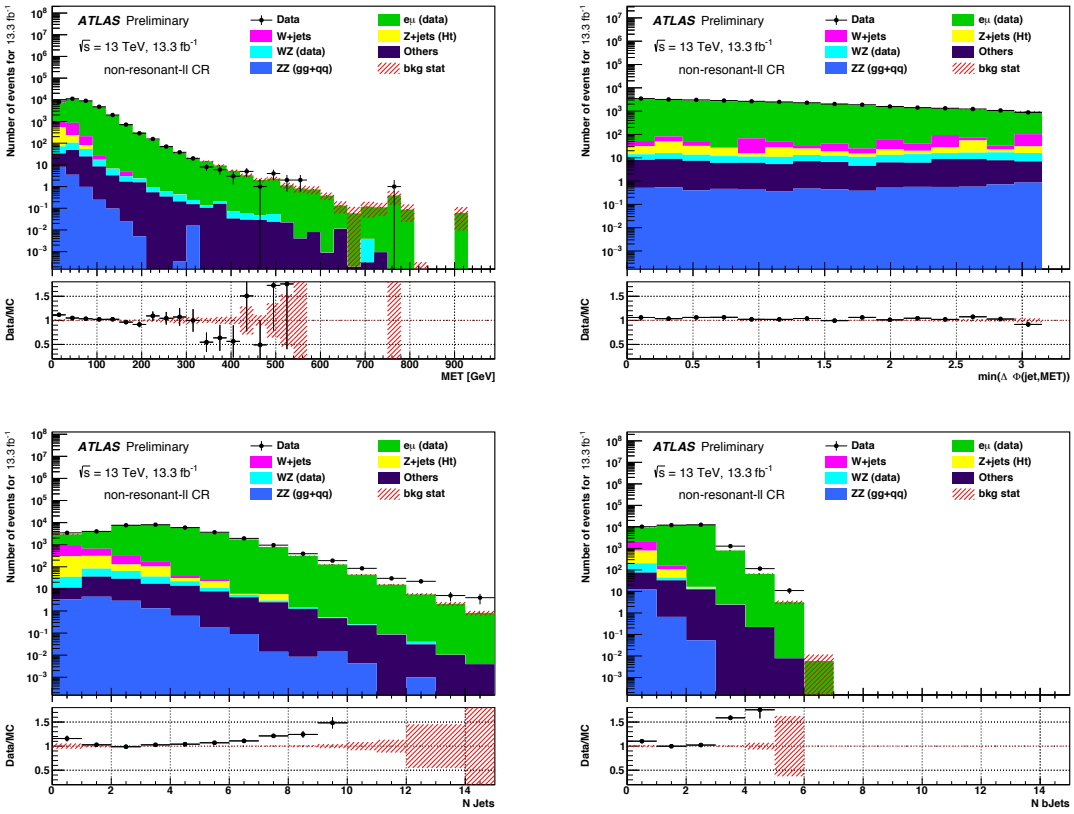

Figure 7.5: Data-MC comparison in the $e\mu$ Control Region after the Z mass requirement of the $E_{\mathrm{T}}^{\mathrm{miss}}$ distribution (a), the angular distribution between the $E_{\mathrm{T}}^{\mathrm{miss}}$ and leading jet (b), the number of jets (c), and the number of b-jets (d).

fore, the shape of the $E_{\mathrm{T}}^{\mathrm{miss}}$ will be used from the MC, and the relative scale factors calculated from data will normalize the yields. Shape variations were not considered for the systematic uncertainty, though this should be a future consideration.

7.3.3 MC Closure and Estimation of Systematic Error

The check to see if a background estimation method is valid is often referred to as the 'closure' of the method. The closure of this method is verified through MC to ensure that the method is self-consistent. The estimation method is performed on the full set of MC ($N_{e\mu}^{\mathrm{MC}}$) and the $e\mu$ event yields that are predicted from the method are compared with the expected number of events from the $e\mu$ MC in the signal region ($N_{e\mu}^{\mathrm{est}}$).

In order to perform this verification, the efficiency factor is extracted from the MC events with same flavour and opposite sign leptons, after applying a Z mass cut of $76 < m(e\mu) < 106$ GeV for the $e\mu$ processes (WW, $t\bar{t}$ Wt and $Z \to \tau\tau$). This efficiency factor is found to be 0.954 ± 0.003. It is used only to assess the closure of the method and estimate the systematic uncertainty. It is applied to the full set of MC in the signal region. The number of events obtained this way is then compared with the number of events found in the signal region for the $e\mu$ MC backgrounds alone. The comparison, which shows good agreement, is given in Table 7.6.

	$N_{e\mu}^{\mathrm{MC}}$	$N_{e\mu}^{\mathrm{est}}$
SR ee	15.2 ± 1.6	14.8 ± 1.0
SR $\mu\mu$	15.0 ± 1.4	16.2 ± 1.1

Table 7.6: Closure of the $e\mu$ backgrounds estimation. $N_{e\mu}^{\mathrm{MC}}$ is the expected event yields for the $e\mu$ background from adding up the MC estimated contributions in the signal region, while $N_{e\mu}^{\mathrm{est}}$ is the number of $e\mu$ events in the signal region estimated by applying the MC efficiency factor (0.954 ± 0.003) to the full set of MC. Numbers are normalized to 13.3 fb^{-1}. Errors quoted are from statistical uncertainty.

Further validations on the method are done by observing the amount of $e\mu$ background obtained as each subsequent cut, listed in Table 7.5, is applied. Table 7.7 reports the breakdown of backgrounds in this control region. It can be observed that the events remaining in the final control region are more than 95% $e\mu$ events. Fur-

ther, the sum of the other backgrounds is quite small ($< 5\%$), as was required for the method to be valid.

	Diboson		$e\mu$				others
	ZZ	WZ	WW	$Z \to \tau\tau$	$t\bar{t}$	Wt	
$m(e\mu)$	12.99 ± 0.32	111.2 ± 1.9	2604 ± 26	2013 ± 99	25555 ± 52	2200 ± 13	1988 ± 151
$E_{\mathrm{T}}^{\mathrm{miss}}$	0.144 ± 0.038	5.25 ± 0.35	96.3 ± 4.9	6.5 ± 3.2	2985 ± 18	204 ± 4	10.1 ± 2.1
$\Delta R_{e\mu}$	0.047 ± 0.025	2.19 ± 0.23	31.7 ± 2.7	4.8 ± 3.0	527 ± 8	53.2 ± 2.2	2.9 ± 0.4
$\Delta\phi(Z, E_{\mathrm{T}}^{\mathrm{miss}})$	0.033 ± 0.013	0.21 ± 0.06	4.18 ± 1.13	0 ± 0	46.7 ± 2.2	5.88 ± 0.69	0.28 ± 0.02
Fractional p_{T}	0.030 ± 0.013	0.21 ± 0.06	4.18 ± 1.13	0 ± 0	44.9 ± 2.2	5.54 ± 0.66	0.27 ± 0.02
$\Delta\phi_{jet-E_{\mathrm{T}}^{\mathrm{miss}}}$	0.030 ± 0.013	0.20 ± 0.06	4.18 ± 1.13	0 ± 0	41.6 ± 2.1	5.42 ± 0.66	0.26 ± 0.02
$p_{\mathrm{T}}(Z)/m_{\mathrm{T}}$	0.030 ± 0.013	0.20 ± 0.06	4.18 ± 1.13	0 ± 0	41.6 ± 2.1	5.42 ± 0.66	0.25 ± 0.02
b-jet Veto	0.029 ± 0.012	0.18 ± 0.06	4.11 ± 1.11	0 ± 0	5.5 ± 0.7	2.05 ± 0.44	0.13 ± 0.02

Table 7.7: The number of MC events remaining broken down by physics process that contribute to the $e\mu$ final state after each of the cuts for the $e\mu$CR is applied sequentially. The main sources of background for the analysis are listed (ZZ, WZ) as well as those for $e\mu$: WW, $t\bar{t}$, Wt, and $Z \to \tau\tau$. The 'others' category includes W+jets, single-top, and Z+jets processes. Numbers smaller than 0.01 are rounded to 0 in this table. Numbers are normalized to a data sample of 13.3 fb^{-1}.

The systematic error for the background estimates is due to an uncertainty on the efficiency factor. This uncertainty comes from the efficiency factor dependency on the kinematics (p_{T}, η) of the leptons in the event. To take this effect into account, the efficiency factor (ϵ as defined in Equation 7.3) has been evaluated using all MC processes listed in Table 7.7 and comparing them against ϵ calculated from $e\mu$ MC backgrounds. The relative difference between the two values was then taken as a systematic uncertainty on the final data estimates (shown in Table 7.8).

A final comparison among data and MC estimates with statistical and systematic errors is provided in Table 7.9.

ϵ-factor	MC ($e\mu$)	MC (All)	% difference
After m($e\mu$) cut	0.954 $\pm$ 0.003	0.900 $\pm$ 0.001	**6.0%**

Table 7.8: The efficiency factor measured from the $e\mu$ MC background after the Z mass window cut, with its statistical error. In this table the difference is calculated between the ϵ-factor evaluated with $e\mu$ MC (WW, $t\bar{t}$, Wt, and $Z \to \tau\tau$) and the factor evaluated with all MC.

	Background event estimates in data from $e\mu$	MC expected events
SR ee	**16.9 $\pm$ 2.8 $\pm$ 1.0**	(15.2 $\pm$ 1.6)
SR $\mu\mu$	**20.7 $\pm$ 3.4 $\pm$ 1.2**	(15.0 $\pm$ 1.4)

Table 7.9: The estimated background events from data for WW, $t\bar{t}$, Wt, and $Z \to \tau\tau$ backgrounds in the signal region with statistical and systematic errors. The systematic error is calculated taking into account the uncertainty on the efficiency factor evaluation.

7.4 Z+jets Background

The Z+jets background is largely reduced by the $E_{\mathrm{T}}^{\mathrm{miss}}$ requirement, as well as other selections applied in the SRs, namely the angular requirements: $\Delta R_{\ell\ell}$, $\Delta\phi(Z, E_{\mathrm{T}}^{\mathrm{miss}})$, $\Delta\phi(\mathrm{jet}(p_{\mathrm{T}}, E_{\mathrm{T}}^{\mathrm{miss}})$, and the fractional p_{T} difference. All of these selection cuts contribute to the reduction of the Z+jets, resulting in a small number of events left in the SRs. However, this background has significant uncertainties, as the modelling of $E_{\mathrm{T}}^{\mathrm{miss}}$ mismeasurement in the MC depends strongly on the correct modelling of detector, pileup interactions, the jet energy response and the track reconstruction. It is thus crucial to estimate it with the data.

The Z+jets background was estimated by an independent data-driven method. This method is known as the 'ABCD method'. The idea behind the ABCD method is to reverse two of the event selection cuts to enhance the background, and use ratios between the four defined regions (A, B, C, and D) to predict the number of events coming from Z+jets in the signal region, A. This is simply A = C * B / D. The yields from the ABCD CR can be used to normalize those obtained from MC simulation.

7.4.1 ABCD Method

The ABCD method is a data-driven technique that is used to estimate the number of background events in a defined SR, giving the number of events found in side-band regions built in such a way to be enriched in background events and poor in signal events. Sideband regions are built by reversing the selections on the fractional p_{T} difference and $\Delta\phi(Z, E_{\mathrm{T}}^{\mathrm{miss}})$ to enhance the Z+jets background. The signal and sideband regions are defined as shown in Figure 7.6.

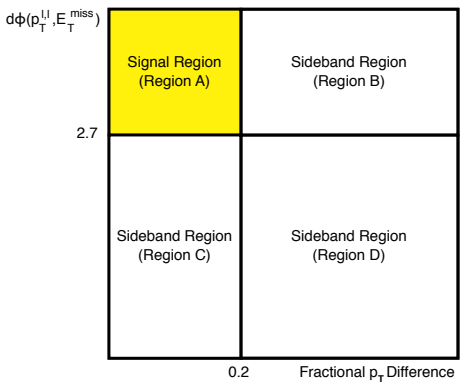

Figure 7.6: The signal and sideband regions considered in the ABCD method.

These variables are chosen due to their low correlation, as can be seen in Figure 7.7. The correlation coefficient is -0.0504 (-0.006) for the ee-channel ($\mu\mu$-channel) at the event selection step of the Z mass window (Table 6.5). This combination of variables is chosen instead of other possible combinations using the $\Delta R_{\ell\ell}$, since $\Delta R_{\ell\ell}$ has

a large correlation with the $E_{\mathrm{T}}^{\mathrm{miss}}$. After the $E_{\mathrm{T}}^{\mathrm{miss}}$ cut, the statistics in the Z+jets background is greatly reduced, making it difficult to have enough statistics to execute the ABCD method. However, the correlations have been observed to change after further event selections, which will lead to a greater uncertainty (referred to as a 'lack of closure') on the method. This will be accounted for in the systematics estimation.

Due to the initial lack of closure (see Section 7.4.2) for the ABCD method, the kinematic cut $p_{\mathrm{T}}(Z)/m_{\mathrm{T}}$ was added to the selection. The lack of closure of the method without the $p_{\mathrm{T}}(Z)/m_{\mathrm{T}}$ selection is due to the reversed $\Delta\phi(Z, E_{\mathrm{T}}^{\mathrm{miss}})$ cut. This cut reversal was used to construct the sideband regions C and D, which consequently contained many more events with badly balanced Z boson and $E_{\mathrm{T}}^{\mathrm{miss}}$. Thus, these regions have a sizeable overestimation of the Z+jets background contributions. This problem persists unless the $p_{\mathrm{T}}(Z)/m_{\mathrm{T}}$ cut is applied. The impact of requiring $p_{\mathrm{T}}(Z)/m_{\mathrm{T}} < 0.9$ for both the signal and background events in the signal region is found to be negligible, and thus does not affect the signal significance.

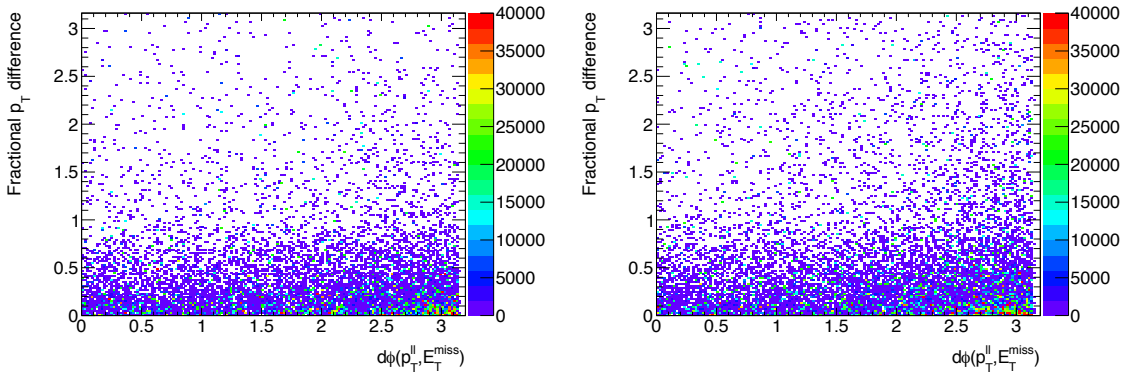

Figure 7.7: Correlation of the variables $\Delta\phi(Z, E_{\mathrm{T}}^{\mathrm{miss}})$ and fractional p_{T} difference are presented for the (a) ee- and (b) $\mu\mu$-channels. The Z mass requirement and looser selection of $E_{\mathrm{T}}^{\mathrm{miss}} > 70$ GeV are applied.

Provided the two variables are uncorrelated, the Z+jets background in the signal region can be estimated with the following equation:

$$N_A^{\mathrm{est}} = N_C^{\mathrm{obs,sub}} \times \frac{N_B^{\mathrm{obs,sub}}}{N_D^{\mathrm{obs,sub}}}, \tag{7.7}$$

where N_A^{est} is the number of estimated background events in the SR, while $N_X^{\mathrm{obs,sub}}$ (X = B, C, D) are the numbers of observed events in side-band regions. The contribution of non-Z+jets background is subtracted before applying this equation. The normalization factor $N_B^{\mathrm{obs,sub}}/N_D^{\mathrm{obs,sub}}$ is taken from inclusive event yields after a looser

selection with all cuts up to and including the Z mass window as listed in Table 7.10.

ABCD CR definition	
Lepton	Same flavour Opposite sign leptons (e^+e^-, $\mu^+\mu^-$) $p_{\mathrm{T}} > 20(30)$ GeV leading(subleading)
No 3rd Lepton	Vetoed with Loose ID and p_{T} >7 GeV
$\Delta\phi(Z, E_{\mathrm{T}}^{\mathrm{miss}}) > 2.7$ rad (nominal) OR $\Delta\phi(Z, E_{\mathrm{T}}^{\mathrm{miss}}) < 2.7$ (reversed)	
fractional $p_{\mathrm{T}} < 0.2\%$ (nominal) OR fractional $p_{\mathrm{T}} > 0.2\%$ (reversed)	
Z mass window	$76 < m(\ell^+\ell^-) < 106$ GeV
$p_{\mathrm{T}}(Z)/m_{\mathrm{T}}$	< 0.9
$\Delta\phi(\mathrm{jet}, E_{\mathrm{T}}^{\mathrm{miss}})_{\mathrm{min}}$	> 0.6 rad for jets > 25 GeV
b-jet veto	for b-jets > 20 GeV, $\lvert\eta\rvert < 2.5$, tagged at 85%
$E_{\mathrm{T}}^{\mathrm{miss}}$	> 90 GeV
$\Delta R(e, \mu)$	< 1.8 rad

Table 7.10: Event selection applied to define the ABCD Control Region. The control region reflects the SR definition when the nominal cuts are applied.

Figures 7.8 and 7.9 show the $E_{\mathrm{T}}^{\mathrm{miss}}$ distributions in all the regions after the Z mass requirement. A correction to the Z boson p_{T} MC was applied to correct to the Z p_{T} distribution in data. This is referred to as Z p_{T} reweighting. Statistical consistency is observed through the majority of the distribution between the data and MC at this cut level.

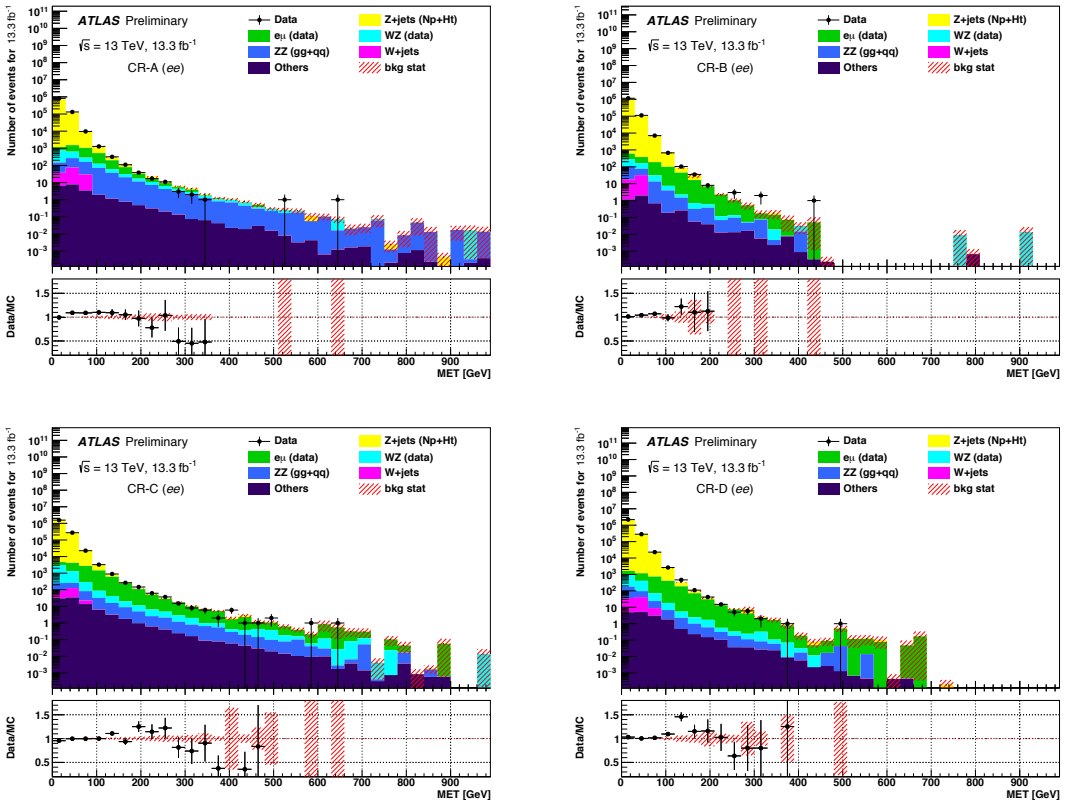

Figure 7.8: $E_{\mathrm{T}}^{\mathrm{miss}}$ distributions in the signal (a) and sideband regions (b–d) after the Z mass requirement for the ee-channel. Z p_{T} reweighting is applied to the MadGraph Z samples. MC samples are normalized to their cross section values as given in Chapter 5 and re-scaled to 13.3 fb^{-1}data integrated luminosity.

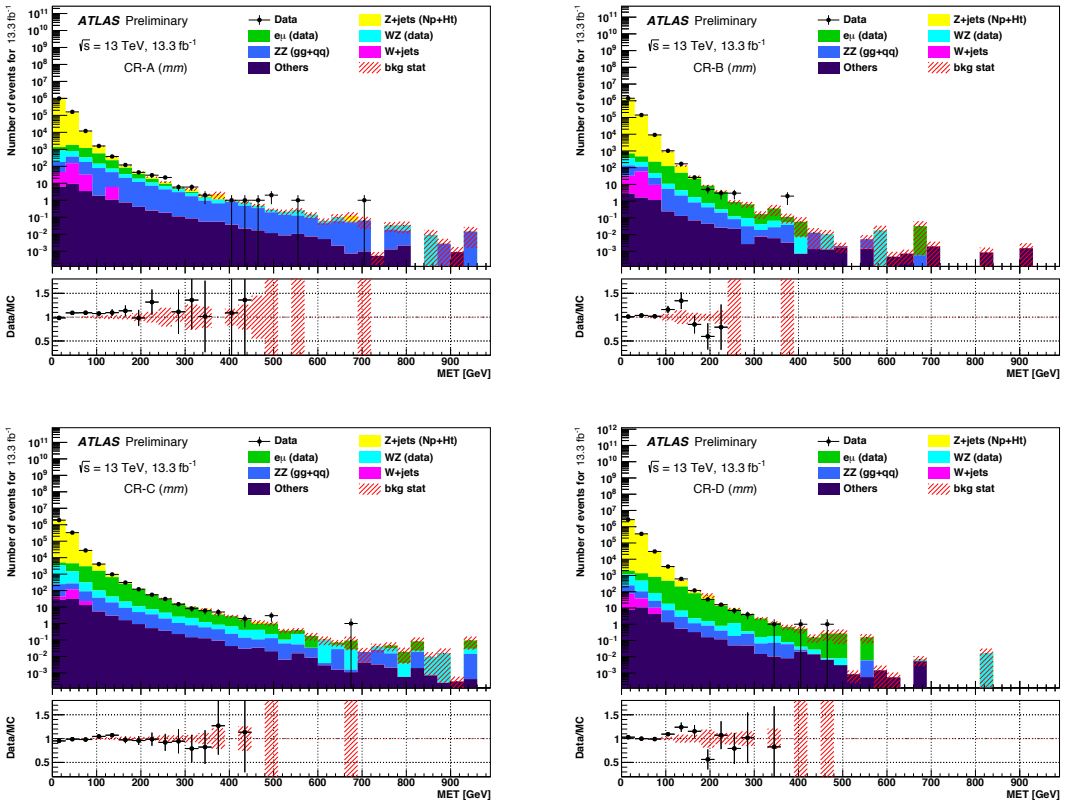

Figure 7.9: $E_{\mathrm{T}}^{\mathrm{miss}}$ distributions in the signal (a) and sideband regions (b–d) after the Z mass requirement for the $\mu\mu$-channel. Z p_{T} reweighting is applied to the MadGraph Z samples. MC samples are normalized to their cross section values as given in Chapter 5 and re-scaled to 13.3 fb^{-1}data integrated luminosity.

7.4.2 MC Closure

As before, a check to see if a background estimation method is valid is often referred to as the 'closure' of the method. The closure of this ABCD method is checked through MC by using the two different ratios to ensure that the method is self-consistent, and comparing the ratios at different steps in the cutflow. As constructed, the ABCD method works up to the Z mass cut, where the elements of the method are defined. As alluded to earlier, once more cuts are applied, the agreement gets worse. However, this disagreement can be estimated and taken into account with systematic uncertainties. Uncertainties are introduced as more cuts are applied, as the cuts are designed to get rid of backgrounds such as Z+jets. Therefore, the number of events in the MC is quite low. The method uses ratios and background subtraction, both of which can introduce large errors when dealing with small statistics. As can be seen in Figures 7.10 and 7.11, the statistics in CR-B and CR-D are low after all of the selections.

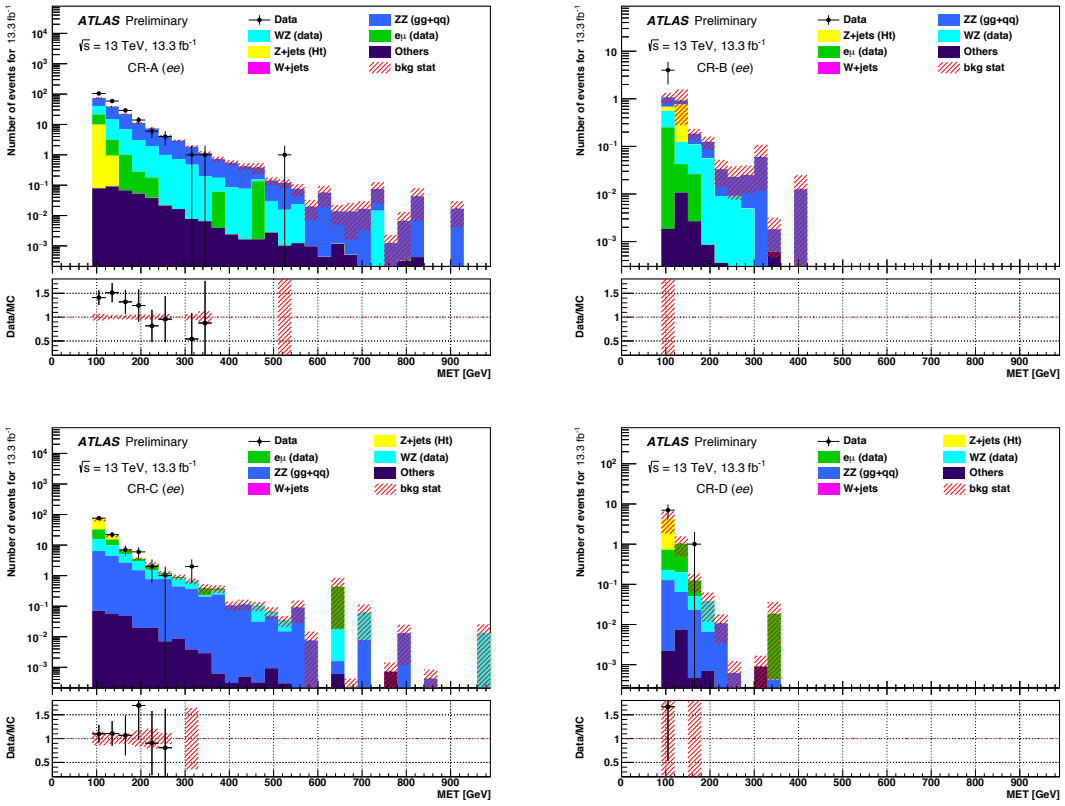

Figure 7.10: $E_{\mathrm{T}}^{\mathrm{miss}}$ distributions in the signal (a) and sideband regions (b–d) after all requirements for the ee-channel. Z p_{T} reweighting is applied to the MadGraph Z samples. MC samples are normalized to their cross section values as given in Chapter 5 and re-scaled to 13.3 fb^{-1}data integrated luminosity.

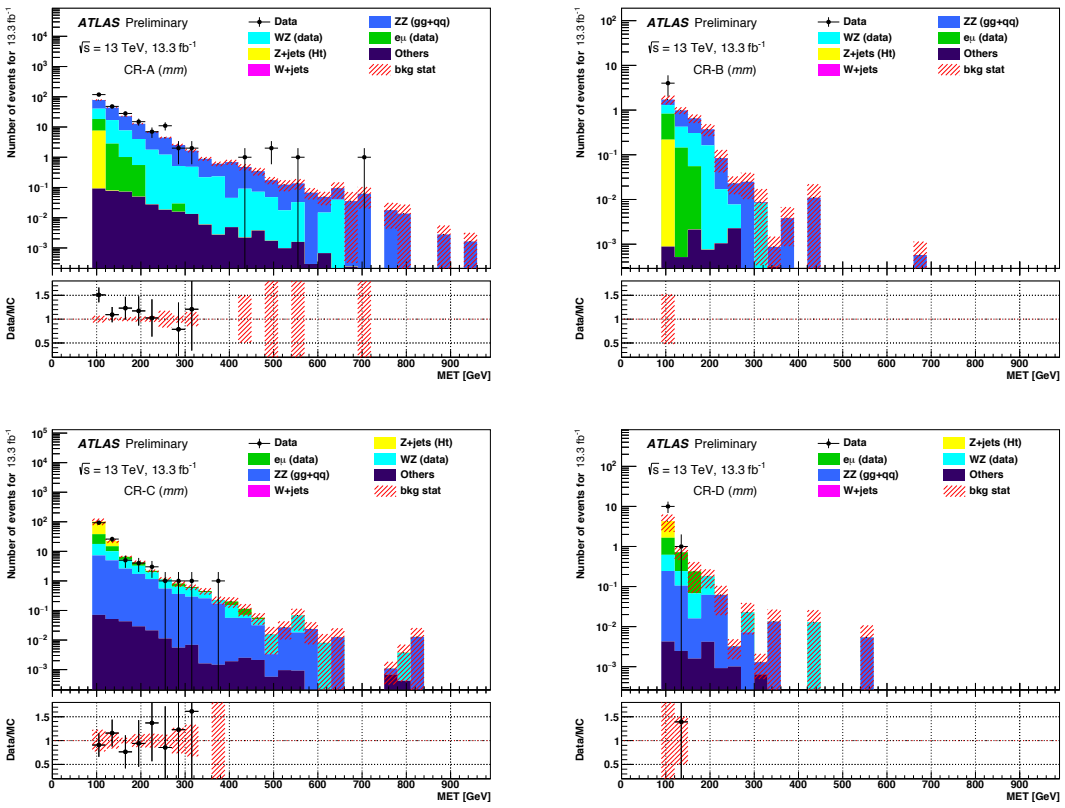

Figure 7.11: $E_{\mathrm{T}}^{\mathrm{miss}}$ distributions in the signal (a) and sideband regions (b–d) after all requirements for the $\mu\mu$-channel. Z p_{T} reweighting is applied to the MadGraph Z samples. MC samples are normalized to their cross section values as given in Chapter 5 and re-scaled to 13.3 fb^{-1}data integrated luminosity.

Tables 7.11 and 7.12 show the breakdown of the scaling factors against the selection cuts for the ee- and $\mu\mu$-channels respectively. The event ratios are consistent between N_A/N_C and N_B/N_D for both channels. Statistical consistency between the data and MC is observed for N_B/N_D. After applying $E_{\mathrm{T}}^{\mathrm{miss}} > 90$ GeV, the statistics become too low to tell whether the scaling factors are stable, though a statistically significant deviation is not observed. When looser $E_{\mathrm{T}}^{\mathrm{miss}}$ requirements are applied ($E_{\mathrm{T}}^{\mathrm{miss}} > 30$, 60, 90 GeV), the factors are consistent within the uncertainty between the two regions. There is a decreasing tendency in the sideband ratios against the $E_{\mathrm{T}}^{\mathrm{miss}}$ requirement (and also for the $\Delta\mathrm{R}_{\ell\ell}$). This tendency is considered as a systematic uncertainty.

	N_A/N_C [MC]	N_B/N_D [MC]	N_B/N_D [Data]
Z mass	0.496 ± 0.001	0.519 ± 0.001	0.5081 ± 0.0006
$p_{\mathrm{T}}(Z)/m_{\mathrm{T}}$	1.049 ± 0.003	0.733 ± 0.002	0.7180 ± 0.0009
$\Delta\phi(\mathrm{jet}, E_{\mathrm{T}}^{\mathrm{miss}})$	1.018 ± 0.004	0.734 ± 0.002	0.7176 ± 0.0009
b-jet veto	1.06 ± 0.004	0.743 ± 0.002	0.7283 ± 0.0009
$E_{\mathrm{T}}^{\mathrm{miss}} > 30$ GeV	0.626 ± 0.005	0.454 ± 0.003	0.470 ± 0.002
$E_{\mathrm{T}}^{\mathrm{miss}} > 60$ GeV	0.45 ± 0.01	0.337 ± 0.009	0.34 ± 0.005
$E_{\mathrm{T}}^{\mathrm{miss}} > 90$ GeV	0.31 ± 0.03	0.32 ± 0.03	0.28 ± 0.01
$\Delta\mathrm{R}_{\ell\ell} < 1.8$ [Full SR]	0.32 ± 0.08	0.2 ± 0.2	0.4 ± 0.4

Table 7.11: Breakdown of scaling factors: N_A/N_C, N_B/N_D for the ee channel. Only the statistical errors are shown. The data have MC backgrounds subtracted before the ratio is calculated. MadGraph samples are used for the Z+jets background. Selections are applied sequentially on top of the previous rows.

	N_A/N_C [MC]	N_B/N_D [MC]	N_B/N_D [Data]
Z mass	0.501 ± 0.001	0.508 ± 0.001	0.4980 ± 0.0005
$p_{\mathrm{T}}(Z)/m_{\mathrm{T}}$	1.043 ± 0.004	0.717 ± 0.002	0.7032 ± 0.0008
$\Delta\phi(\mathrm{jet}, E_{\mathrm{T}}^{\mathrm{miss}})$	1.089 ± 0.006	0.718 ± 0.002	0.7026 ± 0.0008
b-jet veto	1.053 ± 0.004	0.727 ± 0.002	0.7133 ± 0.0008
$E_{\mathrm{T}}^{\mathrm{miss}} > 30$ GeV	0.604 ± 0.005	0.439 ± 0.003	0.456 ± 0.001
$E_{\mathrm{T}}^{\mathrm{miss}} > 60$ GeV	0.44 ± 0.01	0.33 ± 0.009	0.337 ± 0.004
$E_{\mathrm{T}}^{\mathrm{miss}} > 90$ GeV	0.34 ± 0.03	0.29 ± 0.02	0.31 ± 0.01
$\Delta\mathrm{R}_{\ell\ell} < 1.8$ [Full SR]	0.2 ± 0.1	0.2 ± 0.1	0.02 ± 0.26

Table 7.12: Breakdown of scaling factors: N_A/N_C, N_B/N_D for the $\mu\mu$ channel. Only the statistical errors are shown. The data have MC backgrounds subtracted before the ratio is calculated. MadGraph samples are used for the Z+jets background. Selections are applied sequentially on top of the previous rows.

Closure tests are performed for the looser selections, as shown in Tables 7.13 and 7.14, for the background analysis. The effect of a smaller $E_{\mathrm{T}}^{\mathrm{miss}}$ cut was observed, and the loosest selection (at Z mass) was compared to subsequent cuts. There is a difference in agreement between the MC and the method that is taken as a measure of systematic uncertainty, as detailed in the next section. There are evident differences seen between data (ABCD column) and the ABCD method on MC in the final yields, Table 7.15. The systematic errors are estimated in the next section to account for the differences introduced through the ABCD method.

	MC expected events (ee)	Est. from sideband (ee)
Z mass	$(1.022 \pm 0.002) \times 10^6$	$(1.069 \pm 0.01) \times 10^6$
$p_{\mathrm{T}}(Z)/m_{\mathrm{T}}$	$(8.77 \pm 0.02) \times 10^5$	$(4.34 \pm 0.01) \times 10^5$
$\Delta\phi(\mathrm{jet}, E_{\mathrm{T}}^{\mathrm{miss}})$	$(7.94 \pm 0.02) \times 10^5$	$(4.02 \pm 0.01) \times 10^5$
b-veto	$(7.85 \pm 0.02) \times 10^5$	$(3.84 \pm 0.01) \times 10^5$
$E_{\mathrm{T}}^{\mathrm{miss}} > 30$ GeV	$(9.69 \pm 0.06) \times 10^4$	$(8.02 \pm 0.02) \times 10^4$
$E_{\mathrm{T}}^{\mathrm{miss}} > 60$ GeV	$(5.60 \pm 0.14) \times 10^3$	$(6.46 \pm 0.11) \times 10^3$
$E_{\mathrm{T}}^{\mathrm{miss}} > 90$ GeV	364 ± 29	602 ± 29
$\Delta\mathrm{R}_{\ell\ell}$	12.8 ± 3.0	23.1 ± 3.1

Table 7.13: Closure tests for the ABCD method using the MC expected events in the ee-channel. The $\Delta\phi(Z, E_{\mathrm{T}}^{\mathrm{miss}})$ and fractional p_{T} difference cuts are already applied for all the numbers in order to use the ABCD method. The statistical uncertainties are shown for both columns. The differences between data estimates and MC expectations are used to estimate the systematic uncertainty on the method.

	MC expected events ($\mu\mu$)	Est. from sideband ($\mu\mu$)
Z mass	$(1.167 \pm 0.003) \times 10^6$	$(1.183 \pm 0.002) \times 10^5$
$p_{\mathrm{T}}(Z)/m_{\mathrm{T}}$	$(1.005 \pm 0.002) \times 10^6$	$(4.89 \pm 0.01) \times 10^5$
$\Delta\phi(\mathrm{jet}, E_{\mathrm{T}}^{\mathrm{miss}})$	$(9.11 \pm 0.02) \times 10^5$	$(4.54 \pm 0.01) \times 10^5$
b-veto	$(9.01 \pm 0.02) \times 10^5$	$(4.34 \pm 0.01) \times 10^5$
$E_{\mathrm{T}}^{\mathrm{miss}} > 30$ GeV	$(1.09 \pm 0.01) \times 10^5$	$(9.16 \pm 0.05) \times 10^4$
$E_{\mathrm{T}}^{\mathrm{miss}} > 60$ GeV	$(6.54 \pm 0.02) \times 10^3$	$(7.48 \pm 0.01) \times 10^3$
$E_{\mathrm{T}}^{\mathrm{miss}} > 90$ GeV	468 ± 37	709 ± 32
$\Delta\mathrm{R}_{\ell\ell}$	13.0 ± 3.0	31.7 ± 7.2

Table 7.14: Closure tests for the ABCD method using the MC expected events in the $\mu\mu$-channel. The $\Delta\phi(Z, E_{\mathrm{T}}^{\mathrm{miss}})$ and fractional p_{T} difference cuts are already applied for all the numbers in order to use the ABCD method. The statistical uncertainties are shown for both columns.

7.4.3 Estimated Yields and Systematic Error

Systematic uncertainties originate from the MC subtraction, the stability of N_B/N_D against various kinematic cuts, and the level of closure using the ABCD method as discussed in the previous section. The columns in Table 7.15 show the estimated event yields of the Z+jets background in the ee- and $\mu\mu$-channels. These systematics were estimated by finding the maximal differences in ratios and yields as seen in the above tables.

The following systematic uncertainties are considered:

- Sideband ratio differences (from the difference in ratios from the Z mass row in Tables 7.11 and 7.12): 4.5% (ee), 2.0% ($\mu\mu$)
- Selection dependencies (from the difference in ratios between the Z mass and $E_{\mathrm{T}}^{\mathrm{miss}} > 90$ GeV cut in Tables 7.11 and 7.12): 64% (ee), 47% ($\mu\mu$)
- MC non-closure (taken at the Z mass selection in Tables 7.13 and 7.14 to avoid double-counting with the selection dependency): 4.4% (ee), 1.4% ($\mu\mu$)
- non-Z background subtraction: 12% (ee), 11% ($\mu\mu$)

The total systematic error on the Z+jets background as summarized here is **65.4%** (ee-channel), and **48.3%** ($\mu\mu$-channel). The statistical uncertainty of the non-Z backgrounds are included separately. These are summarized in Table 7.15.

	Background event estimates in data from ABCD	MC expected events
SR ee	**22.4 ± 4.8 ± 14.7**	(12.8 ± 3.0)
SR $\mu\mu$	**17.6 ± 4.0 ± 8.5**	(13.0 ± 3.0)

Table 7.15: Summary of the Z background estimation using the ABCD method with statistical and systematic uncertainties. The numbers in the parentheses are from the MC expectation with statistical uncertainties, using the averaged MadGraph Z+jets samples.

7.4.4 Estimation of $E_{\mathrm{T}}^{\mathrm{miss}}$ Shape

The MC estimates are scaled to the yields from the ABCD method. The shape is not extracted from the ABCD method due to the low statistics and a higher contamination of the non-Z backgrounds in the high $E_{\mathrm{T}}^{\mathrm{miss}}$ region. In order to increase the MC sample statistics, two complete Z+jets samples are averaged: those from Table 5.2 having the samples sliced by the number of partons, and those from Tables 5.3 and 5.4 sliced by the total energy in the event. The Z p_{T} reweighting is applied separately for each set of the $Z \to \mu\mu$ + jets samples due to a minor issue with the parton sliced sample (see Chapter 5.2.1 for details on the sample).

Due to the low number of Z+jets statistics remaining after all the signal region cuts are applied, the shape of the $E_{\mathrm{T}}^{\mathrm{miss}}$ distributions for this background is taken at an earlier step in the cutflow, and scaled to the number of events in data. The $\Delta\phi(E_{\mathrm{T}}^{\mathrm{miss}}, \mathrm{jets})$ and $p_{\mathrm{T}}(Z)/m_{\mathrm{T}}$ cuts are designed to remove Z+jets events, and so these cuts are eliminated, along with the b-jet veto cut. Then the total yield is scaled to the data values from Table 7.15 by 75% and 35% in the ee and $\mu\mu$ channels respectively. The shape of the $E_{\mathrm{T}}^{\mathrm{miss}}$ distribution that has been scaled can be seen in Figure 7.12. The shape variation is considered as a systematic on the Z+jets background as well.

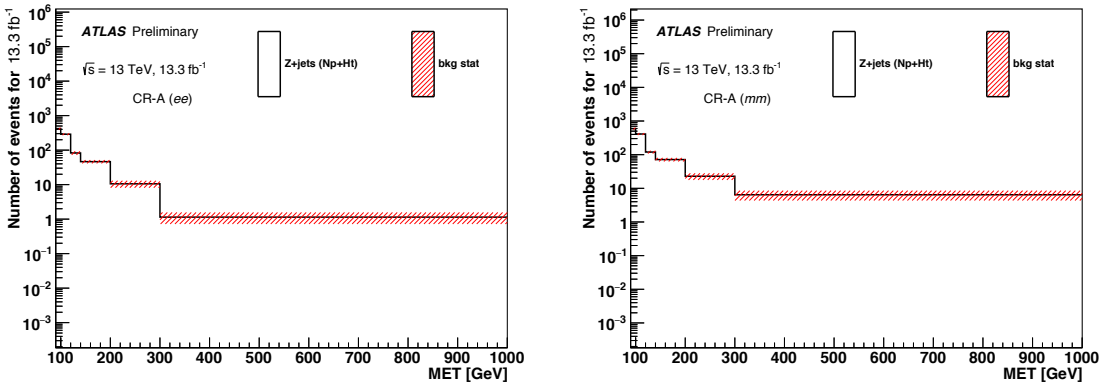

Figure 7.12: $E_{\mathrm{T}}^{\mathrm{miss}}$ shape in the ee signal (a) and $\mu\mu$ signal regions (b) for the Z+jets background obtained by removing the $\Delta\phi(E_{\mathrm{T}}^{\mathrm{miss}}, \mathrm{jets})$ and $p_{\mathrm{T}}(Z)/m_{\mathrm{T}}$ requirements, along with the b-jet veto. The shape is then scaled to the yield in the final signal region (after applying all of the cuts).

7.5 W+jets, ttV, Single-t, and VVV Backgrounds

The final set of backgrounds considered have a very small contribution to the final signal region, and so are only estimated through MC.

The triboson backgrounds, VVV have a small cross section for production (see Table 5.7), but end up in the signal region when one or more of the bosons is a Z boson. This is estimated with the same MC as the diboson background. Almost all of this background ends up in the signal region, as the analysis selections are not designed to remove this signature (aside from vetoing on a third lepton if it is reconstructed from leptonic decays of the third boson).

The ttV backgrounds are where one or more W or Z bosons are produced in conjunction with a $t\bar{t}$ pair. These processes have a very small cross section (see Table 5.5), but need to be considered, as their contribution can end up in the signal region, as the charged leptons may fall into the Z mass window requirement. As the analysis has a b-jet veto, the impact is reduced somewhat, as the t-quark often decays into a b-quark.

The process W+jets has a large cross section (see Table 5.6); however, due to the Z mass window cut and the large $E_{\mathrm{T}}^{\mathrm{miss}}$ requirement, it is eliminated entirely. This background was then estimated entirely through MC, though none of these events make it into the final signal regions.

Finally, the single top quark background is negligible due to rarely falling in the Z mass window, and being sensitive to the b-jet veto. It is included here for completeness, though no MC simulated events make it into the signal region.

The total contributions from these backgrounds are negligible, but are estimated with MC, and their systematic uncertainties are estimated from experimental uncertainties as explained in Chapter 8. The MC yields are summarized in Table 7.16.

	VVV	ttV	single-t	W+jets	Total
SR ee	0.362 ± 0.020	0.039 ± 0.007	0 ± 0	0 ± 0	**0.40 ± 0.02 ± 0.06**
SR $\mu\mu$	0.346 ± 0.014	0.045 ± 0.008	0 ± 0	0 ± 0	**0.39 ± 0.02 ± 0.06**

Table 7.16: Number of observed events for the W+jets, ttV, single-t, and VVV backgrounds for an integrated luminosity of 13.3 fb^{-1}. Errors quoted are statistical and systematic, where the systematic errors are evaluated from MC experimental systematics as described in the next section.

7.6 Summary of Background Results

The full results of the background estimates are given in Table 7.17. Where data-driven estimates are available, they are included in a separate column. The data and results from two dark matter signal simulations are included here as well.

	ee channel		$\mu\mu$ channel	
Data	220		236	
	ee (MC only)	ee (Data-driven)	$\mu\mu$ (MC only)	$\mu\mu$ (Data-driven)
$m_\chi = 1$ GeV, $m_{\text{med}} = 10$ GeV	198 ± 14 ± 16	-	187 ± 14 ± 18	-
$m_\chi = 50$ GeV, $m_{\text{med}} = 300$ GeV	48.6 ± 7.0 ± 2.8	-	51.5 ± 7.2 ± 2.8	-
$q\bar{q} \to ZZ$	90.4 ± 1.4 ± 5.8	-	97.2 ± 1.5 ± 8.0	-
$gg \to ZZ$	5.6 ± 0.1 ± 3.3	-	5.7 ± 0.1 ± 3.4	-
WZ	35.2 ± 0.9	44.0 ± 1.1 ± 3.3	40.4 ± 1.0	50.5 ± 1.2 ± 3.3
$WW/t\bar{t}/Wt/Z\tau\tau$	15.2 ± 1.6	16.9 ± 2.8 ± 1.0	15.0 ± 1.4	20.7 ± 3.4 ± 1.2
Z+jets	12.8 ± 3.0	22.4 ± 4.8 ± 15	13.0 ± 3.0	17.6 ± 4.0 ± 8.5
other	0.40 ± 0.02 ± 0.06	-	0.39 ± 0.02 ± 0.06	-
Total Bkg.	160 ± 4 ± 7	180 ± 6 ± 17	172 ± 4 ± 9	192 ± 6 ± 13

Table 7.17: The number of events observed in data and expected from MC (scaled to 13.3 fb^{-1}) in ee and $\mu\mu$ signal regions after full event selections, including two vector mediator model DM signal samples from Table 5.8. MC events are weighted to the luminosity of the data, and by the procedures described in the text. Estimates have statistical + systematic errors shown where available in both MC and data-driven estimations.

Chapter 8

Error Estimation

The estimation of errors on a measurement is as important as the measurement itself. Errors can be broken down into two categories: statistical and systematic uncertainties.

8.1 Statistical Uncertainties

Statistical uncertainties arise from a finite number of events and are improved by collecting more data or by generating more Monte Carlo. On the other hand, systematic uncertainties are theoretical and experimental considerations that arise from modelling and reconstructing events, and do not necessarily decrease with more data collection or MC generation. However, as systematics are often constrained or estimated through checks made through data techniques, they tend to decrease with more data.

Statistical uncertainty on the number of data events, N, is taken as the root of the number of events, $\sqrt{N}$. This is typically the largest source of statistical uncertainty. Another component of statistical uncertainty (which is usually rolled into the systematics on the background estimation) comes from the finite number of MC events generated. This statistical component of the error on the MC can be decreased by generating more events and this is done so that the statistical error is not dominant.

8.2 Systematic Uncertainties

Systematic uncertainties fall into two main categories. The first are the uncertainties arising from theoretical modelling. These include uncertainties from event generation and hadronization, and arise from the theoretical models used for the parton distribution functions, and the higher order QCD effects. The second category is those arising from detector performance modelling. These include uncertainties on various measurable quantities, including the luminosity of the LHC and all of the measurable objects in the ATLAS detector.

8.2.1 Theoretical Uncertainties

The theoretical uncertainties that are considered in this analysis are the QCD scale uncertainties, PDF uncertainties, and uncertainties arising from corrections going from leading order (LO) or next-to-leading order (NLO) to NLO or beyond (NNLO).

QCD Scale Uncertainties

These arise from the choice of the renormalization scale and the factorization scale. The QCD scale uncertainties on the MC samples are estimated by generating new sets with different scale values, half the nominal and twice the nominal, and observing how much the final yields change (Table 8.1, Line 7). These are done for all of the signal samples. QCD scale uncertainties are also calculated for the diboson ZZ and WZ samples. The uncertainties from QCD scale are $\sim 1-2\%$.

PDF Uncertainties

These arise from the choice of the proton parton distribution function, which has intra-PDF variations within a given model, or inter-PDF variations, from different theoretical models of the PDF. The nominal PDF set used for the dark matter samples is `NNPDF30_lo_as_0130`. Both intra- and inter-PDF uncertainties are estimated by making the variations, and checking the effect on the final yields in the MC signal samples (Table 8.1, Lines 12, 20). PDF uncertainties are also evaluated in background ZZ and WZ samples. For most samples, the PDF uncertainties are $1-2\%$ for the intra-PDF uncertainty, and $2-3\%$ for the inter-PDF uncertainties.

8.2.2 Experimental Uncertainties

Experimental uncertainties encompass those arising from calibrations and corrections on simulated reconstructed physics objects such as electrons, muons, and jets. The calibrations and corrections are compared to data and tuned to match the conditions in the detector and from the LHC, and the uncertainty for each parameter is estimated by dedicated working groups. The effect of these uncertainties is determined by varying these parameters up or down by one standard deviation, and looking at how the yields and distribution shapes change.

Luminosity

The luminosity measurement has one of the main uncertainties and is often grouped with the experimental uncertainties. The luminosity of the data sample collected by ATLAS is estimated through algorithms using data collected with the detector during nominal beam conditions, and is measured through independent forward detector systems placed next to the beam line outside the detector much further away from the collision point. The luminosity measurement is further calibrated through dedicated luminosity scans. Uncertainties are determined from the calibration methods, as detailed in the papers of 7 TeV and 8 TeV luminosity determination [109], [110]. For the integrated luminosity of 2015+2016 equal to 13.3 fb^{-1}, the uncertainty was 2.9% (Table 8.1, Line 1).

Pileup Uncertainty

This is estimated by varying the pileup parameter μ. This parameter is the average number of interactions per bunch crossing. It is strongly correlated to the number of vertices in an event. This number is estimated in MC, but as the pileup conditions are not known beforehand, and tend to change as a function of time, they must be corrected in MC to match the number in data. The upward variation on the pileup parameter, equivalent to not applying any correction, is highly correlated with a downward fluctuation of luminosity, and the downward variation is highly correlated to an upward fluctuation of luminosity. These uncertainties are on the order of 9%. The variations of $\pm 1\sigma$ in the pileup reweighting of MC is included to cover the uncertainty on the ratio between the predicted and measured inelastic cross-section [111] (Table 8.1, Line 4).

Jets

Uncertainties from jets come from three main sources: the jet energy scale, the jet energy resolution, and the jet vertex tagging. Further uncertainties arise when jets are tagged as coming from a particular flavour of quark. The impact of the jet uncertainties was assessed by varying each parameter $\pm 1\sigma$ and redoing the full analysis.

Jet energy scale uncertainties refer to uncertainties on the energy response of the calorimeter to jets of particles. There are many dedicated studies of this uncertainty, as it dominates the uncertainties for many important hadronic measurements [112], [113]. However, as this analysis is not strongly sensitive to hadronic energy scale corrections, a reduced number of parameters was used for the uncertainty calculation (Table 8.1, Lines 5, 16, 18, 28).

The jet energy resolution uncertainty is measured by using jets calibrated through the jet energy scale calibrations using two different algorithms in data and seeing how big the difference is in the measured resolution. The difference between the two methods is a measure of the uncertainty on the jet energy resolution [114]. The systematics can be grouped by parameters, and the simplest grouping was chosen for this analysis, as it is not heavily dependent on jets (Table 8.1, Line 15).

Uncertainty on jet vertex tagging impacts various aspects of the analysis, including flavour tagging, as well as pileup determination through number of vertices reconstruction. The uncertainty is estimated from an estimation of the residual contamination from pileup jets after pileup suppression [115] (Table 8.1, Line 6).

Finally, the flavour tagging is done using a multi-variate analysis, whose uncertainties are propagated to determine the uncertainties on the objects that are flavour tagged, which are b-quark jets in this analysis [99], [98] (Table 8.1, Lines 9, 10, 11, 14, 23).

Missing Transverse Energy

These uncertainties originate from ambiguity in how the soft terms are dealt with. These uncertainties are broken into resolution parallel and perpendicular to the vector sum of the hard scatter and the scale uncertainty parallel to it [116] (Table 8.1, Lines 19, 22). The impact of the $E_{\mathrm{T}}^{\mathrm{miss}}$ uncertainties was assessed by varying each parameter $\pm 1\sigma$ and redoing the full analysis.

Electrons

The uncertainties on the electrons arise from the scale factors applied on the energy scale and resolution [93] (Table 8.1, Lines 21, 29). They also arise from the efficiencies of the isolation, the ID, and the reconstruction [94] (Lines 2, 8, 13). The recommended variations are made on each of these parameters in turn, and the effect on the analysis is measured. Simplified lists of systematics are used, as this analysis does not use angular categorization. The impact of the electron uncertainties was assessed by varying each parameter $\pm 1\sigma$ and redoing the full analysis.

Muons

The uncertainties on the muons come from position reconstruction corrections applied to both the ID and MS [95] (Table 8.1, Lines 25, 30) and the momentum scale corrections applied (Line 27). Further uncertainties arise from applied scale factors for both efficiency and isolation from statistical and systematic variations (Lines 3, 17, 24, 26). The impact of the muon uncertainties was assessed by varying each parameter $\pm 1\sigma$ in turn and redoing the full analysis.

8.3 Effect of Errors on Significance and Discovery

The degree to which the bounds can be placed or the certainty that a discovery has been made depends not only on the properties of the proposed models for dark matter, but also on how well they can be measured. Therefore, a crucial component to estimate is the effect of systematic uncertainties on the measurement in data.

As can be seen in Table 8.1, each of the systematics listed above has a different effect on the signal. This is shown for a single model, with $m_{\text{med}} = 300$ GeV and $m_{\chi} = 50$ GeV. The variation of the systematic has an effect on the total yield, or number of events. In many cases, the systematic variations on the shape of the $E_{\text{T}}^{\text{miss}}$ are also accounted for. Both yield and shape systematics are evaluated for each signal models, and for the backgrounds that are estimated through MC simulation. The systematic uncertainties for the backgrounds estimated from data were explained in Chapter 7.

Uncertainty in signal regions		ee	$\mu\mu$
Total scaled signal events		48.57	51.50
Total statistical ($\sqrt{N_{\text{exp}}}$) uncertainty		±6.97	±7.18
Total systematic uncertainty		±2.77	±2.77
[systematic uncertainty in %]		[5.70%]	[5.38%]
1	Lumi	±1.41	±1.49
2	EL_EFF_ID_TOTAL_1NPCOR_PLUS_UNCOR	±1.26	±0.00
3	MUON_EFF_SYS	±0.00	±1.15
4	PRW_DATASF	±1.00	±0.90
5	JET_GroupedNP_1	±0.84	±0.94
6	JvtEfficiency	±0.84	±0.92
7	QCD	±0.59	±0.62
8	EL_EFF_Iso_TOTAL_1NPCOR_PLUS_UNCOR	±0.50	±0.00
9	FT_EFF_extrapolation	±0.42	±0.46
10	FT_EFF_extrapolation_from_Charm	±0.42	±0.46
11	FT_EFF_B_systematics	±0.00	±0.46
12	PDFIntra	±0.44	±0.25
13	EL_EFF_Reco_TOTAL_1NPCOR_PLUS_UNCOR	±0.43	±0.00
14	FT_EFF_Light_systematics	±0.36	±0.41
15	JET_JER_SINGLE_NP	±0.24	±0.38
16	JET_GroupedNP_3	±0.31	±0.22
17	MUON_ISO_SYS	±0.00	±0.23
18	JET_GroupedNP_2	±0.16	±0.11
19	MET_SoftTrk_Reso	±0.12	±0.13
20	PDFShape	±0.12	±0.09
21	EG_RESOLUTION_ALL	±0.11	±0.00
22	MET_SoftTrk_Scale	±0.10	±0.06
23	FT_EFF_C_systematics	±0.04	±0.03
24	MUON_EFF_STAT	±0.00	±0.08
25	MUONS_ID	±0.00	±0.08
26	MUON_ISO_STAT	±0.00	±0.06
27	MUONS_Scale	±0.00	±0.03
28	JET_EtaIntercalibration_NonClosure	±0.02	±0.00
29	EG_SCALE_ALL	±0.01	±0.00
30	MUONS_MS	±0.00	±0.00

Table 8.1: Summary of systematic uncertainties on events considered for Mono-Z signal point with $m_{\text{med}} = 300$ GeV and $m_{\chi} = 50$ GeV. These are the systematic variations considered in ee and $\mu\mu$ channels. The total uncertainties in first row are calculated by summing up all variations from different term quadratically.

Chapter 9

Results

Now all the pieces are in place: the signal samples have been modelled, the selections have been made, and the backgrounds and all of the uncertainties have been estimated, and the data have been analyzed. In order to make an interpretation of the measurement in data, the distributions of missing energy will now be compared to the Standard Model predictions. Distributions of the $E_{\mathrm{T}}^{\mathrm{miss}}$ using data taken in 2015+2016, a total integrated luminosity of 13.3 fb^{-1}, can be seen in Figure 9.1. This figure shows the data events represented as black points with statistical error bars, overlaid on the sum of the background processes. The backgrounds are stacked on top of each other so that the full stack represents the total SM predicted background. The statistical error of the total background contribution is shown as a shaded area. As can be seen, there are fluctuations on the observed data above the prediction, but it is not statistically significant, as will be quantified further in this chapter.

9.1 Background-Only ZZ Prediction

If there were no physics beyond the SM in this final state, at this centre-of-mass energy, and with the amount of integrated luminosity, then this analysis could be used to measure the cross section of the SM ZZ process. The acceptance can be estimated from Monte Carlo simulation of the ZZ background. The scaled starting number of events (for MC sample 361604 $ZZ \to \ell^+\ell^-\bar{\nu}\nu$ in the HIGG2D1 derivation) is 935.9, and the final number of events is 6.8. The sample has a filter efficiency of 1.00, from the Table in 5.1, equating, after all applied cuts, to an acceptance of $(0.73 \pm 0.05)\%$ in the ee channel. The error is obtained from Table 7.17 from adding

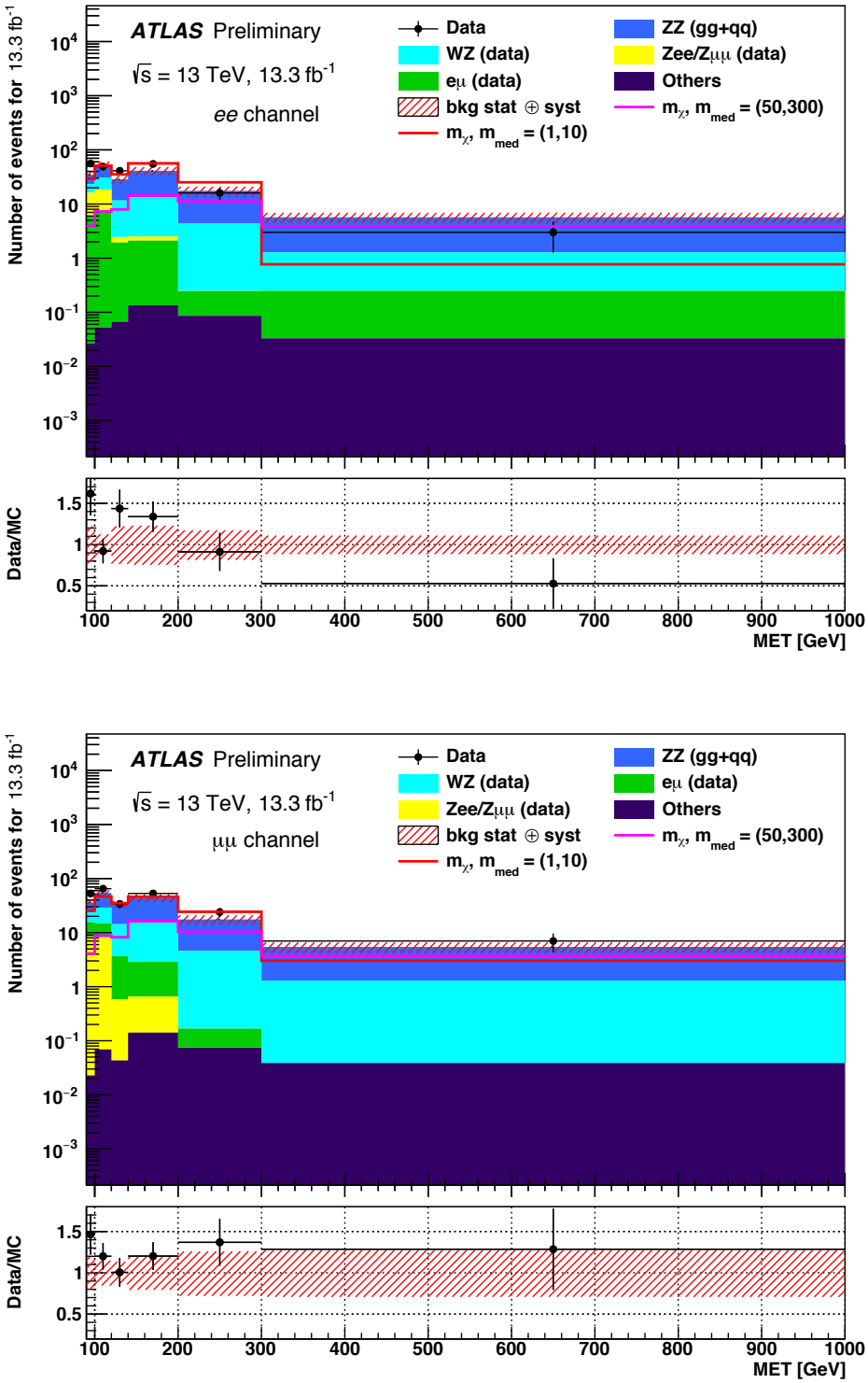

Figure 9.1: $E_{\mathrm{T}}^{\mathrm{miss}}$ distributions in the final signal regions of ee (top) and $\mu\mu$ (bottom). The background stack includes all of the backgrounds, estimated with data where possible, and 13.3 fb^{-1} of data collected in 2015+2016. Two signal samples are shown with coloured lines with their masses given in GeV.

in quadrature both the statistical and systematic error. For the $\mu\mu$ channel, this gives $(0.78 \pm 0.07)\%$.

From Equations 3.4 and 6.1, the cross section σ_{ZZ} is estimated in the ee-channel as $\sigma_{ZZ}(ee) = \sigma_{ZZ} \times Br(Z \to \nu\nu, Z \to e^+e^-)$ and in the $\mu\mu$-channel as $\sigma_{ZZ}(\mu\mu) = \sigma_{ZZ} \times Br(Z \to \nu\nu, Z \to \mu\mu)$. The calculation for each of these channels can be seen in Equation 9.1.

$$
\begin{array}{c|c}
ee & \mu\mu \\
\hline
\sigma_{ZZ} \times Br(Z \to \nu\nu, Z \to e^+e^-) & \sigma_{ZZ} \times Br(Z \to \nu\nu, Z \to \mu\mu) \\
= \dfrac{\left(N_{\text{signal},ee} - N_{\text{background},ee}\right)}{\epsilon_{\text{tot},ee}\, A_{\text{MC},ee} \int \mathcal{L}\, dt} & = \dfrac{\left(N_{\text{signal},\mu\mu} - N_{\text{background},\mu\mu}\right)}{\epsilon_{\text{tot},\mu\mu}\, A_{\text{MC},\mu\mu} \int \mathcal{L}\, dt} \\
= \dfrac{\big((220 \pm 15) - (84 \pm 16)\big)}{(0.0073 \pm 0.0005) \times (13.3 \pm 0.04)\,\text{fb}^{-1}} & = \dfrac{\big((236 \pm 15) - (89 \pm 11)\big)}{(0.0078 \pm 0.0007) \times (13.3 \pm 0.04)\,\text{fb}^{-1}} \\
\hline
= 1310 \pm 230\,\text{fb} & = 1420 \pm 220\,\text{fb}
\end{array}
\tag{9.1}
$$

The $qqZZ$ sample 361604 has two associated cross section values from different methods of calculation with values of 924.98 fb and 917.95 fb. Taking the average, and using the difference as an estimate of the uncertainty, gives 921 ± 4 fb. The $ggZZ$ contribution has a cross section value of 34.58 fb, and scaling by the NLO k-factor gives 59$\pm$35 fb. To approximate the total ZZ cross section, the cross sections from the $ggZZ$ and $qqZZ$ contributions are added, giving 980 ± 35 fb predicted cross section. The observed cross section in data is higher than the value from the MC generation. The values are slightly outside the maximum combined errors on the prediction and measurement. However, the difference is less than one standard deviation, 1σ, from the error on the estimate. While 68% of measurements should lie within 1σ of the prediction, 32%, or almost one in every three experiments, should show a level of disagreement of this much or more.

This same measurement of the SM diboson process can be visualized as a comparison of the number of events predicted from the cross section through the distribution of $E_{\text{T}}^{\text{miss}}$ in the data. The sum of the backgrounds is subtracted from the data, and the background-subtracted data events are drawn on top of the ZZ predicted back-

ground as shown in Figure 9.2. The observation from data shows more events than a background-only hypothesis would predict from the MC simulation, though it does not appear significant. This result is consistent with the cross section measurement carried out above.

9.2 Limit Setting

The measurement, assuming only the SM, is consistent to within 1σ. The simulated samples from the dark matter model (vector mediated with vector couplings) to which the analysis is sensitive may be excluded.

Using the expected values for the background in the signal regions, and comparing to the observed data, the signal samples can be studied to see if it is more likely that the observed data come from the 'null hypothesis' – a hypothesis that postulates the observations are drawn from a distribution including only the background (a null result), or if they are more likely to come from the background plus signal hypothesis – one whose distribution is drawn from a combined background and signal distribution [106]. The vector model from Section 5.2.2 was used to find the limits. In Figure 9.3, it can be see that the observed limit rules out the vector dark matter model below $\approx$ 400 GeV at a 95% Confidence Level (CL), where the measurement was expected to exclude mass samples in the model up to $\approx$ 500 GeV.

Limits were set using Histfitter [118]. The shape of the $E_{\mathrm{T}}^{\mathrm{miss}}$ distributions for each background (from Figure 9.1) were input with their statistical and systematic uncertainties. Along with the expected background, the observed $E_{\mathrm{T}}^{\mathrm{miss}}$ distributions in data were input. Each signal point was tested using the CLs method [119], a frequentist method that uses the signal strength as the parameter of interest. If the signal point was ruled out at 95% CL or better, the point was excluded. Interpolation between the signal points is applied to draw an exclusion curve. In Figure 9.3, the expected exclusion curve is given by the dashed line, which is from a background-only hypothesis (without data observations). The one sigma error bands on this expected exclusion are given in green. The solid line represents the exclusion curve from a background-only hypothesis on the observations. The observed exclusion of models is not as strong as expected, as the number of observed events in data was higher than the prediction from the expected backgrounds. However, the excess in number of events is within 1σ, meaning this is not statistically significant and cannot be claimed as a discovery. It is also consistent with the SM prediction of the ZZ

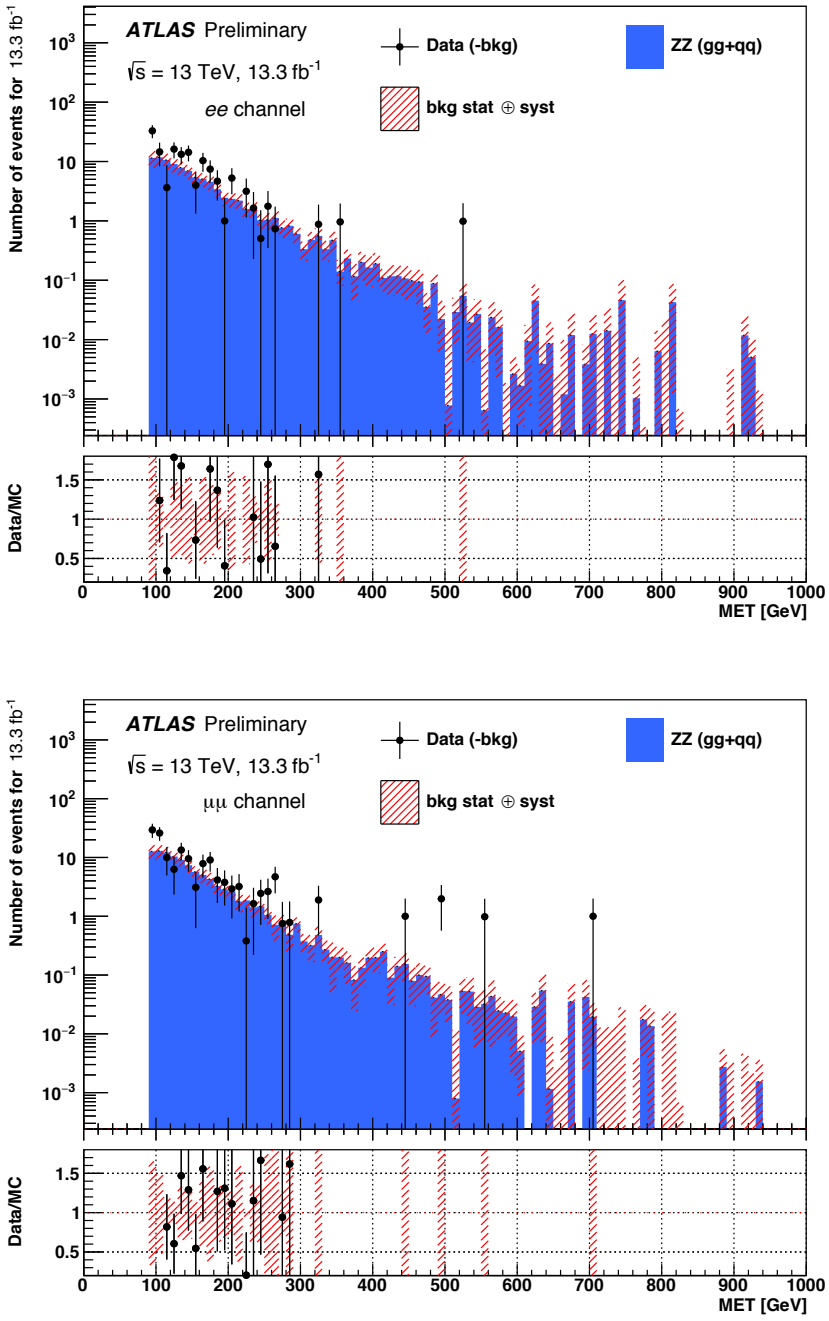

Figure 9.2: ZZ background estimated with MC vs observed in data in the (top) ee- and (bottom) $\mu\mu$-channels. The distributions are shown after all selection requirements are applied in the cutflow, in the final signal region. The data distribution has all other backgrounds subtracted, using data-driven estimates where available. Statistical and systematic uncertainties are shown in the error band.

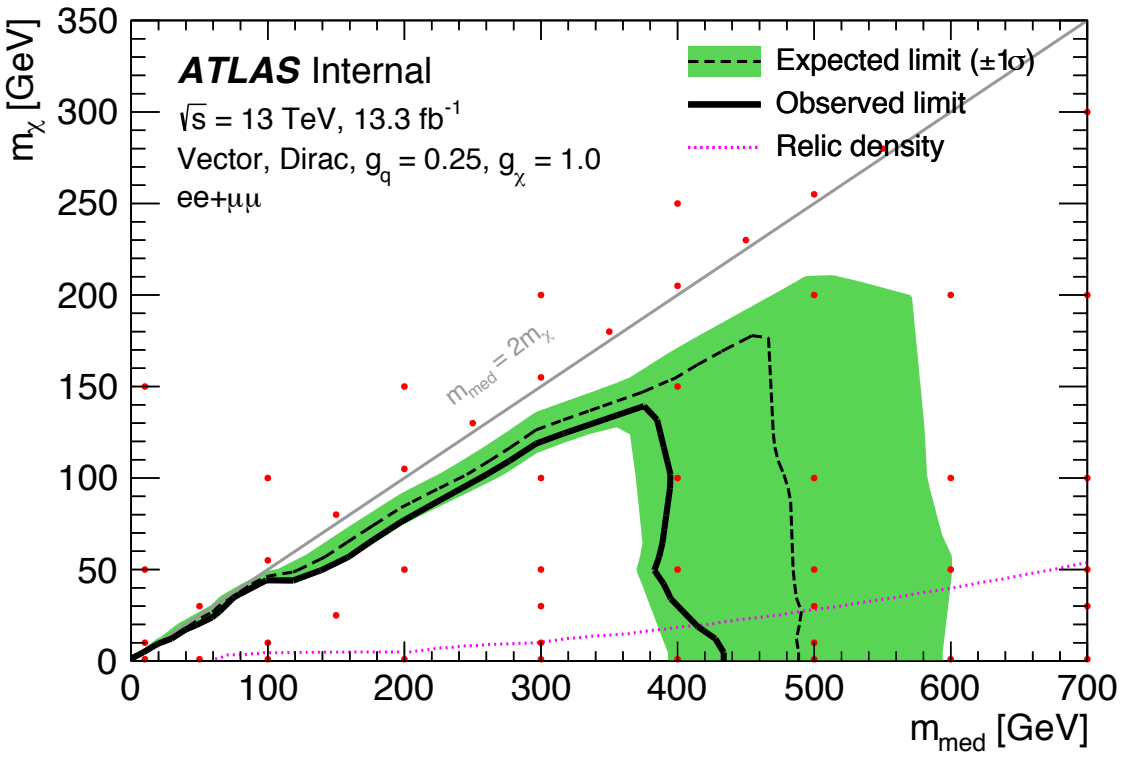

Figure 9.3: Expected and observed 95% CL limits for the vector mediated, vector coupling model of the Mono-Z dark matter signals. The 'on-shell' line, where $m_{\text{med}} = 2m_{\chi}$, is indicated in grey. The red points indicate the simulated DM samples. The dotted magenta curve corresponds to the parameters where the correct DM relic abundance is obtained from standard thermal freeze-out for the chosen couplings [117]. DM is overproduced to the bottom-right of the curve.

diboson background in the previous section.

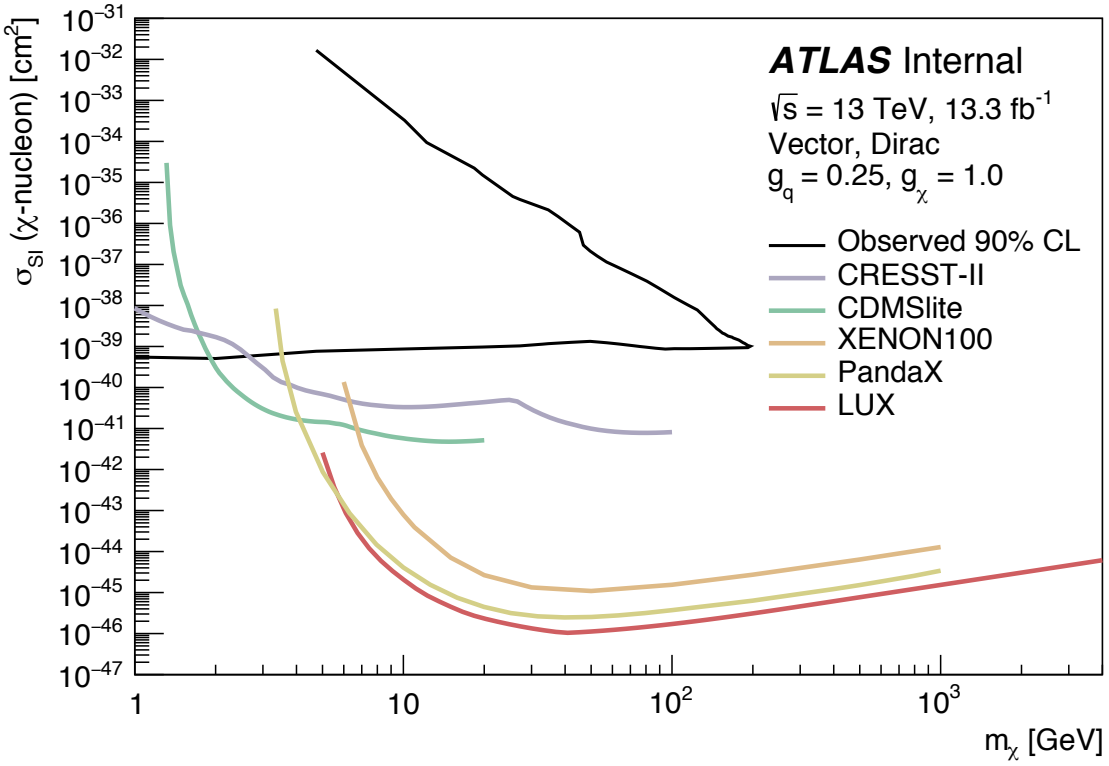

Figure 9.4: The dark matter vector observed 90% CL limit reinterpreted as a spin independent nucleon-scattering limit and compared to various direct detection experimental search results at 90% CL.

The limits calculated for the null hypothesis were recalculated at a 90% CL, and reinterpreted as cross section-m_χ limits. These are then compared with direct detection searches, as seen in Figure 9.4. The model that includes a vector mediator would lead to a spin-independent interaction with a nucleon. For spin-independent interactions, the assumption is made that the DM-nucleon cross section for interaction, σ_{SI}, is equivalent for both protons and neutrons.

From [117], the DM-nucleon cross section is given by

$$\sigma_{\text{SI}} = \frac{f^2(g_q) g_\chi^2 \mu_{n\chi}^2}{\pi m_{\text{med}}^4}, \tag{9.2}$$

where $f(g_q) = 3g_q$ is the mediator-nucleon coupling, as a function of the mediator-quark coupling g_q for the vector mediator; g_χ is the DM-mediator coupling; m_{med} is the mass of the mediator; and $\mu_{n\chi} = m_n m_\chi/(m_n + m_\chi)$ is the DM-nucleon reduced

mass. With a choice of convenient variables (and using the values of $g_q = 0.25$ and $g_\chi = 1$) this works out to be

$$\sigma_{\mathrm{SI}} \simeq 6.9 \times 10^{-41}\mathrm{cm}^2 \left(\frac{\mu_{n\chi}}{1\ \mathrm{GeV}}\right)^2 \left(\frac{1\ \mathrm{TeV}}{m_{\mathrm{med}}}\right)^4. \tag{9.3}$$

The comparison to the direct detection limits is made using this equation. This is valid for a set of assumptions. Two of the most important ones are that the SM quarks all couple equally to the mediator, and that there is a single variant of Dirac DM in the universe that the direct detection searches are able to probe. Given these, it can be seen that the LHC is more sensitive than the SI direct detection experiments for the lightest dark matter particles in the vector mediator simplified dark matter models, but direct detection searches are still the best method at finding this model of dark matter at intermediate to high masses. The two approaches are highly complementary.

9.3 Future Prospects

As no discoveries are being made with the first large dataset from the LHC, the models that are used to search for new physics are being considered more carefully. Effort is being put into making the models more physically motivated, with theories that are valid in terms of gauge invariance and perturbative unitarity. These models, to which we may have less sensitivity, are nevertheless more likely to describe nature, and must be searched out.

A dark matter discovery is unlikely to happen in isolation. If it is detected in a collider experiment, it may be visible in a direct detection experiment, and could be found in an indirect detection experiment as well. Similarly, if it is seen in one of the other two sets of experiments, it should be observable at the LHC. There is complementarity between the searches but there is also a capacity to cross-check. Moreover, we need to be mindful of the limits already set by different experiments, and understand the sensitivity of the LHC to set comparable limits.

The nature of dark matter is still unknown. The most exciting part is that no one knows where the first evidence of the particle nature of dark matter will appear.

Bibliography

[1] ATLAS Collaboration, G. Aad et al., *Observation of a new particle in the search for the Standard Model Higgs boson with the ATLAS detector at the LHC*, Phys. Lett. **B716** (2012) 1–29, arXiv:1207.7214 [hep-ex]. (Cited on page 1.)

[2] G. Bertone, D. Hooper, and J. Silk, *Particle Dark Matter: Evidence, Candidates and Constraints*, Physics Reports **405** (2005) 279 – 390. (Cited on pages 1 and 2.)

[3] J. L. Feng, *Dark Matter Candidates from Particle Physics and Methods of Detection*, Ann. Rev. Astron. Astrophys. **48** (2010) 495–545, arXiv:1003.0904 [astro-ph.CO]. (Cited on pages 1 and 5.)

[4] L. Bergström, *Nonbaryonic dark matter: Observational evidence and detection methods*, Rept. Prog. Phys. **63** (2000) 793, arXiv:hep-ph/0002126 [hep-ph]. (Cited on pages 1 and 3.)

[5] F. Zwicky, *Republication of: The redshift of extragalactic nebulae*, General Relativity and Gravitation **41** (2009) 207–224. (Cited on pages 1 and 3.)

[6] Particle Data Group Collaboration, C. Patrignani et al., *Review of Particle Physics*, Chin. Phys. **C40** (2016) 100001. (Cited on pages 1, 3, 4, 11, 22, and 30.)

[7] L. Evans and P. Bryant, *LHC Machine*, Journal of Instrumentation **3** (2008) S08001. (Cited on pages 1 and 2.)

[8] ATLAS Collaboration, G. Aad et al., *The ATLAS Experiment at the CERN Large Hadron Collider*, JINST **3** (2008) S08003. (Cited on pages 1, 29, 30, 32, and 33.)

[9] J. Abdallah, H. Araujo, A. Arbey, et al., *Simplified models for dark matter searches at the LHC*, Physics of the Dark Universe **9–10** (2015) 8 – 23. (Cited on pages 2 and 26.)

[10] P. Scott, *Searches for Particle Dark Matter: Dark stars, dark galaxies, dark halos and global supersymmetric fits*. PhD thesis, Stockholm University, 2010. (Cited on pages 2, 4, and 5.)

[11] L. Bergström, *Dark Matter Candidates*, New Journal of Physics **11** (2009) 105006. (Cited on page 2.)

[12] J. A. Tyson, G. P. Kochanski, and I. P. Dell'Antonio, *Detailed mass map of CL0024+1654 from strong lensing*, Astrophys. J. **498** (1998) L107, `arXiv:astro-ph/9801193 [astro-ph]`. (Cited on page 3.)

[13] D. Clowe, M. Bradac, A. H. Gonzalez, M. Markevitch, S. W. Randall, C. Jones, and D. Zaritsky, *A direct empirical proof of the existence of dark matter*, Astrophys. J. **648** (2006) L109–L113, `arXiv:astro-ph/0608407 [astro-ph]`. (Cited on page 3.)

[14] R. Massey et al., *Dark matter maps reveal cosmic scaffolding*, Nature **445** (2007) 286, `arXiv:astro-ph/0701594 [astro-ph]`. (Cited on page 3.)

[15] Supernova Cosmology Project Collaboration, M. Kowalski et al., *Improved Cosmological Constraints from New, Old and Combined Supernova Datasets*, Astrophys. J. **686** (2008) 749–778, `arXiv:0804.4142 [astro-ph]`. (Cited on page 4.)

[16] F. Iocco, G. Mangano, G. Miele, O. Pisanti, and P. D. Serpico, *Primordial nucleosynthesis: From precision cosmology to fundamental physics*, Physics Reports **472** (2009) 1 – 76. (Cited on page 4.)

[17] W. J. Percival, S. Cole, D. J. Eisenstein, R. C. Nichol, J. A. Peacock, A. C. Pope, and A. S. Szalay, *Measuring the Baryon Acoustic Oscillation scale using the Sloan Digital Sky Survey and 2dF Galaxy Redshift Survey*, Monthly Notices of the Royal Astronomical Society **381** (2007) 1053, `arXiv:0705.3323`. (Cited on page 4.)

[18] G. Jungman, M. Kamionkowski, and K. Griest, *Supersymmetric dark matter*, Physics Reports **267** (1996) 195 – 373. (Cited on page 4.)

[19] SNO Collaboration, Q. R. Ahmad et al., *Measurement of the rate of $\nu_e + d \to p + p + e^-$ interactions produced by ^8B solar neutrinos at the Sudbury Neutrino Observatory*, Phys. Rev. Lett. **87** (2001) 071301, arXiv:nucl-ex/0106015 [nucl-ex]. (Cited on page 4.)

[20] J. Goodman, M. Ibe, A. Rajaraman, W. Shepherd, T. M. P. Tait, and H.-B. Yu, *Constraints on Dark Matter from Colliders*, Phys. Rev. **D82** (2010) 116010, arXiv:1008.1783 [hep-ph]. (Cited on page 5.)

[21] J. Goodman, M. Ibe, A. Rajaraman, W. Shepherd, T. M. P. Tait, and H.-B. Yu, *Constraints on Light Majorana dark Matter from Colliders*, Phys. Lett. **B695** (2011) 185–188, arXiv:1005.1286 [hep-ph]. (Cited on pages 5, 23, and 24.)

[22] P. J. Fox, R. Harnik, J. Kopp, and Y. Tsai, *LEP Shines Light on Dark Matter*, Physical Review D **84** (2011) 014028. (Cited on page 5.)

[23] LUX Collaboration, D. S. Akerib et al., *Limits on spin-dependent WIMP-nucleon cross section obtained from the complete LUX exposure*, arXiv:1705.03380 [astro-ph.CO]. (Cited on page 6.)

[24] XENON100 Collaboration, E. Aprile et al., *Dark Matter Results from 225 Live Days of XENON100 Data*, Phys. Rev. Lett. **109** (2012) 181301, arXiv:1207.5988 [astro-ph.CO]. (Cited on page 6.)

[25] PandaX-II Collaboration, A. Tan et al., *Dark Matter Results from First 98.7 Days of Data from the PandaX-II Experiment*, Phys. Rev. Lett. **117** (2016) 121303, arXiv:1607.07400 [hep-ex]. (Cited on page 6.)

[26] J. Schieck et al., *Direct Dark Matter Search with the CRESST II Experiment*, PoS **ICHEP2016** (2016) 217, arXiv:1611.02113 [astro-ph.CO]. (Cited on page 6.)

[27] SuperCDMS Collaboration, R. Agnese et al., *Search for Low-Mass Weakly Interacting Massive Particles with SuperCDMS*, Phys. Rev. Lett. **112** (2014) 241302, arXiv:1402.7137 [hep-ex]. (Cited on page 6.)

[28] M. Kuźniak, *DEAP-3600 Dark Matter Search*, Nuclear and Particle Physics Proceedings **273** (2016) 340 – 346, 37th International Conference on High Energy Physics (ICHEP). (Cited on page 6.)

[29] C. E. Aalseth et al., *DarkSide-20k: A 20 Tonne Two-Phase LAr TPC for Direct Dark Matter Detection at LNGS*, arXiv:1707.08145 [physics.ins-det]. (Cited on page 6.)

[30] PICO Collaboration, C. Amole et al., *Improved dark matter search results from PICO-2L Run 2*, Phys. Rev. **D93** (2016) 061101, arXiv:1601.03729 [astro-ph.CO]. (Cited on page 6.)

[31] E. Tempel, A. Hektor, and M. Raidal, *Fermi 130 GeV gamma-ray excess and dark matter annihilation in sub-haloes and in the Galactic centre*, JCAP **1209** (2012) 032, arXiv:1205.1045 [hep-ph], [Addendum: JCAP1211,A01(2012)]. (Cited on page 6.)

[32] AMS Collaboration, M. Aguilar et al., *First Result from the Alpha Magnetic Spectrometer on the International Space Station: Precision Measurement of the Positron Fraction in Primary Cosmic Rays of 0.5-350 GeV*, Phys. Rev. Lett. **110** (2013) 141102. (Cited on page 6.)

[33] PAMELA Collaboration, O. Adriani et al., *An anomalous positron abundance in cosmic rays with energies 1.5-100 GeV*, Nature **458** (2009) 607–609, arXiv:0810.4995 [astro-ph]. (Cited on page 6.)

[34] S. L. Glashow, *Partial Symmetries of Weak Interactions*, Nucl. Phys. **22** (1961) 579–588. (Cited on pages 9 and 12.)

[35] S. Weinberg, *A Model of Leptons*, Phys. Rev. Lett. **19** (1967) 1264–1266. (Cited on pages 9 and 12.)

[36] A. Salam, *Weak and Electromagnetic Interactions*, Conf. Proc. **C680519** (1968) 367–377. (Cited on pages 9 and 12.)

[37] D. H. Perkins, *Introduction to High Energy Physics*. Cambridge University Press, 4th ed., 2000. (Cited on pages 9 and 21.)

[38] I. J. R. Aitchison and A. J. G. Hey, *Gauge Theories in Particle Physics*. IOP Publishing Ltd, 2nd ed., 1989. (Cited on page 9.)

[39] D. Griffiths, *Introduction to Elementary Particles*. Wiley-VCH, 2nd ed., 2008. (Cited on pages 9 and 19.)

[40] P. Higgs, *Broken symmetries, massless particles and gauge fields*, Physics Letters **12** (1964) 132 – 133. (Cited on page 9.)

[41] ATLAS Collaboration, *Observation of a new particle in the search for the Standard Model Higgs boson with the ATLAS detector at the LHC*, Physics Letters B **716** (2012) 1 – 29. (Cited on page 9.)

[42] CMS Collaboration, *Observation of a new boson at a mass of 125 GeV with the CMS experiment at the LHC*, Physics Letters B **716** (2012) 30 – 61. (Cited on page 9.)

[43] A. Purcell, *Go on a particle quest at the first CERN webfest. Le premier webfest du CERN se lance à la conqutê des particules*, `https://cds.cern.ch/record/1473657`. (Cited on page 10.)

[44] T2K Collaboration, K. Abe et al., *Upper bound on neutrino mass based on T2K neutrino timing measurements*, Phys. Rev. **D93** (2016) 012006, `arXiv:1502.06605 [hep-ex]`. (Cited on page 15.)

[45] R. P. Feynman, *Very high-energy collisions of hadrons*, Phys. Rev. Lett. **23** (1969) 1415–1417. (Cited on page 15.)

[46] L. A. Harland-Lang, A. D. Martin, P. Motylinski, and R. S. Thorne, *Parton distributions in the LHC era: MMHT 2014 PDFs*, Eur. Phys. J. **C75** (2015) 204, `arXiv:1412.3989 [hep-ph]`. (Cited on page 16.)

[47] G. Altarelli and G. Parisi, *Asymptotic Freedom in Parton Language*, Nucl. Phys. **B126** (1977) 298–318. (Cited on page 16.)

[48] Y. L. Dokshitzer, *Calculation of the Structure Functions for Deep Inelastic Scattering and e+ e- Annihilation by Perturbation Theory in Quantum Chromodynamics.*, Sov. Phys. JETP **46** (1977) 641–653, [Zh. Eksp. Teor. Fiz.73,1216(1977)]. (Cited on page 16.)

[49] V. N. Gribov and L. N. Lipatov, *Deep inelastic e p scattering in perturbation theory*, Sov. J. Nucl. Phys. **15** (1972) 438–450, [Yad. Fiz.15,781(1972)]. (Cited on page 16.)

[50] J. M. Campbell, J. Huston, and W. Stirling, *Hard interactions of quarks and gluons: a primer for LHC physics*, Reports on Progress in Physics **70** (2006) 89. (Cited on page 17.)

[51] O. S. Brüning, P. Collier, P. Lebrun, S. Myers, R. Ostojic, J. Poole, and P. Proudlock, *LHC Design Report*. CERN Yellow Reports: Monographs. CERN, Geneva, 2004. `https://cds.cern.ch/record/782076`. (Cited on page 18.)

[52] P. D. Group, J. Beringer, J.-F. Arguin, R. Barnett, K. Copic, O. Dahl, D. Groom, C.-J. Lin, J. Lys, H. Murayama, C. Wohl, et al., *The Review of Particle Physics*, Physical Review D **86** (2012) 010001. (Cited on page 20.)

[53] OPAL Collaboration, G. Abbiendi et al., *Precise determination of the Z resonance parameters at LEP: 'Zedometry'*, Eur. Phys. J. **C19** (2001) 587–651, `arXiv:hep-ex/0012018 [hep-ex]`. (Cited on page 20.)

[54] The ALEPH Collaboration; The DELPHI Collaboration; The L3 Collaboration; The OPAL Collaboration; The SLD Collaboration; The LEP Electroweak Working Group; The SLD Electroweak and Heavy Flavour Groups, *Precision electroweak measurements on the Z resonance*, Physics Reports **427** (2006) 257 – 454. (Cited on page 20.)

[55] C. Burgess, *An Introduction to Effective Field Theory*, Annual Review of Nuclear and Particle Science **57** (2007) 329–362. (Cited on page 22.)

[56] M. Beltran, D. Hooper, E. W. Kolb, Z. A. Krusberg, and T. M. Tait, *Maverick Dark Matter at Colliders*, Journal of High Energy Physics **2010** (2010) 1–17. (Cited on page 23.)

[57] P. Ciafaloni, M. Cirelli, D. Comelli, A. De Simone, A. Riotto, and A. Urbano, *On the Importance of Electroweak Corrections for Majorana Dark Matter Indirect Detection*, Journal of Cosmology and Astroparticle Physics **2011** (2011) 018. (Cited on page 24.)

[58] P. Ciafaloni, D. Comelli, A. De Simone, A. Riotto, and A. Urbano, *Electroweak bremsstrahlung for wino-like Dark Matter annihilations*, Journal of Cosmology and Astroparticle Physics **2012** (2012) 016. (Cited on page 24.)

[59] L. Bergström, *Radiative Processes in Dark Matter Photino Annihilation*, Physics Letters B **225** (1989) 372–380. (Cited on page 24.)

[60] ATLAS Collaboration, *Search for dark matter in events with a Z boson and missing transverse momentum in pp collisions at* $\sqrt{s} = 8$ TeV *with the ATLAS detector*, Physical Review D **90** (2014) 012004. (Cited on page 25.)

[61] G. Busoni, A. D. Simone, E. Morgante, and A. Riotto, *On the validity of the effective field theory for dark matter searches at the LHC*, Physics Letters B **728** (2014) 412 – 421. (Cited on page 25.)

[62] J. Abdallah et al., *Simplified Models for Dark Matter and Missing Energy Searches at the LHC*, `arXiv:1409.2893 [hep-ph]`. (Cited on page 25.)

[63] CMS Collaboration, S. Chatrchyan et al., *The CMS Experiment at the CERN LHC*, JINST **3** (2008) S08004. (Cited on page 28.)

[64] LHCb Collaboration, A. A. Alves, Jr. et al., *The LHCb Detector at the LHC*, JINST **3** (2008) S08005. (Cited on page 28.)

[65] ALICE Collaboration, K. Aamodt et al., *The ALICE experiment at the CERN LHC*, JINST **3** (2008) S08002. (Cited on page 28.)

[66] P. Mouche, *Overall view of the LHC. Vue d'ensemble du LHC*, `http://cds.cern.ch/record/1708847`, General Photo. (Cited on page 29.)

[67] ATLAS Collaboration, *ATLAS inner detector: Technical Design Report, 1*. Technical Design Report ATLAS. CERN, Geneva, 1997. `https://cds.cern.ch/record/331063`. (Cited on page 30.)

[68] ATLAS Collaboration, N. Wermes and G. Hallewel, *ATLAS pixel detector: Technical Design Report*. Technical Design Report ATLAS. CERN, Geneva, 1998. `https://cds.cern.ch/record/381263`. (Cited on page 30.)

[69] M. Capeans, G. Darbo, K. Einsweiller, M. Elsing, T. Flick, M. Garcia-Sciveres, C. Gemme, H. Pernegger, O. Rohne, and R. Vuillermet, *ATLAS Insertable B-Layer Technical Design Report*, Tech. Rep. CERN-LHCC-2010-013. ATLAS-TDR-19, CERN, Sep, 2010. `https://cds.cern.ch/record/1291633`. (Cited on page 30.)

[70] ATLAS SCT Collaboration, Y. Unno, *ATLAS silicon microstrip semiconductor tracker (SCT)*, Nucl. Instrum. Meth. **A453** (2000) 109–120. (Cited on page 30.)

[71] ATLAS TRT Collaboration, E. Abat et al., *The ATLAS Transition Radiation Tracker (TRT) proportional drift tube: Design and performance*, JINST **3** (2008) P02013. (Cited on page 30.)

[72] J. Pequenao, *Computer generated image of the whole ATLAS detector*, 2008. (Cited on page 31.)

[73] ATLAS Collaboration, *ATLAS liquid argon calorimeter: Technical design report*, `https://cds.cern.ch/record/331061`. (Cited on page 30.)

[74] W. Lampl, S. Laplace, D. Lelas, P. Loch, H. Ma, S. Menke, S. Rajagopalan, D. Rousseau, S. Snyder, and G. Unal, *Calorimeter Clustering Algorithms: Description and Performance*,. (Cited on page 30.)

[75] A. Artamonov et al., *The ATLAS forward calorimeters*, JINST **3** (2008) P02010. (Cited on page 31.)

[76] ATLAS Collaboration, *ATLAS tile calorimeter: Technical Design Report*. Technical Design Report ATLAS. CERN, Geneva, 1996. `https://cds.cern.ch/record/331062`. (Cited on page 32.)

[77] ATLAS Collaboration, *Performance of the ATLAS hadronic end-cap calorimeter in beam tests*, Nuclear Instruments and Methods in Physics Research Section A: Accelerators, Spectrometers, Detectors and Associated Equipment **482** (2002) 94 – 124. (Cited on page 32.)

[78] ATLAS Collaboration, G. Aad et al., *Jet energy resolution in proton-proton collisions at $\sqrt{s} = 7$ TeV recorded in 2010 with the ATLAS detector*, Eur. Phys. J. **C73** (2013) 2306, `arXiv:1210.6210 [hep-ex]`. (Cited on pages 32 and 57.)

[79] ATLAS Collaboration, *ATLAS muon spectrometer: Technical Design Report*. Technical Design Report ATLAS. CERN, Geneva, 1997. `https://cds.cern.ch/record/331068`. (Cited on page 32.)

[80] R. Achenbach et al., *The ATLAS level-1 calorimeter trigger*, JINST **3** (2008) P03001. (Cited on page 33.)

[81] F. Anulli, G. Ciapetti, D. De Pedis, et al., *The Level-1 Trigger Muon Barrel System of the ATLAS experiment at CERN. The Level-1 Trigger barrel System of the ATLAS Experiment at CERN*, JINST **4** (2009) P04010. 37 p, `http://cds.cern.ch/record/1154759`. (Cited on page 33.)

[82] ATLAS Collaboration, P. Jenni, M. Nessi, M. Nordberg, and K. Smith, *ATLAS high-level trigger, data-acquisition and controls: Technical Design Report*. Technical Design Report ATLAS. CERN, Geneva, 2003. `https://cds.cern.ch/record/616089`. (Cited on page 33.)

[83] Y. Nakahama, *The ATLAS Trigger System: Ready for Run-2*, J. Phys. Conf. Ser. **664** (2015) 082037. (Cited on page 33.)

[84] ATLAS Collaboration, ATLAS Collaboration, *Technical Design Report for the Phase-I Upgrade of the ATLAS TDAQ System*,. (Cited on page 33.)

[85] A. Achilli, Y. Srivastava, R. Godbole, A. Grau, G. Pancheri, and O. Shekhovtsova, *Total and inelastic cross-sections at LHC at* $\sqrt{s} = 7$ *TeV and beyond*, Physical Review D **84** (2011) 094009. (Cited on page 35.)

[86] J. Alwall, R. Frederix, S. Frixione, V. Hirschi, F. Maltoni, O. Mattelaer, H.-S. Shao, T. Stelzer, P. Torrielli, and M. Zaro, *The automated computation of tree-level and next-to-leading order differential cross sections, and their matching to parton shower simulations*, Journal of High Energy Physics **2014** (2014) 1–157. (Cited on page 37.)

[87] T. Gleisberg et al., *Event generation with SHERPA 1.1*, JHEP **02** (2009) 007, `arXiv:0811.4622 [hep-ph]`. (Cited on page 37.)

[88] S. Frixione, P. Nason, and C. Oleari, *Matching NLO QCD computations with Parton Shower simulations: the POWHEG method*, Journal of High Energy Physics **2007** (2007) 070. (Cited on page 37.)

[89] T. Sjöstrand, S. Mrenna, and P. Skands, *PYTHIA 6.4 Physics and Manual*, Journal of High Energy Physics **2006** (2006) 026. (Cited on page 37.)

[90] T. Sjöstrand, S. Ask, J. R. Christiansen, R. Corke, N. Desai, P. Ilten, S. Mrenna, S. Prestel, C. O. Rasmussen, and P. Z. Skands, *An Introduction to PYTHIA 8.2*, Computer physics communications **191** (2015) 159–177. (Cited on page 37.)

[91] S. Agostinelli, J. Allison, K. a. Amako, J. Apostolakis, H. Araujo, P. Arce, M. Asai, D. Axen, S. Banerjee, G. Barrand, et al., *GEANT4–a simulation toolkit*, Nuclear instruments and methods in physics research section A: Accelerators, Spectrometers, Detectors and Associated Equipment **506** (2003) 250–303. (Cited on page 37.)

[92] ATLAS Collaboration, *Electron reconstruction and identification efficiency measurements with the ATLAS detector using the 2011 LHC proton–proton collision data*, The European Physical Journal C **74** (2014) 1–38. (Cited on page 48.)

[93] ATLAS Collaboration, *Electron and photon energy calibration with the ATLAS detector using data collected in 2015 at* $\sqrt{s} = 13$ TeV, Tech. Rep. ATL-PHYS-PUB-2016-015, CERN, Geneva, Aug, 2016. `https://cds.cern.ch/record/2203514`. (Cited on pages 48 and 108.)

[94] ATLAS Collaboration, *Electron efficiency measurements with the ATLAS detector using the 2015 LHC proton-proton collision data*, Tech. Rep. ATLAS-CONF-2016-024, CERN, Geneva, Jun, 2016. `https://cds.cern.ch/record/2157687`. (Cited on pages 49 and 108.)

[95] ATLAS Collaboration, G. Aad et al., *Muon reconstruction performance of the ATLAS detector in proton-proton collision data at* $\sqrt{s}$ *=13 TeV*, Eur. Phys. J. **C76** (2016) 292, `arXiv:1603.05598 [hep-ex]`. (Cited on pages 52, 53, and 108.)

[96] M. Cacciari, G. P. Salam, and G. Soyez, *The anti-kt jet clustering algorithm*, Journal of High Energy Physics **2008** (2008) 063. (Cited on page 57.)

[97] ATLAS Collaboration, *Tagging and suppression of pileup jets with the ATLAS detector*, ATLAS-CONF-2014-018, 2014, `https://cds.cern.ch/record/1700870`. (Cited on page 58.)

[98] ATLAS Collaboration, *Optimisation of the ATLAS b-tagging performance for the 2016 LHC Run*, Tech. Rep. ATL-PHYS-PUB-2016-012, CERN, Geneva, Jun, 2016. http://cds.cern.ch/record/2160731. (Cited on pages 58 and 107.)

[99] ATLAS Collaboration, G. Aad et al., *Performance of b-Jet Identification in the ATLAS Experiment*, JINST **11** (2016) P04008, arXiv:1512.01094 [hep-ex]. (Cited on pages 58 and 107.)

[100] D. Adams, C. Anastopoulos, A. Andreazza, et al., *Recommendations of the Physics Objects and Analysis Harmonisation Study Groups 2014*, Tech. Rep. ATL-PHYS-INT-2014-018, CERN, Geneva, Jul, 2014. https://cds.cern.ch/record/1743654. (Cited on page 60.)

[101] ATLAS Collaboration, *Performance of missing transverse momentum reconstruction for the ATLAS detector in the first proton-proton collisions at at $\sqrt{s}$= 13 TeV*, Tech. Rep. ATL-PHYS-PUB-2015-027, CERN, Geneva, Jul, 2015. https://cds.cern.ch/record/2037904. (Cited on page 60.)

[102] ATLAS Collaboration, M. Aaboud et al., *Reconstruction of primary vertices at the ATLAS experiment in Run 1 proton-proton collisions at the LHC*, Eur. Phys. J. **C77** (2017) 332, arXiv:1611.10235 [physics.ins-det]. (Cited on page 61.)

[103] ATLAS Collaboration, *Vertex Reconstruction Performance of the ATLAS Detector at $\sqrt{s} = 13$ TeV*, Tech. Rep. ATL-PHYS-PUB-2015-026, CERN, Geneva, Jul, 2015. http://cds.cern.ch/record/2037717. (Cited on page 61.)

[104] ATLAS Collaboration, *Selection of jets produced in 13 TeV proton-proton collisions with the ATLAS detector*, Tech. Rep. ATLAS-CONF-2015-029, CERN, Geneva, Jul, 2015. http://cds.cern.ch/record/2037702. (Cited on page 61.)

[105] L. Eklund, C. Buttar, C. Grigson, G. Kramberger, I. Mandic, M. Mikuz, and P. Phillips, *SEU rate estimates for the ATLAS/SCT front-end ASIC*, Nucl. Instrum. Meth. **A515** (2003) 415–421. (Cited on page 63.)

[106] G. Cowan, K. Cranmer, E. Gross, and O. Vitells, *Asymptotic formulae for likelihood-based tests of new physics*, Eur. Phys. J. **C71** (2011) 1554, arXiv:1007.1727 [physics.data-an], [Erratum: Eur. Phys. J.C73,2501(2013)]. (Cited on pages 66 and 113.)

[107] ATLAS Collaboration, G. Aad et al., *Measurement of ZZ production in pp collisions at $\sqrt{s} = 7$ TeV and limits on anomalous ZZZ and $ZZ\gamma$ couplings with the ATLAS detector*, JHEP **03** (2013) 128, arXiv:1211.6096 [hep-ex]. (Cited on page 72.)

[108] Private communication with the ATLAS 'HZZ Group', *Theoretical Uncertainties Occurring In $H \to ZZ$ analyses*, Unpublished, 2015. (Cited on pages 72 and 75.)

[109] ATLAS Collaboration, G. Aad et al., *Improved luminosity determination in pp collisions at $\sqrt{s} = 7$ TeV using the ATLAS detector at the LHC*, Eur. Phys. J. **C73** (2013) 2518, arXiv:1302.4393 [hep-ex]. (Cited on page 106.)

[110] ATLAS Collaboration, M. Aaboud et al., *Luminosity determination in pp collisions at $\sqrt{s} = 8$ TeV using the ATLAS detector at the LHC*, Eur. Phys. J. **C76** (2016) 653, arXiv:1608.03953 [hep-ex]. (Cited on page 106.)

[111] ATLAS Collaboration, M. Aaboud et al., *Measurement of the Inelastic Proton-Proton Cross Section at $\sqrt{s} = 13$ TeV with the ATLAS Detector at the LHC*, Phys. Rev. Lett. **117** (2016) 182002, arXiv:1606.02625 [hep-ex]. (Cited on page 106.)

[112] ATLAS Collaboration, G. Aad et al., *Single hadron response measurement and calorimeter jet energy scale uncertainty with the ATLAS detector at the LHC*, Eur. Phys. J. **C73** (2013) 2305, arXiv:1203.1302 [hep-ex]. (Cited on page 107.)

[113] ATLAS Collaboration, *Jet Calibration and Systematic Uncertainties for Jets Reconstructed in the ATLAS Detector at $\sqrt{s} = 13$ TeV*, Tech. Rep. ATL-PHYS-PUB-2015-015, CERN, Geneva, Jul, 2015. http://cds.cern.ch/record/2037613. (Cited on page 107.)

[114] ATLAS Collaboration, M. Aaboud et al., *Jet energy scale measurements and their systematic uncertainties in proton-proton collisions at $\sqrt{s} = 13$ TeV with the ATLAS detector*, arXiv:1703.09665 [hep-ex]. (Cited on page 107.)

[115] ATLAS Collaboration, *Tagging and suppression of pileup jets with the ATLAS detector*, Tech. Rep. ATLAS-CONF-2014-018, CERN, Geneva, May, 2014. https://cds.cern.ch/record/1700870. (Cited on page 107.)

[116] ATLAS Collaboration, *Expected performance of missing transverse momentum reconstruction for the ATLAS detector at $\sqrt{s} = 13$ TeV*, Tech. Rep. ATL-PHYS-PUB-2015-023, CERN, Geneva, Jul, 2015. http://cds.cern.ch/record/2037700. (Cited on page 107.)

[117] G. Busoni et al., *Recommendations on presenting LHC searches for missing transverse energy signals using simplified s-channel models of dark matter*, arXiv:1603.04156 [hep-ex]. (Cited on pages 115 and 116.)

[118] M. Baak, G. J. Besjes, D. Côte, A. Koutsman, J. Lorenz, and D. Short, *HistFitter software framework for statistical data analysis*, Eur. Phys. J. **C75** (2015) 153, arXiv:1410.1280 [hep-ex]. (Cited on page 113.)

[119] A. L. Read, *Presentation of search results: the CL s technique*, Journal of Physics G: Nuclear and Particle Physics **28** (2002) 2693. (Cited on page 113.)